GEOMETRIC MULTIGRID METHODS FOR FLOW PROBLEMS IN HIGHLY HETEROGENEOUS POROUS MEDIA

A Dissertation

by

YOULI MAO

Submitted to the Office of Graduate and Professional Studies of
Texas A&M University
in partial fulfillment of the requirements for the degree of

DOCTOR OF PHILOSOPHY

Chair of Committee,	Raytcho Lazarov
Co-Chair of Committee,	Guido Kanschat
Committee Members,	Andrea Bonito
	Benchun Duan
Head of Department,	Emil Straube

August 2014

Major Subject: Mathematics

ABSTRACT

In this dissertation, we develop geometric multigrid methods for the finite element approximation of flow problems (*e.g.*, Stokes, Darcy and Brinkman models) in highly heterogeneous porous media. Our method is based on H^{div}-conforming discontinuous Galerkin methods and the Arnold-Falk-Winther (AFW) type smoothers. The main advantage of using H^{div}-conforming elements is that the discrete velocity field will be globally divergence-free for incompressible fluid flows. Besides, the smoothers used are of overlapping domain decomposition Schwarz type and employ a local Helmholtz decomposition.

Our flow solvers are the combination of multigrid preconditioners and classical iterative solvers. The proposed preconditioners act on the combined velocity and pressure space and thus does not need a Schur complement approximation. There are two main ingredients of our preconditioner: first, the AFW type smoothers can capture a meaningful basis on local divergence free subspace associated with each overlapping patch; second, the grid operator does not increase the divergence from the coarse divergence free subspace to the fine one as the divergence free spaces are nested.

We present the convergence analysis for the Stokes' equations and Brinkman's equations (with constant permeability field), as well as extensive numerical experiments. Some of the numerical experiments are given to support the theoretical results. Even though we do not have analysis work for the highly heterogeneous and highly porous media cases, numerical evidence exhibits strong robustness, efficiency and unification of our algorithm.

ACKNOWLEDGEMENTS

First and foremost, I would like to express my deep appreciation to Dr. Guido Kanschat and Dr. Raytcho Lazarov for all the guidance and consistent support during my graduate career. Dr. Kanschat gave me many great ideas for my research and showed me invaluable insights. Dr. Lazarov provided me with excellent advice and assistance and constructive criticism during the preparation of this dissertation. I would like to thank Dr. Andrea Bonito and Dr. Benchun Duan for serving on my committee and presenting many insightful comments and questions.

I would like to thank Dr. Vivette Girault and Dr. Joe Pasciak for helpful discussions and insightful suggestions on multigrid analysis work. I wish to express my gratitude to Dr. Todd Arbogast and Dr. Joerg Willems for valuable discussions about permeability data of highly heterogeneous and highly porous media. I am also grateful to Dr. Wolfgang Bangerth and Dr. Timo Heister for their help and guidance on implementation with Deal.II library. I also would like to thank Dr. Kainan Wang for the valuable discussions and his kind help during my graduate study.

I also wish to express my gratitude to the professors and staff of the Department of Mathematics at Texas A&M University. Additionally, I would like to thank Dr. Paulo Lima-Filho and Dr. Peter Howard, who were graduate advisors during my graduate career. I also wish to thank Ms. Monique Stewart for her incredible knowledge and ability as graduate program assistant.

Last, but most importantly, I would like to thank my wife, my parents and my friends for their unconditional support, their encouragement and their confidence in me during last five years.

TABLE OF CONTENTS

LIST OF FIGURES

FIGURE Page

LIST OF TABLES

TABLE Page

1. INTRODUCTION

Flow through porous media occurs in many real-world applications (e.g., hydrology, ecology, industrial filters and oil exploration, thermal insulation engineering, etc) and this has attracted substantial attention throughout both academic and industrial communities in the last century. With the advent of the computers and due to their capabilities for large scale simulations the research has focused on better mathematical models and efficient numerical methods describing the flow processes in porous media. All these processes have multi-scale phenomena and could involve multiple phases, species, and have multi-physics nature.

On a macro level the most popular mathematical model is represented by conservation of mass and Darcy's law that relates the gradient of the macroscopic pressure with the macroscopic fluid velocity. Currently, Darcy's law is still the most popular model for fluid flows with relatively small Reynolds number and for media with relatively small porosity. The main deficiency of Darcy's law is disregarding the viscous effects in the flow, a fact that is not always appropriate to neglect on the fluid's properties and the corresponding pore size distribution. In response to the limitations of Darcy's law, in 1947 Brinkman proposed a phenomenologically more adequate model (cf. [23]), considered as an extension of Darcy's Law, which takes into account the viscous effects of the fluid. Experimentally, Brinkman's model has shown to better describe for fluid flows in highly porous media (especially, for porosity for more than 0.8). Theoretically, Brinkman model can be rigorously derived from Stokes' flows in a media with periodically arranged obstacles through Allaire's homogenization theory (cf. [2]) under proper assumptions, which are close to media of low solid volume fraction (i.e. highly porous media).

Remark 1. *(Comments about homogenization theory in [2]) The obvious limitation of the homogenization theory is that it can be used only for periodic or statistically homogeneous porous media. For such media the theory delivers complete and practically useful results. However, for highly heterogeneous media the theory is not applicable, but it could be used as a guiding tool in modeling and simulations.*

1.1 Mathematical models of flow in porous media

Now, we use mathematical language to express the physical relations into a system of partial differential equations for the macroscopic characteristics of the flow, the pressure p and the fluid velocity u. For Ω being a bounded Lipschitz domain in $\mathbb{R}^d$ with dimension $d = 2, 3$, the steady-state Brinkman model reads:

$$\begin{aligned} -\mu\triangle u + \kappa u + \nabla p &= f, \quad in \quad \Omega \\ \nabla\cdot u &= 0, \quad in \quad \Omega \\ u &= u^B, \quad on \quad \partial\Omega \end{aligned} \tag{1.1}$$

The coefficient μ is the fluid viscosity and the coefficient $\kappa(x) = K^{-1}(x)$, where $K(x)$ is the permeability of the porous medium. In general, $K(x)$ is symmetric and uniformly in Ω positive definite $d \times d$ matrix. However, for our purposes it is enough to consider it as a diagonal matrix and in most of the cases as an identity matrix scaled by a scalar function, i.e. $K(x) = diag\{K_{11}(x), \ldots, K_{dd}(x)\}$. Depending on the viscosity μ and the inverse permeability κ, we distinguish different types of flows in various subdomains

$$\begin{cases} \kappa = 0 \neq \mu & \text{in } \Omega_S \quad \text{Stokes flow,} \\ \kappa \neq 0 = \mu & \text{in } \Omega_D \quad \text{Darcy's flow,} \\ \kappa \neq 0 \neq \mu & \text{in } \Omega_B \quad \text{Brinkman flow.} \end{cases}$$

The numerical methods (finite difference, finite volume and finite element - conforming, nonconforming and mixed - methods) for Stokes' and Darcy's equations are by now well understood and quite mature. From the finite element point of view, there are many stable elements available for them in current literature. Therefore, one natural approach in approximation of Brinkman's equations (1.1) is to modify these stable elements. In fact, there are a great many works following this nature approach, for instance, modifications based on Stokes elements with various stabilization techniques (*e.g.*, [7, 25, 32, 46, 47, 68]), modifications based on Darcy elements (*e.g.*, [68, 71, 97]) and solving the coupling of Stokes and Darcy flows (*e.g.*, [26, 63, 69, 73]), etc. Besides, there are also other elements directly constructed for Brinkman's equations (cf. [24, 98]). A high proportion of these works have been developed on topologically simple geometries associated with constant or smoothly varying permeability coefficients.

Understandably, we are not satisfied with just idealized geometries and simple permeability fields. Specifically, we aim at the numerical simulation of flows in the heterogeneously porous media such as glass wool (one of heat insulators, see Figure 1.1), open foam (one of industrial filters,see Figure 1.2), and natural reservoirs (see Figure 1.3), etc.

Figure 1.1: Microstructure and Macrostructure of glass wool (cf. [55])

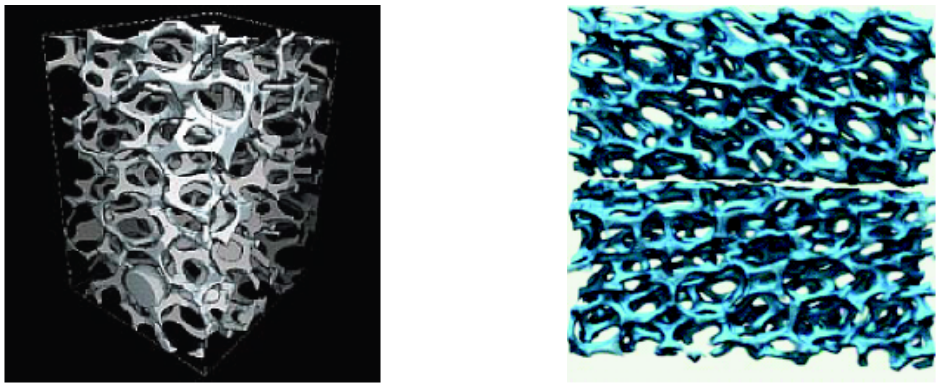

Figure 1.2: Microstructure of industrial foams (cf. [55])

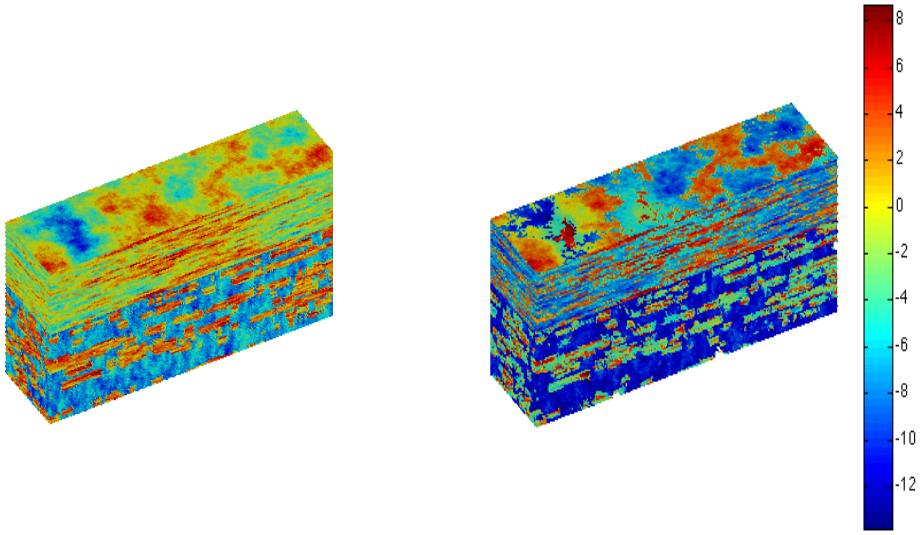

Figure 1.3: 3-D logarithmic plots of the horizontal and vertical permeability coefficients of SPE 10 benchmark dataset (cf. [28]). Note that there are 85 distinct layers in this natural reservoir model and the coefficient field admits the large jumps between different cells with contrast up to 10^8.

Remark 2. *(Comments about Figure 1.1-1.3) The porous mediums in Figure 1.1-1.3 usually refer to highly heterogeneous and/or highly porous media. The heterogeneity often means that these media contain different composites which may be randomly distributed inside the matrix. Another issue with this type of materials is the size of permeability. Take 3-D the SPE 10 benchmark natural reservoir dataset (Figure 1.3) for example, the dimensions of the fine scale geological model are* $1200 \times 2200 \times 170$ *(ft). A fine scale grid size of* $1 \times 1 \times 1$ *(ft) will produce over 40 million cells, which would require tremendous computational effort even with modern supercomputers. Moreover, the discrete system obtained from finite element approximation of Brinkman's equations in this case will be extremely ill-conditioned due to significantly varying permeability coefficients.*

Due to the heterogeneity of the media at different scales (*e.g.*, micro-scale and macro-scale) fast and accurate numerical solution of Brinkman's equations is still a challenging task. More precisely, it is very demanding to simultaneously resolve all structural features that are at different length scales. Additionally, according to the example in Remark 2, the high variability of the permeability negatively affects the condition number of the corresponding discrete system. These ill-conditioned systems have posed an enormous challenge for developing efficient solvers.

As we pointed out in Remark 1, the homogenization theory ([2]) may not work well for the cases where the geometries are rather complex such as highly heterogeneous and highly porous media. Despite this, the main ideas have been imported to several numerical upscaling approaches. Here, by upscaling we mean the method to compute the finite element basis functions on the coarse grids based on the information on the fine grid. To tackle these ill-condition systems arising from the approximation of Brinkman's equations in heterogeneous porous media, the following two major approaches have been heavily used in the existing literature:

1. Multiscale methods (MS): MS finite volume by Jenny, Lunati and Hajibeygi [17, 45, 57];Galerkin MS finite element method by Hou and Efendiev [39, 38]; MS mortar finite element by Arbogast, Pencheva, Wheeler and Yotov [8, 9]; subgrid method by Arbogast [6], and Illiev, Lazarov and Willems [54, 95];

2. Algebraic multigrid method (AMG), by Efendiev, Galvis, and Vassilevski [36, 37, 90, 91] and Villa [92].

Furthermore, a number of other approaches that have emerged in the resent years and were used in this area: mixed discontinuous Galerkin method by Konno and Stenberg [68], pressure Schur complement preconditioning by Popov [79] and weak Galerkin FEM by Mu, Wang and Ye [72], to name a few.

However, up to our best knowledge, the Geometric Multigrid Method (GMG), known as a powerful tool for fast solution of linear systems arising the finite element approximations, has not been applied in this field. In fact, the author could not find any work with GMG for flows problems in highly heterogeneous and highly porous media in current literature. One may wonder why? There are two major reasons for it: first, the performance of GMG on problems with variable coefficients often has not been quite satisfactory, as pointed out by many investigators in classical multigrid textbooks (*e.g.*, [86, 22]); additionally, GMGs with traditional smoothers are not suitable for discrete system arising from the popular H^{div}-conforming discretization for Brinkman's model (*e.g.*, [27, 61, 62]). To some extent, this dissertation shows that this situation could be largely improved: with certain modifications, GMG could regain the power of efficiency for this class of problems.

1.2 Dissertation outline

In this dissertation, we propose and analyze an efficient solver for the finite element approximation of the Brinkman system, which is based on Geometric Multigrid Method (with Arnold-Falk-Winther (AFW) type smoothers) and H^{div}-conforming discontinuous Galerkin methods. (Note: by solver in this dissertation we refer to the combination of the multigrid preconditioner and classical iterative solver).

The **main goals** of this dissertation are to:

(a) derive, analyze, and numerically test solvers for the finite element approximation of the Brinkman system used as a model of flows in highly heterogeneous porous media with high porosity; here the objective is to develop a robust and efficient solver that is independent of mesh size and of the distribution of the permeability.

(b) improve the computational performance with two objectives: first, rapidly convergent method (most existing algorithms converge at a very slow rate and are

very time consuming); second, perform simulations of flows in porous media on very fine scale, *e.g.* on meshes with 2048×2048 (for $RT0$) or 512×512 (for $RT1$) grid-blocks in two spacial dimensions; note that these meshes represent well the original geological benchmark dataset for natural reservoirs, e.g., shown on Figure 1.3 and will lead to a significant improvement in the numerical results. Most of current algorithms are applied to 128×128 or even coarser grids.

(c) unify the implementation of dimension and the polynomial order of the finite elements. The first objective is to make the implementation easily extendable to two or three dimension. The second objective is to implement finite elements with any order (many of the current algorithms are only limited to certain order of finite element and two dimensional mesh).

As a byproduct of the Brinkman solver, we also obtained efficient Stokes and Darcy solvers under the same multigrid framework. For the readers' benefit, we start with Stokes solver. Then, we add Darcy flow region into the Stokes model by a topologically simple way and build a solver for the coupling Stokes-Darcy flow. Finally, we present the Brinkman solver as well as Darcy solver in heterogeneously porous media. All proposed numerical algorithms are implemented in the open source software Deal.II - a Finite Element Differential Equations Analysis Library of Bangerth, Heister and Kanschat [15]; in particular, the multilevel support by Kanschat based on [56].

The dissertation is organized as follows.

1. In Section 2, we introduce the H^{div}-conforming discontinuous Galerkin discretization (cf. [30, 64]) for the Stokes' equations and present the idea of geometric multigrid preconditioners (cf. [11, 12]). Particular emphasis are put on the overlapping domain decomposition Schwarz smoothers (additive and mul-

tiplicative). We then prove the convergence analysis for the proposed method. Numerical results of different Schwarz smoothers and conclusion are provided at the end of this section.

2. In Section 3 we study the coupling of Stokes-Darcy flow model with Beavers-Joseph-Saffman interface boundary conditions (cf. [16]). Next, we apply a H^{div}-conforming discontinuous Galerkin discretization with interior penalty method for the proposed model problem (cf. [63]). The multigrid preconditioning method is presented and relevant discussion on the smoother choice is given. We conclude this section with numerical experiments on two setups.

3. In Section 4, we present a brief introduction of the Brinkman model in heterogeneously porous media (cf. [3, 4]). We then derive and analyze a mixed finite element discretization for the Brinkman's equations. The multigrid method and convergence analysis are followed. Substantial numerical results on different heterogeneous porous media geometries are presented, followed by a brief conclusion.

4. Finally, summary of the dissertation and comments on some future work are reported in Section 5.

2. THE STOKES' EQUATIONS*

The presentation and numerical experiments in this section closely follow the manuscript [61].

2.1 Introduction

The efficient solution of the Stokes' equations is an important step in the development of fast flow solvers. In this section we present analysis and numerical results for a multigrid method with subspace correction smoother, which performs very efficiently on divergence-conforming discretizations with interior penalty. We obtain convergence rates for the Stokes problem which are comparable to those for the Laplacian.

Multigrid methods are known to be the most efficient preconditioners and solvers for diffusion problems. Nevertheless, for Stokes equations, the divergence constraint makes the solution process more complicated. A typical solution employs the use of block preconditioners, e. g. [40, 66, 74, 59], but their disadvantage is, that their performance is limited by the inf-sup constant of the problem. This could be avoided, if the multigrid method operated on the divergence free subspace directly, and thus would not have to deal with the saddle point problem at all. Such methods have been developed in different context and have proven very successful as reported for instance by Hiptmair [50] for Maxwell equations and by Schöberl [83] for incompressible elasticity with reduced integration.

The main ingredients into such a method are a smoother which operates on the divergence free subspace and a grid transfer operator from coarse to fine mesh which

*Reprinted with permission from "Multigrid methods for H^{div}-conforming discontinuous Galerkin methods for the Stokes equations " by Guido Kanschat and Youli Mao, 2014. Journal of Numerical Mathematics, accepted for publication, Copyright [2014] by De Gruyter.

maps the coarse divergence free subspace into the fine one. The second objective can be achieved by using a mixed finite element discretization for which the weakly divergence free functions are point-wise divergence free. For such a discretization, the natural finite element embedding operator from coarse to fine mesh does not increase the divergence of a function. Discretizations of this type are available, such as for instance in Scott and Vogelius [85, 93], Neilan and coauthors [44, 41] and Zhang [99, 100]. Here, we focus on the divergence conforming discontinuous Galerkin (DivDG) method of Cockburn, Kanschat, and Schötzau [30] due to its simplicity.

Following the approach by Schöberl [83], in order to study smoothers for the Stokes' equations, we first consider a problem on the velocity space only with penalty for the divergence. This leads to a singularly perturbed problem with an operator with a large kernel. When it comes to smoothers for such operators, there are two basic options. One approach is to smooth the kernel of the H^{div} space explicitly, as proposed for instance by Hiptmair [50] and Xu in [51]. The other option was presented by Arnold, Falk, and Winther in [11, 12] and smoothens the kernel implicitly, while never employing an explicit description of it.

We follow the implicit approach and use the same domain decomposition principle (i.e additive and multiplicative Schwarz methods and vertex patches), but instead of the Maxwell or divergence dominated mass matrix as in [11, 12] apply it to the DivDG Stokes discretization. Then, we prove the convergence of the multigrid method with respect to variable V-cycle scheme for the singularly perturbed problem. The second pillar we rest on is the equivalence between singularly perturbed, divergence dominated elliptic forms and mixed formulations established by Schöberl in [83, 82]. This equivalence allows us to apply the smoother to a mixed formulation of nearly incompressible elasticity and then to proceed to the Stokes limit. As far as we know, the combination of these techniques has not been applied the DivDG method in [30].

Since our analysis is based on domain decomposition, fundamental results are also drawn from the seminal paper by Feng and Karakashian [42] on domain decomposition for discontinuous Galerkin methods for elliptic problems.

There is a close relation between our technique and the smoother suggested by Vanka in [89] for the MAC scheme: the MAC scheme can be considered the lowest order case of the DivDG methods (see [60]). In this case, the subspace decomposition structure of Vanka smoother corresponds to Neumann problems on cells, while our smoother is based on Dirichlet problems for vertex patches. Generalizations of the Vanka smoother have been applied successfully to different other discretizations albeit their velocity-pressure spaces are not matched in the sense of (2.2) (see for instance[87, 96] and literature cited there).

Recently, an alternative preconditioning method for Stokes discretizations of the same type as here has been introduced in [14] by Ayuso et al. Their method is based on auxiliary spaces introduced by Hiptmair and Xu in [51]. The exact sequence property of the divergence-conforming velocity element plays a crucial role as in our scheme, but their preconditioner uses a multigrid method for the biharmonic problem to solve the Stokes problem. As a consequence, it is not possible to use the preconditioning method for no-slip boundary conditions. On the other hand, it has been demonstrated in [65] that the multigrid method here can be lifted to the biharmonic problem, providing an efficient method for clamped boundary conditions.

This section is organized as follows. In Subsection 2.2 we present the model problem and the DG discretization. The multigrid method and domain decomposition smoother are derived in Subsection 2.4. Subsection 2.7 is devoted to the convergence analysis of our preconditioning technique with the main result in Theorem 1 on page 26. Numerical results for additive and multiplicative Schwarz smoothers of our multigrid method are presented in Subsection 2.8.

We consider discretizations of the Stokes' equations

$$\begin{aligned} -\triangle u + \nabla p &= f \qquad \text{in} \quad \Omega, \\ \nabla \cdot u \qquad &= 0 \qquad \text{in} \quad \Omega, \\ u \quad &= u^B \qquad \text{on} \quad \partial\Omega, \end{aligned} \tag{2.1}$$

with no-slip boundary conditions on a bounded and convex domain $\Omega \subset \mathbb{R}^d$ with dimension $d = 2, 3$. The natural solution spaces for this problem are $V = H_0^1(\Omega; \mathbb{R}^d)$ for the velocity u and the space of mean value free square integrable functions $Q = L_0^2(\Omega)$ for the pressure p, although we point out that other well-posed boundary conditions do not pose a problem.

In order to obtain a finite element discretization, we partition the domain Ω into a hierarchy of meshes $\{\mathbb{T}_j\}_{j=0,\dots,L}$ of parallelogram and parallelepiped cells in two and three dimensions, respectively. In view of multilevel methods, the index j refers to the mesh level defined as follows: let a coarse mesh $\mathbb{T}_0$ be given. The mesh hierarchy is defined recursively, such that the cells of $\mathbb{T}_{j+1}$ are obtained by splitting each cell of $\mathbb{T}_j$ into 2^d congruent children (refinement). These meshes are nested in the sense that every cell of $\mathbb{T}_j$ is equal to the union of its four children. We define the mesh size h_j as the maximum of the diameters of the cells of $\mathbb{T}_j$. Due to the refinement process, we have $h_j = 2^{-j} h_0$.

By construction, these meshes are conforming in the sense that every face of a cell is either at the boundary or a whole face of another cell; nevertheless, local refinement and hanging nodes do not pose a particular problem, since they can be treated following [56, 58]. By $\mathbb{F}_j$ we denote the set of all faces of the mesh $\mathbb{T}_j$, which is composed of the set of interior faces $\mathbb{F}_j^i$ and the set of all boundary faces $\mathbb{F}_j^\partial$.

We introduce a short hand notation for integral forms on $\mathbb{T}_j$ and on $\mathbb{F}_j$ by

$$\big(\phi,\psi\big)_{\mathbb{T}_j} = \sum_{T\in\mathbb{T}_j}\int_T \phi\odot\psi\,dx, \qquad \big\langle\phi,\psi\big\rangle_{\mathbb{F}_j} = \sum_{F\in\mathbb{F}_j}\int_F \phi\odot\psi\,ds,$$
$$\big\|\phi\big\|_{\mathbb{T}_j} = \Big(\sum_{T\in\mathbb{T}_j}\int_T |\phi|^2\,dx\Big)^{\frac{1}{2}}, \qquad \big\|\phi\big\|_{\mathbb{F}_j} = \Big(\sum_{F\in\mathbb{F}_j}\int_F |\phi|^2\,ds\Big)^{\frac{1}{2}},$$

The point-wise multiplication operator $\phi\odot\psi$ refers to the product $\phi\psi$, the scalar product $\phi\cdot\psi$ and the double contraction $\phi:\psi$ for scalar, vector and tensor arguments, respectively. The modulus $|\phi| = \sqrt{\phi\odot\phi}$ is defined accordingly.

In order to discretize (2.1) on the mesh $\mathbb{T}_j$, we choose discrete subspaces $X_j = V_j\times Q_j$, where $Q_j\subset Q$. Following [30], we employ discrete subspaces V_j of the space $H_0^{\mathrm{div}}(\Omega)$, where

$$H^{\mathrm{div}}(\Omega) = \big\{v\in L^2(\Omega;\mathbb{R}^d)\big|\nabla\cdot v\in L^2(\Omega)\big\},$$
$$H_0^{\mathrm{div}}(\Omega) = \big\{v\in H^{\mathrm{div}}(\Omega)\big|v\cdot\mathbf{n} = 0 \quad \text{on } \partial\Omega\big\}.$$

Here, we choose the well-known Raviart–Thomas space[81], but we point out that any pair of velocity spaces V_j and pressure spaces Q_j is admissible, if the key relation

$$\nabla\cdot V_j = Q_j \tag{2.2}$$

holds. The details of constructing the Raviart–Thomas space follow.

Each cell $T\in\mathbb{T}_j$ can be obtained as the image of a linear mapping Ψ_T of the reference cell $\widehat{T} = [0,1]^d$. On the reference cell, we define two polynomial spaces: first, $\widehat{Q}_k$, the space of polynomials in d variables, such that the degree with respect to each variable does not exceed k. Second, we consider the vector valued space of Raviart–Thomas polynomials $\widehat{V}_k = \widehat{Q}_k^d + x\widehat{Q}_k$. Polynomial spaces V_T and Q_T on the mesh cell

T are obtained by the pull-back under the mapping Ψ_T (see for instance [13]). The polynomial degree k is arbitrary, but chosen uniformly on the whole mesh. Thus, we will omit the index k from now on. Concluding this construction, we obtain the finite element spaces

$$V_j = \left\{ v \in H_0^{\mathrm{div}}(\Omega) \middle| \forall T \in \mathbb{T}_j : v_{|T} \in V_T \right\},$$
$$Q_j = \left\{ q \in L_0^2(\Omega) \middle| \forall T \in \mathbb{T}_j : q_{|T} \in Q_T \right\}.$$

2.2 Discontinuous Galerkin discretization

While the fact that V_j is a subspace of $H_0^{\mathrm{div}}(\Omega)$ implies continuity of the normal component of its functions across interfaces between cells, this is not true for tangential components. Thus, $V_j \not\subset H^1(\Omega;\mathbb{R}^d)$, and it cannot be used immediately to discretize (2.1). We follow the example in for instance [30, 64, 63] and apply a DG formulation to the discretization of the elliptic operator. Here, we focus on the interior penalty method[10, 75]. Let T_1 and T_2 be two mesh cells with a joint face F, and let u_1 and u_2 be the traces of a function u on F from T_1 and T_2, respectively. On this face F, we introduce the averaging and the jump operator

$$\{\!\{u\}\!\} = \frac{u_1 + u_2}{2}, \ \textit{and} \ \ [\![u]\!] = u_1 - u_2 \tag{2.3}$$

In this notation, the interior penalty bilinear form reads

$$\begin{aligned} a_j(u,v) =& \big(\nabla u, \nabla v\big)_{\mathbb{T}_j} + 4\big\langle \sigma_J \{\!\{u \otimes \mathbf{n}\}\!\}, \{\!\{v \otimes \mathbf{n}\}\!\} \big\rangle_{\mathbb{F}_j^i} \\ & - 2\big\langle \{\!\{\nabla u\}\!\}, \{\!\{\mathbf{n} \otimes v\}\!\} \big\rangle_{\mathbb{F}_j^i} - 2\big\langle \{\!\{\nabla v\}\!\}, \{\!\{\mathbf{n} \otimes u\}\!\} \big\rangle_{\mathbb{F}_j^i} \\ & + 2\big\langle \sigma_J u, v \big\rangle_{\mathbb{F}_j^\partial} - \big\langle \partial_n u, v \big\rangle_{\mathbb{F}_j^\partial} - \big\langle \partial_n v, u \big\rangle_{\mathbb{F}_j^\partial}. \end{aligned} \tag{2.4}$$

The operator "$\otimes$" denotes the Kronecker product of two vectors. We note that the term $4\{\!\{u \otimes \mathbf{n}\}\!\} : \{\!\{v \otimes \mathbf{n}\}\!\}$ actually denotes the product of the jumps of u and v.

The discrete weak formulation of (2.1) reads now: find $(u_j, p_j) \in V_j \times Q_j$, such that for all test functions $v_j \in V_j$ and $q_j \in Q_j$ there holds

$$\mathcal{A}_j \left(\begin{pmatrix} u_j \\ p_j \end{pmatrix}, \begin{pmatrix} v_j \\ q_j \end{pmatrix} \right) \equiv a_j(u_j, v_j) - \big(p_j, \nabla \cdot v_j\big) - \big(q_j, \nabla \cdot u_j\big) = \mathcal{F}(v_j, q_j) \equiv \big(f, v_j\big). \tag{2.5}$$

Discussion on the existence and uniqueness of such solutions can be found for instance in [30, 31, 48, 63]. Here, we summarize that the discrete system (2.5) is symmetric. If σ_J is sufficiently large, the form $a_j(.,.)$ is positive definite independently of the multigrid level $j \in [0, L]$, and that thus we can define a norm on V_j by

$$\big\|v_j\big\|_{V_j} = \sqrt{a_j(v_j, v_j)}. \tag{2.6}$$

In order to obtain optimal convergence results and to satisfy Proposition 3 below, σ_J is chosen as $\overline{\sigma}/h_J$, where h_J is mesh size on the finest level J and $\overline{\sigma}$ is a positive constant depending on the polynomial degree. By this choice, the bilinear forms on lower levels are inherited from finer levels in the sense, that

$$a_j(u_j, v_j) = a_J(u_j, v_j), \quad \forall\, u_j, v_j \in V_j. \tag{2.7}$$

A particular feature of this method is (see [29, 30]), that the solution u_j is in the divergence free subspace

$$V_j^0 = \big\{ v_j \in V_j \big| \nabla \cdot v_j = 0 \big\}, \tag{2.8}$$

where the divergence condition is to be understood in the strong sense.

Proposition 1 (Inf-sup condition)**.** *For any pressure function $q \in Q_j$, there exists a velocity function $v \in V_j$, satisfying*

$$\sup_{v \in V_j} \frac{\big(q, \nabla \cdot v\big)}{\big\|v\big\|_{V_j}} \geq \gamma_j \big\|q\big\|_{L^2(\Omega)} > 0 \tag{2.9}$$

where $\gamma_j = c\sqrt{\frac{h_J}{h_j}} = c\sqrt{2^{j-J}}$ and c is a constant independent of the multigrid level j.

Proof. The proof of this proposition can be found in [84, Section 6.4]. Indeed, a different result is proven there, with $\gamma_j \approx 1/k$, where k is the polynomial degree in the *hp*-method. Thorough study of the proof though reveals, that this k-dependence is due to the penalty parameter of the form $\sigma_j \approx k^2/h_j$. In our case, the penalty parameter depends on the fine mesh, not on h_j, such that $\sigma_j \approx (h_j/h_J)/h_j$, and that the role of the k^2 in the penalty is taken by the factor h_j/h_J. □

For any $u \in V_j$, we consider the following discrete Helmholtz decomposition:

$$u = u^0 + u^\perp \tag{2.10}$$

where $u^0 \in V_j^0$ is the divergence free part and $u^\perp$ belongs to its $a_j(.,.)$-orthogonal complement. For functions from this complement holds the estimate:

Lemma 1. *Let $u^\perp \in V_j$ be $a_j(.,.)$-orthogonal to V_j^0, that is,*

$$a_j(u^\perp, v) = 0 \quad \forall\, v \in V_j^0.$$

Then, there is a constant $\alpha > 0$ such that

$$\frac{\alpha}{d^2}\left\|\nabla\cdot u^\perp\right\|^2 \leq a_j(u^\perp, u^\perp) \leq \frac{1}{\gamma_j}\left\|\nabla\cdot u^\perp\right\|^2, \tag{2.11}$$

γ_j is the inf-sup constant from inequality (2.9).

Proof. On the left side, we already argued above that σ_J is chosen large enough such that $a_j(.,.)$ is uniformly positive definite. Thus, we have with a positive constant α

$$\alpha\|\nabla u^\perp\|^2_{\mathbb{T}_j} \leq a_j(u^\perp, u^\perp).$$

But then,

$$\big(\nabla\cdot u^\perp, \nabla\cdot u^\perp\big)_\Omega \leq d^2\big(\nabla u^\perp, \nabla u^\perp\big)_{\mathbb{T}_j} \leq \frac{d^2}{\alpha}a_j(u^\perp, u^\perp),$$

On the right side, let $q = \nabla\cdot\, u^\perp$. Then $q \in Q_j$ due to (2.2). From (2.9), we conclude that there is $u \in V_j$ such that $\nabla\cdot u = q$ and $\left\|u\right\|_{V_j} \leq 1/\gamma_j\|q\|$. On the other hand, $u^\perp$ is the error of the orthogonal projection into V_j^0. Thus, $u^\perp$ must be the element with minimal norm, and in particular $\left\|u^\perp\right\|_{V_j} \leq \left\|u\right\|_{V_j}$. □

2.3 The nearly incompressible problem

We are going to prove convergence uniform with respect to the refinement level j of the proposed multigrid method for the Stokes problem by deviating twice. First, we provide estimates robust with respect to the parameter ϵ of the nearly incompressible problem: find $(u_j, p_j) \in V_j \times Q_j$ such that for all $(v_j, q_j) \in V_j \times Q_j$ there holds

$$\mathcal{A}_j\left(\begin{pmatrix}u_j\\ p_j\end{pmatrix}, \begin{pmatrix}v_j\\ q_j\end{pmatrix}\right) + \epsilon\big(p_j, q_j\big) = \mathcal{F}(v_j, q_j). \tag{2.12}$$

This problem is connected with the simpler penalty bilinear form (see for instance also [48])

$$A_{j,\epsilon}(u_j, v_j) \equiv a_j(u_j, v_j) + \epsilon^{-1}\big(\nabla\cdot u_j, \nabla\cdot v_j\big) \tag{2.13}$$

and the singularly perturbed, elliptic problem: find $u_j \in V_j$ such that for all $v_j \in V_j$ there holds

$$A_{j,\epsilon}(u_j, v_j) = \big(f, v_j\big). \tag{2.14}$$

Lemma 2. *Let (u_m, p_m) be the solution to (2.12) and u_e be the solution to (2.14). Then, if (2.2) holds, the following equations hold true:*

$$u_m = u_e, \qquad \textit{and} \qquad \epsilon p_m = \nabla\cdot u_m = \nabla\cdot u_e.$$

Proof. Testing (2.12) with $v_j = 0$ and $q_j \in Q_j$ yields

$$-\big(\nabla\cdot u_m, q_j\big) + \epsilon(p_m, q_j) = 0 \quad \forall\, q_j \in Q_j.$$

Due to (2.2), this translates to the point-wise equality $\epsilon p_m = \nabla\cdot\ u_m$. Substituting p_m in (2.12) and testing with the pair $(v_j, \nabla\cdot v_j)$, which is possible again due to (2.2), we obtain that u_m solves (2.14).

If on the other hand u_e solves (2.14), we introduce $p_e = \frac{1}{\epsilon}\nabla\cdot u_e$, which translates to

$$-\big(\nabla\cdot u_e, q_j\big) + \epsilon(p_e, q_j) = 0 \quad \forall\, q_j \in Q_j,$$

corresponding to (2.12) tested with $(0, q_j)$. On the other hand, (2.12) tested with $(v_j, 0)$ is obtained directly from (2.14) substituting p_e. Thus, the equivalence is proven. □

In order to help keeping the notation separate, we adopt the following convention: the subscript ϵ is dropped wherever possible. Furthermore, curly letters refer to the mixed form, while straight capitals refer to operators on the velocity space only. Thus:

$a_j(u, v)$ the vector valued interior penalty form

$A_j(u, v)$ the form of the singularly perturbed, elliptic problem (2.14)

$\mathcal{A}_j\left(\begin{pmatrix} u \\ p \end{pmatrix}, \begin{pmatrix} v \\ q \end{pmatrix}\right)$ the mixed bilinear form (2.12)

Similarly, capital letters like in R_j for the smoother (2.26) refer to the singularly perturbed, elliptic problem, while $\mathcal{R}_j$ is the corresponding symbol for the Stokes smoother (2.24). Additionally, we associate operators with bilinear forms using the same symbol:

$$A_{j,\epsilon} : V_j \to V_j \qquad \big(A_{j,\epsilon}u, v\big) = A_{j,\epsilon}\big(u, v\big) = A_j(u, v) = A_J(u, v) \qquad \forall u, v \in V_j$$
$$\mathcal{A}_{j,\epsilon} : X_j \to X_j \qquad \big(\mathcal{A}_{j,\epsilon}x, y\big) = \mathcal{A}_{j,\epsilon}\big(x, y\big) = \mathcal{A}_j(x, y) = \mathcal{A}_J(x, y) \qquad \forall x, y \in X_j$$

2.4 Multigrid method for Stokes

In Subsection 2.2, we introduced hierarchies of meshes $\{\mathbb{T}_j\}$. Due to the nestedness of mesh cells, the finite element spaces associated with these meshes are nested

as well:

$$\begin{array}{ccccccc} V_0 & \subset & V_1 & \subset & \dots & \subset & V_J, \\ Q_0 & \subset & Q_1 & \subset & \dots & \subset & Q_J. \\ X_0 = V_0 \times Q_0 & \subset & X_1 & \subset & \dots & \subset & V_J \times Q_J = X_J. \end{array}$$

This relation also extends to the divergence free subspaces, see for instance [65]:

$$V_0^0 \subset V_1^0 \subset \dots \subset V_J^0. \tag{2.15}$$

The nestedness of the spaces implies that there is a sequence of natural injections $\mathcal{I}_j : X_j \to X_{j+1}$ of the form $\mathcal{I}_j(v_j, q_j) = (I_{j,u}v_j, I_{j,p}q_j)$, such that

$$I_{j,u} : V_j \hookrightarrow V_{j+1}, \qquad I_{j,p} : Q_j \hookrightarrow Q_{j+1}, \tag{2.16}$$

$$I_{j,u} : V_j^0 \hookrightarrow V_{j+1}^0. \tag{2.17}$$

The L^2-projection from $X_{j+1} \to X_j$ is defined by $\mathcal{I}_j^t(v_j, q_j) = (I_{j,u}^t v_j, I_{j,p}^t q_j)$ with

$$\left(v_{j+1} - I_{j,u}^t v_{j+1}, w_j\right) = 0 \; \forall w_j \in V_j \qquad \left(q_{j+1} - I_{j,p}^t q_{j+1}, r_j\right) = 0 \; \forall r_j \in Q_j. \tag{2.18}$$

The $\mathcal{A}$-orthogonal projection $\mathcal{P}_j$ from $(V_J \times Q_J) \to (V_j \times Q_j)$ is defined by

$$\mathcal{A}_J\big(\mathcal{P}_j \begin{pmatrix} u \\ p \end{pmatrix}, \begin{pmatrix} v_j \\ q_j \end{pmatrix}\big) = \mathcal{A}_J\big(\begin{pmatrix} u \\ p \end{pmatrix}, \begin{pmatrix} v_j \\ q_j \end{pmatrix}\big) \tag{2.19}$$

for all $(u, p) \in (V_J \times Q_J), (v_j, q_j) \in V_j \times Q_j$. Similarly, The A-orthogonal projection

P_j from $V_J \to V_j$ is defined by

$$A_J(P_j u, v_j) = A_J(u, v_j) \tag{2.20}$$

for all $u \in V_J, v_j \in V_j$.

2.5 The variable V-cycle algorithm

In this subsection we define V-cycle multigrid preconditioners $\mathcal{B}_{j,\epsilon}$ and $B_{j,\epsilon}$ for the operators $\mathcal{A}_{j,\epsilon}$ and $A_{j,\epsilon}$, respectively. For simplicity of the presentation, we drop the index ϵ.

First, we define the action of the multigrid preconditioner $\mathcal{B}_j : X_j \to X_j$ recursively as the multigrid V-cycle with $m(j) \geq 1$ pre- and post-smoothing steps. Let $\mathcal{R}_j$ be a suitable smoother. Let $\mathcal{B}_0 = \mathcal{A}_0^{-1}$. For $j \geq 1$, define the action of $\mathcal{B}_j$ on a vector $\mathcal{L}_j = (f_j, g_j)$ by

1. Pre-smoothing: begin with $(u_0, p_0) = (0, 0)$ and let

$$\begin{pmatrix} u_i \\ p_i \end{pmatrix} = \begin{pmatrix} u_{i-1} \\ p_{i-1} \end{pmatrix} + \mathcal{R}_j \left(\mathcal{L}_j - \mathcal{A}_j \begin{pmatrix} u_{i-1} \\ p_{i-1} \end{pmatrix} \right) \quad i = 1, \ldots, m(j), \tag{2.21a}$$

2. Coarse grid correction:

$$\begin{pmatrix} u_{m(j)+1} \\ p_{m(j)+1} \end{pmatrix} = \begin{pmatrix} u_{m(j)} \\ p_{m(j)} \end{pmatrix} + \mathcal{B}_{j-1} \mathcal{I}_{j-1}^t \left(\mathcal{L}_j - \mathcal{A}_j \begin{pmatrix} u_{m(j)} \\ p_{m(j)} \end{pmatrix} \right), \tag{2.21b}$$

3. Post-smoothing:

$$\begin{pmatrix} u_i \\ p_i \end{pmatrix} = \begin{pmatrix} u_{i-1} \\ p_{i-1} \end{pmatrix} + \mathcal{R}_j \left(\mathcal{L}_j - \mathcal{A}_j \begin{pmatrix} u_{i-1} \\ p_{i-1} \end{pmatrix} \right), \quad i = m(j)+2, \ldots, 2m(j)+1 \tag{2.21c}$$

4. Assign:

$$\mathcal{B}_j \mathcal{L}_j = \begin{pmatrix} u_{2m(j)+1} \\ p_{2m(j)+1} \end{pmatrix} \tag{2.21d}$$

We distinguish between the standard and variable V-cycle algorithms by the choice

$$m(j) = \begin{cases} m(J) & \text{standard V-cycle,} \\ m(J)2^{L-j} & \text{variable V-cycle,} \end{cases}$$

where the number $m(J)$ of smoothing steps on the finest level is a free parameter. We refer to $\mathcal{B}_J$ as the V-cycle preconditioner of $\mathcal{A}_J$. The iteration

$$\begin{pmatrix} u_{k+1} \\ p_{k+1} \end{pmatrix} = \begin{pmatrix} u_k \\ p_k \end{pmatrix} + \mathcal{B}_J \left(\mathcal{L}_J - \mathcal{A}_J \begin{pmatrix} u_k \\ p_k \end{pmatrix} \right) \tag{2.22}$$

is the V-cycle iteration.

The definition of the preconditioner $B_j : V_j \to V_j$ for the elliptic operator A_j follows the same concept, but dropping the pressure variables.

2.6 Overlapping Schwarz smoothers

In this subsection, we define a class of smoothing operators $\mathcal{R}_j$ based on a subspace decomposition of the space X_j. Let $\mathcal{N}_j$ be the set of vertices in the triangulation $\mathbb{T}_j$, and let $\mathbb{T}_{j,v}$ be the set of cells in $\mathbb{T}_j$ sharing the vertex v. They form a triangulation with $N(N > 0)$ subdomains or patches which we denote by $\{\Omega_{j,v}\}_{v=1}^{N}$.

The subspace $X_{j,v} = V_{j,v} \times Q_{j,v}$ consists of the functions in X_j with support in $\Omega_{j,v}$. Note that this implies homogeneous slip boundary conditions on $\partial\Omega_{j,v}$ for the velocity subspace $V_{j,v}$ and zero mean value on $\Omega_{j,v}$ for the pressure subspace $Q_{j,v}$. The Ritz projection $\mathcal{P}_{j,v} : X_j \to X_{j,v}$ is defined by the equation

$$\mathcal{A}_j\big(\mathcal{P}_{j,v}\begin{pmatrix} u_j \\ p_j \end{pmatrix}, \begin{pmatrix} v_{j,v} \\ q_{j,v} \end{pmatrix}\big) = \mathcal{A}_j\big(\begin{pmatrix} u_j \\ p_j \end{pmatrix}, \begin{pmatrix} v_{j,v} \\ q_{j,v} \end{pmatrix}\big) \qquad \forall \begin{pmatrix} v_{j,v} \\ q_{j,v} \end{pmatrix} \in X_{j,v}. \tag{2.23}$$

Note that each cell belongs to not more than four (eight in 3D) patches $\mathbb{T}_{j,v}$, one for each of its vertices.

Then we define the additive Schwarz smoother

$$\mathcal{R}_{a,j} = \eta \sum_{v \in \mathcal{N}_j} \mathcal{P}_{j,v}\mathcal{A}_j^{-1} \tag{2.24}$$

where $\eta \in (0, 1]$ is a scaling factor, $\mathcal{R}_{a,j}$ is L^2 symmetric and positive definite.

Similarly, we define smoothers of the singularly perturbed elliptic operator A_j, namely, $P_{j,v} : V_j \to V_{j,v}$ is defined as

$$A_j\big(P_{j,v}u_j, v_{j,v}\big) = A_j\big(u_j, v_{j,v}\big) \qquad \forall v_{j,v} \in V_{j,v}, \tag{2.25}$$

and the corresponding additive Schwarz smoother for the singularly perturbed prob-

lem is defined as follows:

$$R_{a,j} = \eta \sum_{\upsilon \in \mathcal{N}_j} P_{j,\upsilon} A_j^{-1}. \tag{2.26}$$

Here, we also define the symmetric multiplicative Schwarz smoother $\mathcal{R}_{m,j}$ associated with the spaces $X_{j,\upsilon}$, defined by

$$\mathcal{R}_{m,j} = (\mathcal{I} - \mathcal{E}_j \mathcal{E}_j^*) \mathcal{A}_j^{-1}, \tag{2.27}$$

$$\mathcal{E}_j = (\mathcal{I} - \mathcal{P}_{j,1}) \dots (\mathcal{I} - \mathcal{P}_{j,N}). \tag{2.28}$$

then by multiplying $\mathcal{A}_j$ on both side of (2.27), we get

$$\mathcal{I} - \mathcal{R}_{m,j} \mathcal{A}_j = \mathcal{E}_j \mathcal{E}_j^* \tag{2.29}$$

(Note that $\mathcal{E}_j^*$ is the adjoint of $\mathcal{E}_j$ with respect to the inner product $\mathcal{A}_j(\cdot, \cdot)$).

And corresponding multiplicative the smoother of the singularly perturbed elliptic operator A_j, namely, $P_{j,\upsilon} : V_j \to V_{j,\upsilon}$ is defined as

$$R_{m,j} = (I - E_j) A_j^{-1}, \tag{2.30}$$

$$E_j = (I - P_{j,1}) \dots (I - P_{j,N}). \tag{2.31}$$

Similarly,

$$I - R_{m,j} A_j = E_j E_j^* \tag{2.32}$$

(Note that E_j^* is the adjoint of E_j with respect to the inner product $A_j(\cdot, \cdot)$).

2.7 Convergence analysis

In this section, we provide a proof of the convergence for the variable V-cycle iteration with additive and multiplicative Schwarz preconditioning methods. Our proof is based on the assumption that the domain Ω is bounded and convex, which will be omitted for simplicity in the statement of following theorems and propositions.

The structure of the proof follows [83] in that we first consider a singularly perturbed elliptic problem (2.14) related to (2.12) in Subsection 2.7.1 and obtain uniform estimates with respect to ϵ in Theorem 2. Then, in Subsection 2.7.2, equivalence of the methods for the elliptic problem and the mixed problem is established. Finally, the estimate uniform in ϵ for (2.12) allows us to proceed to the limit $\epsilon \to 0$ to obtain the main convergence result, namely.

Theorem 1. *The multilevel iteration $\mathcal{I}-\mathcal{B}_J\mathcal{A}_J$ with the Variable V-cycle operator $\mathcal{B}_J$ defined in Section 2.5 employing the smoother $\mathcal{R}_j$ is a contraction with contraction number independent of the mesh level J.*

Proof. Under the hypotheses of Theorem 2 , the error operator $I-B_JA_J$ is a positive definite contractions on V_J independent of mesh level J. Following Theorem 3, we get the two multigrid algorithms for singularly-perturbed and mixed problems are equivalent in terms of velocity $u(u \in V_J)$. Then, the estimate uniform in ϵ for (2.12) gives us that $\mathcal{I} - \mathcal{B}_J\mathcal{A}_J$ is also a contraction with contraction number independent of the mesh level J when $\epsilon \to 0$. □

2.7.1 The singularly perturbed problem

Theorem 2. *Let R_j be the smoother defined in Section 2.6. Then, the multilevel iteration $I - B_JA_J$ with the variable V-cycle operator B_J defined in Section 2.5 is a contraction with contraction number independent of the mesh level J and the*

parameter ϵ.

The proof of this theorem relies on

Proposition 2. *If a smoother* R_j *satisfies the conditions:*

$$A_J\big((I - R_j A_j)w, w\big) \geq 0, \quad \forall w \in V_j \tag{2.33}$$

and

$$(R_j^{-1}[I - P_{j-1}]w, [I - P_{j-1}]w) \leq \beta_j A_J([I - P_{j-1}]w, [I - P_{j-1}]w), \quad \forall w \in V_j \tag{2.34}$$

where $\beta_j = O(\frac{1}{\gamma_j})$ *defined in the proof of Theorem 2. . Then*

$$0 \leq A_J\big((I - B_j A_j)w, w\big) \leq \delta A_J(w, w), \quad \forall w \in V_j \tag{2.35}$$

where $\delta = \frac{\hat{C}}{1+\hat{C}}$ *(*$\hat{C}$ *defined in Lemma 5)*

Proof. In the case of self-adjoint operators A_j which are inherited from a common bilinear form $a(.,.)$, this proposition is part of the standard multigrid theory and its proof can be adapted from similar theorems in [18, 19, 11].

Following the proof in [11], we want to show it by induction on i that

$$0 \leq A_J((I - B_i A_i)u, u) \leq \delta A_J(u, u), \quad \forall u \in V_j \tag{2.36}$$

For $i = 1$ is obvious since $B_1 = A_1^{-1}$. Now check if the above inequality hold for $i = j - 1$. Recall the relaxation operator $K_j = I - R_j A_j$ and the recurrence relation

introduced in [19]:

$$I - B_j A_j = K_j^{m(j)}[(I - P_{j-1}) + (I - B_{j-1}A_{j-1})P_{j-1}]K_j^{m(j)} \tag{2.37}$$

The lower bound easily follows from the inductive hypothesis and the above identity. For the upper bound, we use the induction hypothesis to obtain

$$A_J((I - B_j A_j)u, u) \leq A_J([I - P_{j-1}]K_j^{m(j)}u, K_j^{m(j)}u) + \delta A_J(P_{j-1}K_j^{m(j)}u, K_j^{m(j)}u) \tag{2.38}$$

$$= (1 - \delta)A_J([I - P_{j-1}]K_j^{m(j)}u, K_j^{m(j)}u) + \delta A_J(K_j^{m(j)}u, K_j^{m(j)}u) \tag{2.39}$$

Now by the orthogonality from 2.20

$$A_J([I - P_{j-1}]K_j^{m(j)}u, [I - P_{j-1}]K_j^{m(j)}u) \tag{2.40}$$

$$= A_J([I - P_{j-1}]K_j^{m(j)}u, K_j^{m(j)}u) \tag{2.41}$$

$$= ([I - P_{j-1}]K_j^{m(j)}u, A_j K_j^{m(j)}u) \tag{2.42}$$

$$= (R_j^{-1}[I - P_{j-1}]K_j^{m(j)}u, R_j A_j K_j^{m(j)}u) \tag{2.43}$$

$$\leq (R_j^{-1}[I - P_{j-1}]K_j^{m(j)}u, [I - P_{j-1}]K_j^{m(j)}u)^{\frac{1}{2}}(R_j A_j K_j^{m(j)}u, A_j K_j^{m(j)}u)^{\frac{1}{2}} \tag{2.44}$$

$$\leq \sqrt{\beta_j}([I - P_{j-1}]K_j^{m(j)}u, [I - P_{j-1}]K_j^{m(j)}u)^{\frac{1}{2}}(R_j A_j K_j^{m(j)}u, A_j K_j^{m(j)}u)^{\frac{1}{2}} \tag{2.45}$$

Hence, we get

$$A_J([I - P_{j-1}]K_j^{m(j)}u, K_j^{m(j)}u) \leq \beta_j(R_j A_j K_j^{m(j)}u, A_j K_j^{m(j)}u) \tag{2.46}$$

$$= \beta_j A_J([I - K_{j-1}]K_j^{2m(j)}u, u) \tag{2.47}$$

It follows from the positive semidefiniteness and (2.33). Therefore, we have

$$A_J([I - K_{j-1}]K_j^{2m(j)}u, u) \leq A_J([I - K_{j-1}]K_j^{i}u, u), \quad for \quad i \leq 2m(j) \tag{2.48}$$

whence

$$A_J([I - K_{j-1}]K_j^{2m(j)}u, u) \leq \frac{1}{2m(j)} \sum_{i=0}^{2m(j)-1} A_J([I - K_j]K_j^{i}u, u) \tag{2.49}$$

$$= \frac{1}{2m(j)} A_J([I - K_j]K_j^{2m(j)}u, u) \tag{2.50}$$

Combining 2.38 and 2.48 and following Lemma 5, we get

$$A_J((I - B_j A_j)u, u) \leq (1 - \delta)\frac{\beta_j}{2m(j)} A_J([I - K^{2m(j)}]u, u) + \delta A_J(K_j^{m(j)}u, K_j^{m(j)}u) \tag{2.51}$$

$$\leq (1 - \delta)\hat{C} A_J([I - K^{2m(j)}]u, u) + \delta A_J(K_j^{m(j)}u, K_j^{m(j)}u) \tag{2.52}$$

$$= (1 - \delta)\hat{C} A_J(u, u) + [\delta - (1 - \delta)\hat{C}]A_J(K_j^{m(j)}u, K_j^{m(j)}u) \tag{2.53}$$

The results now follows by choosing :

$$\delta = (1 - \delta)\hat{C}, i.e, \delta = \frac{\hat{C}}{1 + \hat{C}} \tag{2.54}$$

□

2.7.1.1 Proof for additive Schwarz smoother

In this subsection, we use several propositions and lemmas to establish our smoother $R_{a,j}$ satisfies the assumptions of Proposition 2. For $u \in (I - P_{j-1})w, w \in V_j$, it follows from the discrete Helmholtz decomposition in 2.2 and the projection operator $P_{j,v}$ in 2.6 that u admits a local discrete Helmholtz decomposition

$$u_v = u_v^0 + u_v^\perp \tag{2.55}$$

Lemma 3. *Given L^2-symmetric positive definite $R_{a,j}$ defined in 2.6 and symmetric positive definite $A_J(\cdot,\cdot)$ defined in* (2.13) *, there exists a scaling constant η (defined in* (2.24)*) independent of j such that*

$$\eta(R_{a,j}^{-1}u, u) = \inf_{\substack{u_v \in V_{j,v} \\ \Sigma_v u_v = u}} \sum_{v \in N_j} A_J(u_v, u_v) \tag{2.56}$$

Proof. The following proof can be found in [11]. We copy it here to ascertain that it does not depend on the actual structure of the operator A_J since it is purely algebraic. Thus, it applies to the operator A_J in this paper as it applies to the different operator applied there. Recall that

$$R_{a,j} = \eta \sum_{v \in \mathcal{N}_j} P_{j,v} A_j^{-1} = \eta \sum_{v \in \mathcal{N}_j} P_{j,v} A_J^{-1} \tag{2.57}$$

and

$$u = \sum_{v \in \mathcal{N}_j} u_v \tag{2.58}$$

we get

$$\eta(R_{a,j}^{-1}u,u) = \eta \sum_{\upsilon\in\mathcal{N}_j}(R_{a,j}^{-1}u,u_\upsilon) \tag{2.59}$$

$$= \eta \sum_{\upsilon\in\mathcal{N}_j}(A_J A_J^{-1}R_{a,j}^{-1}u,u_\upsilon) \tag{2.60}$$

$$= \eta \sum_{\upsilon\in\mathcal{N}_j}(A_J P_{j,\upsilon}A_J^{-1}R_{a,j}^{-1}u,u_\upsilon) \tag{2.61}$$

$$\leq \eta \sum_{\upsilon\in\mathcal{N}_j}(A_J P_{j,\upsilon}A_J^{-1}R_{a,j}^{-1}u, P_{j,\upsilon}A_J^{-1}R_{a,j}^{-1}u)^{\frac{1}{2}}(A_J u_\upsilon,u_\upsilon)^{\frac{1}{2}} \tag{2.62}$$

$$\leq \eta \sum_{\upsilon\in\mathcal{N}_j}(A_J P_{j,\upsilon}A_J^{-1}R_{a,j}^{-1}u, P_{j,\upsilon}A_J^{-1}R_{a,j}^{-1}u)^{\frac{1}{2}}(A_J u_\upsilon,u_\upsilon)^{\frac{1}{2}} \tag{2.63}$$

$$\leq \eta \left\{\sum_{\upsilon\in\mathcal{N}_j}(A_J P_{j,\upsilon}A_J^{-1}R_{a,j}^{-1}u, A_J^{-1}R_{a,j}^{-1}u)\right\}^{\frac{1}{2}}\left\{\sum_{\upsilon\in\mathcal{N}_j}(A_J u_\upsilon,u_\upsilon)\right\}^{\frac{1}{2}} \tag{2.64}$$

$$= \eta^{\frac{1}{2}} \left\{\sum_{\upsilon\in\mathcal{N}_j}(A_J \eta P_{j,\upsilon}A_J^{-1}R_{a,j}^{-1}u, A_J^{-1}R_j^{-1}u)\right\}^{\frac{1}{2}}\left\{\sum_{\upsilon\in\mathcal{N}_j}(A_J u_\upsilon,u_\upsilon)\right\}^{\frac{1}{2}} \tag{2.65}$$

$$= \eta^{\frac{1}{2}} \left\{(A_J u, A_J^{-1}R_{a,j}^{-1}u)\right\}^{\frac{1}{2}}\left\{\sum_{\upsilon\in\mathcal{N}_j}(A_J u_\upsilon,u_\upsilon)\right\}^{\frac{1}{2}} \tag{2.66}$$

$$= \eta^{\frac{1}{2}} \left\{(u, R_{a,j}^{-1}u)\right\}^{\frac{1}{2}}\left\{\sum_{\upsilon\in\mathcal{N}_j}(A_J u_\upsilon,u_\upsilon)\right\}^{\frac{1}{2}} \tag{2.67}$$

The above inequality works for arbitrary splitting, hence we have

$$\eta(R_{a,j}^{-1}u,u) \leq \sum_{\upsilon\in N_j} A_J(u_\upsilon,u_\upsilon) \tag{2.68}$$

For the choice $u_\upsilon = P_{j,\upsilon} P_j A_J^{-1} R_{a,j}^{-1} u$ we get

$$\eta(R_{a,j}^{-1}u, u) = \inf_{\substack{u_\upsilon \in V_{j,\upsilon} \\ \Sigma_\upsilon u_\upsilon = u}} \sum_{\upsilon \in N_j} A_J(u_\upsilon, u_\upsilon) \tag{2.69}$$

□

Lemma 4. *Given the local Helmholtz decomposition in* (2.55)*. For any* $u_\upsilon^\perp \in V_{j,\upsilon}$ *, there exists constant* C_1 *independent of multigrid level satisfying:*

$$\sum_{\upsilon \in \mathcal{N}_j} \left\| \nabla \cdot u_\upsilon^\perp \right\|^2 \leq C_1 \sum_{\upsilon \in \mathcal{N}_j} a_j(u_\upsilon^\perp, u_\upsilon^\perp) \tag{2.70}$$

Proof. It follows from Lemma 1 that the estimate $\left\| \nabla \cdot u^\perp \right\|^2 \leq C a_j(u^\perp, u^\perp)$ hold for all $u^\perp \in V_j$. It is easy to see that $V_{j,\upsilon}$ is a subspace of V_j for any υ, so the estimate are also valid on any patch. In 2-D case, one cell could at most be sharing by four patches (eight patches in 3D). Hence there exists a constant C_1 independent of multigrid level such that the estimates holds for the summation of local estimates. □

Proposition 3. *Assume* σ_j *is chosen sufficiently large, the following estimate holds on each level* j*. Given the overlapping subspace decomposition of* V_j *in 2.6 and the interior penalty bilinear form* $a_j(u, v)$ *in* (2.4)*. For any* $u \in V_j$*, there is a constant* C_2 *which is independent of multigrid level such that*

$$\sum_{\upsilon \in \mathcal{N}_j} a_j(u_\upsilon, u_\upsilon) \leq C_2 a_j(u, u) \tag{2.71}$$

Proof. For a fixed J, the penalty constant σ_j is of order $\frac{1}{h_J}$ which is chosen large enough on each level j to satisfy the requirement in the proof this lemma. The details can be found in [42, p. 1361]. □

Proof of Theorem 2. Recall the definition of A_J-orthogonal projection P_j and $P_{j,\nu}$ which restrict the projection on $\Omega_{j,\nu}$ (zero elsewhere). Following [11], we show that if $0 < \eta \leq 1/4$, the smoother $R_{a,j}$ satisfies the first condition in Theorem 2.

For $w \in V_j$

$$A_J([I - R_j A_j]w, w) = A_J(w, w) - \eta \sum_{v \in N_j} A_J(P_{j,v}w, w) \tag{2.72}$$

but

$$A_J(P_{j,v}w, w) = A_J(P_{j,v}w, P_{j,v}w) \leq A_J(w, w)^{\frac{1}{2}} A_J(P_{j,v}w, P_{j,v}w)^{\frac{1}{2}} \tag{2.73}$$

so

$$\sum_{v \in \mathcal{N}_j} A_J(P_{j,v}w, w) \leq \sum_{v \in \mathcal{N}_j} A_J(w, w) \leq 4A_J(w, w) \tag{2.74}$$

Hence the first hypothesis holds.

Thus, it remains to check the second condition which could be reduced to the following problem: for $u = (I - P_{j-1})w$ (where $w \in V_j$) with the decomposition $u = \sum_v u_v$, there is a constant C_a such that

$$\sum_{v \in \mathcal{N}_j} A_J(u_v, u_v) \leq C_a A_J(u, u) \tag{2.75}$$

Following Lemmas 1, 3, 4 and Proposition 3, we get:

$$\sum_{v\in\mathcal{N}_j} A_J(u_v,u_v) = \sum_{v\in\mathcal{N}_j} \left\{a_j(u_v,u_v) + \epsilon^{-1}(\nabla\cdot u_v, \nabla\cdot v_v)\right\} \tag{2.76}$$

$$= \sum_{v\in\mathcal{N}_j} \left\{a_j(u_v,u_v) + \epsilon^{-1}(\nabla\cdot u_v^{\perp}, \nabla\cdot u_v^{\perp})\right\} \tag{2.77}$$

$$\leq C_2 a_j(u,u) + \sum_{v\in\mathcal{N}_j} C_1 \frac{1}{\alpha}\epsilon^{-1} a_j(u_v^{\perp}, u_v^{\perp}) \tag{2.78}$$

$$\leq C_2 a_j(u,u) + \epsilon^{-1} C_1 \frac{1}{\alpha} a_j(u^{\perp}, u^{\perp}) \tag{2.79}$$

$$\leq C_2 a_j(u,u) + \epsilon^{-1} C_1 \frac{1}{\alpha}\frac{1}{\gamma_j} (\nabla\cdot u^{\perp}, \nabla\cdot u^{\perp}) \tag{2.80}$$

$$= C_2 a_j(u,u) + \epsilon^{-1} C_1 \frac{1}{\alpha}\frac{1}{\gamma_j} (\nabla\cdot u, \nabla\cdot u) \tag{2.81}$$

$$\leq \max\left\{C_2, C_1\frac{1}{\alpha}\frac{1}{\gamma_j}\right\} A_J(u,u) \tag{2.82}$$

$$= C_a A_J(u,u) \tag{2.83}$$

where $C_a = \max\left\{C_2, C_1\frac{1}{\alpha}\frac{1}{\gamma_j}\right\}$. □

Now set

$$\beta = \frac{1}{\eta} C_a \tag{2.84}$$

We have verified the two conditions in Proposition 2.

Lemma 5. *Given β_j above and $m(j)$ defined in 2.5, there is a constant $\hat{C}$ such that*

$$\frac{\beta_j}{2m(j)} \leq \hat{C} \tag{2.85}$$

Proof. We will discuss this inequality in two cases: first, if $\beta_j = \frac{1}{\eta}C_2$, then

$$\frac{\beta_j}{2m(j)} = \frac{\frac{1}{\eta}C_2}{2m_0 2^{J-j}} \leq \frac{\frac{1}{\eta}C_2}{2m_0} =: \hat{C} \tag{2.86}$$

On the other hand, if $\beta = \frac{1}{\eta}C_1\frac{1}{\alpha}\frac{1}{\gamma}_j$

$$\frac{\beta_j}{2m(j)} = \frac{C_1\frac{1}{\alpha}\frac{1}{c}\sqrt{2^{J-j}}}{2m_0 2^{J-j}} = \frac{C_1\frac{1}{\alpha}\frac{1}{c}}{2m_0\sqrt{2^{L-j}}} \leq \frac{C_1\frac{1}{\alpha}\frac{1}{c}}{2m_0} =: \hat{C} \tag{2.87}$$

□

2.7.1.2 Proof for multiplicative Schwarz smoother

In this subsection, we will check the two conditions in Proposition 2 for multiplicative smoother $R_{m,j}$ based some proposition and results in additive Schwarz smoother proof.

Proposition 4. *Given the additive smoother $R_{a,j}(defined\ in\ (2.26))$ and muliiplicative smoother $R_{m,j}(defined\ in\ (2.30))$, there is a constant ζ such that:*

$$(R_{a,j}v, v) \leq \zeta(R_{m,j}v, v) \quad for \quad all \quad v \in V_j \tag{2.88}$$

where ζ is a constant only depends on the overlap between the patches.

Proof. The proof of this proposition can be found in [11, p. 972]. □

Now we show that the smoother $R_{m,j}$ satisfies the first condition in Theorem 2. Recall the definition of A_J-orthogonal projection P_j, $P_{j,\nu}$ which restrict the projection on $\Omega_{j,\nu}$ (zero elsewhere) and the equation (2.32) given in Section 2.6. For $w \in V_j$

$$A_J([I - R_{m,j}A_j]w, w) = A_J(E_j^* E_j w, w) = A_J(E_j w, E_j w) \geq 0 \quad \forall w \in V_j \tag{2.89}$$

So the first hypothesis holds.

Thus, it remains to check the second condition: for $u = (I - P_{j-1})w$ (where $w \in V_j$) with the decomposition $u = \sum_v u_v$, there is a constant C_m independent of multigrid level j such that

$$(R_{m,j}^{-1}u, u) \leq C_m A_J(u, u) \tag{2.90}$$

Here we give a proof based on Proposition 4 and the additive smoother convergence result (2.75):

$$(R_{m,j}^{-1}u, u) = \sum_{v \in \mathcal{N}_j} A_J(P_{j,v}A_j^{-1}R_{m,j}^{-1}u, u_v) \tag{2.91}$$

$$\leq \left\{ \sum_{v \in \mathcal{N}_j} A_J(P_{j,v}A_j^{-1}R_{m,j}^{-1}u, A_j^{-1}R_{m,j}^{-1}u) \right\}^{\frac{1}{2}} \left\{ \sum_{v \in \mathcal{N}_j} A_J(u_v, u_v) \right\}^{\frac{1}{2}} \tag{2.92}$$

$$= \eta^{-\frac{1}{2}}(R_{a,j}R_{m,j}^{-1}u, R_{m,j}^{-1}u) \left\{ \sum_{v \in \mathcal{N}_j} A_J(u_v, u_v) \right\}^{\frac{1}{2}} \tag{2.93}$$

$$\leq \zeta^{-\frac{1}{2}}(R_{m,j}^{-1}u, u)^{\frac{1}{2}} A_J(u, u)^{\frac{1}{2}}. \tag{2.94}$$

Then, we take the square on both side of the above inequality and get

$$(R_{m,j}^{-1}u, u) \leq \frac{\zeta}{\eta} A_J(u, u) = C_m A_J(u, u). \tag{2.95}$$

where $C_m = \frac{\zeta}{\eta}$.

We have verified the two conditions in Proposition 2, thus Theorem 2 holds for multiplicative smoother $R_{m,j}$.

2.7.2 The mixed problem

Secondly, we will discuss the Stokes' equation in mixed variables (2.5). Set $X_{j,\epsilon} := \{(u_j, p_j) \in X_j : \nabla \cdot u_j = \epsilon p_j\}$. Now, it remains to show the equivalence between the multigrid algorithms.

Proposition 5. *The multigrid components fulfill the following properties:*

1. *The smoother $\mathcal{R}_j$ for the mixed problem defined in subection 2.6 preserves $X_{j,\epsilon}$. On the subspace it is equivalent to the smoother R_j in primal variables. This means for $(u_j, p_j) \in X_{j,\epsilon}$ and*

$$\begin{pmatrix} \hat{u}_j \\ \hat{p}_j \end{pmatrix} = \mathcal{R}_j \begin{pmatrix} u_j \\ p_j \end{pmatrix} \tag{2.96}$$

   there holds $(\hat{u_j}, \hat{p_j}) \in X_{j,\epsilon}$ and

$$\hat{u}_j = R_j u_j \tag{2.97}$$

2. *The prolongation $\mathcal{I}_{j-1}$ maps $X_{j-1,\epsilon}$ into $X_{j,\epsilon}$. On the subspace it is equivalent to the prolongation I_j in primal variables. This means for $(u_{j-1}, p_{j-1}) \in X_{j-1,\epsilon}$ and*

$$\begin{pmatrix} \hat{u}_j \\ \hat{p}_j \end{pmatrix} = \mathcal{I}_j \begin{pmatrix} u_{j-1} \\ p_{j-1} \end{pmatrix} \tag{2.98}$$

   there holds $(\hat{u}_j, \hat{p}_j) \in X_{j,\epsilon}$ and

$$\hat{u}_j = I_j(u_{j-1}) \tag{2.99}$$

3. *The coarse grid solution operator maps $X_{j-1,\epsilon}$ into $X_{j,\epsilon}$. On the subspace it is equivalent to the coarse grid solution operator in primal variables. This means for $(u_j, p_j) \in X_{j,\epsilon}$ and*

$$\begin{pmatrix} \hat{u}_{j-1} \\ \hat{p}_{j-1} \end{pmatrix} = \mathcal{A}_{j-1}^{-1}[\mathcal{I}_{j-1}]^t \mathcal{A}_j \begin{pmatrix} u_j \\ p_j \end{pmatrix} \tag{2.100}$$

there holds $(\hat{u}_{j-1}, \hat{p}_{j-1}) \in X_{j-1,\epsilon}$ and

$$\hat{u}_{j-1} = A_{j-1}^{-1}[I_{j-1}]^t A_j u_j \tag{2.101}$$

Proof. The proof of this proposition can be found for the operators there in [83, p. 93]. We do not provide it here since the arguments are purely linear algebra, and thus apply independent of the actual bilinear form. □

Theorem 3. *The multigrid algorithm in mixed variables preserves the space $X_{j,\epsilon}$. On this subspace it is equivalent to the multigrid algorithm in primal variables. This means for $(u_j, p_j) \in X_{j,\epsilon}$ and $(\hat{u}_j, \hat{p}_j) = \mathcal{B}_j(u_j, p_j)$ there holds $(\hat{u}_j, \hat{p}_j) \in X_{j,\epsilon}$ and*

$$\hat{u_j} = B_j u_j \tag{2.102}$$

where $\mathcal{B}_j$ and B_j are the corresponding multigrid operators for each algorithm.

Proof. The multigrid operator B_j fulfills the recursion

$$B_0 = A_0^{-1}, \tag{2.103}$$

$$B_j = (R_j)^{m_j}(I - I_j(I - (B_{j-1}))A_{j-1}^{-1}[I_{j-1}]^t A_j)(R_j)^{m_j}. \tag{2.104}$$

and the mixed operator $\mathcal{B}_j$ fulfills a corresponding one. Then we apply the above

proposition, and the theorem is proved by induction. □

(Note that $\mathcal{R}_j$ here refers to additive (defined in (2.24)) or multiplicative (defined in (2.27)) Schwarz smoother in the mixed formulation, and R_j refers to additive (defined in (2.26)) or multiplicative (defined in (2.30)) Schwarz smoother in the singularly perturbed form correspondingly.)

Finally, we can apply continuity arguments and pass to the limit $\epsilon = 0$, then we claim that for the incompressible case our algorithm also works well.

2.8 Numerical experiments for Stokes problem

We test the additive and multiplicative Schwarz methods which we have analyzed in the preceding subsection in order to ascertain that the contraction numbers are not only bounded away from one, but are actually small enough to make this method interesting. Furthermore, we conduct experiments, which go beyond our analysis, in particular regarding the choice of the penalty parameter and the number of smoothing steps on lower levels. The experimental setup for most of the tables is as follows: the domain is $\Omega = [-1, 1]^2$, the coarsest mesh $\mathbb{T}_0$ consists of a single cell $T = \Omega$. The mesh $\mathbb{T}_j$ on level j is obtained by dividing all cells in $\mathbb{T}_{j-1}$ into four quadrilaterals by connecting the edge midpoints. Thus, a mesh on level j has 4^j cells, and the length of their edges is 2^{1-j}. The right hand side is $f = (1, 1)$.

2.8.1 Additive Schwarz Smoother

In the subsection, the smoother choice in our multiword method is set to additive Schwarz smoother. For the relaxation parameter in the additive Schwarz method, we found that 0.5 is the value which provides the best results for all experimental setups, hence we keep it there in all the following experimental setups in this subsection.

In Table 2.1, we first test the additive Schwarz smoother using variable V-cycle

algorithm on a square domain with no-slip boundary condition. For the penalty constant in the DG form (2.4), we choose the penalty parameter as $\bar{\sigma}/h_J$, where $\bar{\sigma} = (k+1)(k+2)$, on the finest level J and all lower levels j. Results for different pairs of RT_k/Q_k are reported in the table which show the fast and uniform convergence.

level	RT_1	RT_2
3	4	4
4	4	4
5	4	4
6	4	4
7	4	4
8	4	5

Table 2.1: Number of iterations n_6 to reduce the residual by 10^{-6} with the variable V-cycle algorithm with penalty parameter dependent of the finest level mesh size (Additive Schwarz Smoother for Stokes).

In Table 2.2, we keep the same experimental setup and present iteration counts for the standard V-cycle algorithm with one and two pre- and post-smoothing steps, respectively. Although our analysis does not apply, we still observe uniform convergence results. We also see that the variable V-cycle with a single smoothing step on the finest level is as fast as the standard V-cycle with two smoothing steps, and thus the variable V-cycle is more efficient.

	$m(j)=1$		$m(j)=2$	
level	RT_1	RT_2	RT_1	RT_2
3	7	7	4	4
4	7	7	4	4
5	7	7	4	4
6	7	7	4	4
7	8	8	4	4
8	8	8	4	4

Table 2.2: Number of iterations n_6 to reduce the residual by 10^{-6} with the standard V-cycle iteration with one and two pre- and post-smoothing steps. Penalty parameter dependent of the finest level mesh size (Additive Schwarz Smoother for Stokes).

In Table 2.3, we test the variable and standard V-cycles with penalty parameters depending on the mesh level j, namely $\bar{\sigma}/h_j$ (where $\bar{\sigma}$ is a positive constant depending on the polynomial degree) in the DG form (2.4). While our convergence analysis does not cover this case either, we observe convergence rates equal to the case with inherited forms.

	variable		standard	
level	RT_1	RT_2	RT_1	RT_2
3	4	4	7	7
4	4	4	7	7
5	4	4	7	7
6	4	4	7	7
7	4	4	7	8
8	4	5	8	8

Table 2.3: Penalty parameter dependent on the mesh size of each level. Number of iterations n_6 to reduce the residual by 10^{-6} with variable and standard V-cycle iterations with $m(J) = 1$ (Additive Schwarz Smoother for Stokes).

In Table 2.4, we provide results with GMRES solver and $\mathcal{B}_J$ as preconditioner for different experimental setups as in Tables 2.1, 2.2 and 2.3 respectively. The second and third columns are results for variable V-cycle with penalty parameter dependent of the finest level mesh size. The fourth and fifth columns are the results for standard V-cycle with penalty parameter dependent of the finest level mesh size. The last two columns are the results for standard V-cycle with penalty parameter depend on the mesh size of each level. From this table, we see that the GMRES method, as expected, is faster in every case.

	variable		standard		noninherited	
level	RT_1	RT_2	RT_1	RT_2	RT_1	RT_2
3	2	2	2	2	2	2
4	3	3	3	3	3	3
5	3	3	4	3	4	4
6	3	3	5	4	5	5
7	3	3	5	5	5	5
8	5	4	6	6	8	6

Table 2.4: Number of iterations n_6 to reduce the residual by 10^{-6} with GMRES solver and preconditioner $\mathcal{B}_J$; variable and standard V-cycle with inherited forms, variable V-cycle with noninherited forms. One pre- and post-smoothing step on the finest level (Additive Schwarz Smoother for Stokes).

Finally, we finish our experiments for additive Schwarz smoother by applying our method on a non-simply connected domain. We choose a square with a square hole, namely the domain $\Omega = [-1,1] \setminus [-\frac{1}{3},\frac{1}{3}]$(see Figure 2.1). The coarse grid on level $j = 0$ consists of the squares of the form $[-1+\frac{2i}{3}, -1+\frac{2i+2}{3}] \times [-1+\frac{2j}{3}, -1+\frac{2j+2}{3}]$ with $0 \leq i,j \leq 2$, and with the index pair $(i,j) = (1,1)$ missing. We note that the Hodge decomposition in this case is more complicated due to the presence of harmonic forms. Nevertheless, the results in Table 2.5 for elements RT_1 and RT_2 show the same convergence rates as the simply connected case.

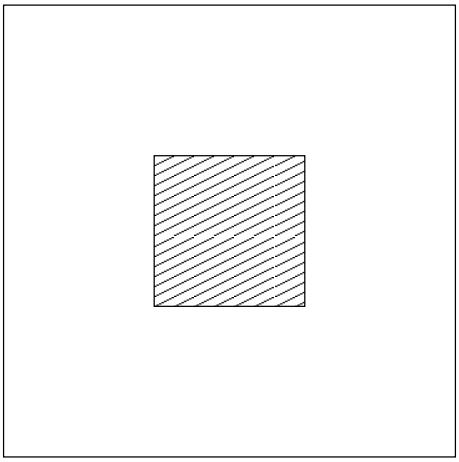

Figure 2.1: Domain with a square hole ($\Omega = [-1, 1] \setminus [-\frac{1}{3}, \frac{1}{3}]$)

Mesh size h	MG level	RT_1	RT_2
2/3	2	4	4
1/3	3	5	5
1/6	4	6	6
1/12	5	6	6
1/24	6	6	6
1/48	7	7	7

Table 2.5: Different finite element orders on the square domain $[-1, 1]^2$ with a square hole $[-1/3, 1/3]^2$ (Additive Schwarz Smoother for Stokes).

2.8.2 Multiplicative Schwarz Smoother

In this subsection, all the numerical experiments are based on the multiplicative Schwarz method. We set the relaxation parameter in multiplicative Schwarz smoother

to 1.0 as standard setup and keep it there in all the following experimental setups.

In Table 2.6, we first study convergence of the linear multigrid method (preconditioned Richardson iteration) with the multiplicative Schwarz smoother using a variable V-cycle algorithm on a square domain with no-slip boundary condition. The penalty constant in the DG form (2.4) is chosen as $\bar{\sigma}/h_J$, where $\bar{\sigma} = (k+1)(k+2)$, on the finest level J and all lower levels j. Results for pairs of RT_k/Q_k with orders k between one and three are reported in the table which show the fast and uniform convergence.

level	RT_1	RT_2	RT_3
3	5	5	5
4	6	6	7
5	6	6	6
6	5	5	6
7	5	5	6
8	5	5	6

Table 2.6: Number of iterations n_8 to reduce the residual by 10^{-8} with the variable V-cycle algorithm with penalty parameter dependent of the finest level mesh size (Multiplicative Schwarz Smoother for Stokes).

In Table 2.7, we keep the same experimental setup and present iteration counts for the standard V-cycle algorithm with one and two pre- and post-smoothing steps, respectively. Although convergence analysis has not been verified, we still observe uniform convergence results. We also see that the variable V-cycle with a single smoothing step on the finest level is as fast as the standard V-cycle with two smoothing

steps, and thus the variable V-cycle is more efficient.

	$m(j)=1$			$m(j)=2$		
level	RT_1	RT_2	RT_3	RT_1	RT_2	RT_3
3	5	5	5	3	3	3
4	6	6	7	5	5	5
5	6	6	7	5	5	6
6	6	6	7	5	5	6
7	7	7	7	5	5	6
8	7	7	7	6	6	6

Table 2.7: Number of iterations n_8 to reduce the residual by 10^{-8} with the standard V-cycle iterationwith one and two pre- and post-smoothing steps. The penalty parameter dependent of the finest level mesh size (Multiplicative Schwarz Smoother for Stokes).

In Table 2.8, we test the variable and standard V-cycles with penalty parameters depending on the mesh level j, namely $\bar{\sigma}/h_j$ (where $\bar{\sigma}$ is a positive constant depending on the polynomial degree) in the DG form (2.4). While convergence analysis has not been finished either, we still observe convergence rates equal to the case with inherited forms.

	variable			standard		
level	RT_1	RT_2	RT_3	RT_1	RT_2	RT_3
3	6	6	6	6	6	6
4	6	6	6	6	6	7
5	6	6	6	6	6	7
6	5	5	6	6	6	7
7	5	5	6	6	6	7
8	5	5	6	6	6	7

Table 2.8: Penalty parameter dependent on the mesh size of each level. Number of iterations n_8 to reduce the residual by 10^{-8} with variable and standard V-cycle iterations with $m(J) = 1$ (Multiplicative Schwarz Smoother for Stokes).

In Table 2.9, we provide results with GMRES solver and $\mathcal{B}_J$ as preconditioner for different experimental setups as in Table 2.6, 2.7 and 2.8 respectively. The second to fourth columns are results for variable V-cycle with penalty parameter dependent of the finest level mesh size. The fifth and seventh columns are the results for standard V-cycle with penalty parameter dependent of the finest level mesh size. The last three columns are the results for standard V-cycle with penalty parameter depend on the mesh size of each level. From this table, we see that the GMRES method, as expected, is faster in every case.

	variable			standard			noninherited		
level	RT_1	RT_2	RT_3	RT_1	RT_2	RT_3	RT_1	RT_2	RT_3
3	2	2	2	2	2	2	3	3	3
4	3	3	4	4	4	4	5	5	5
5	5	5	5	5	5	5	5	5	5
6	4	4	5	5	5	5	5	5	5
7	4	4	5	5	5	5	5	5	5
8	5	4	5	5	5	5	5	5	5

Table 2.9: Number of iterations n_8 to reduce the residual by 10^{-8} with GMRES solver and preconditioner $\mathcal{B}_J$; variable and standard V-cycle with inherited forms, variable V-cycle with noninherited forms. One pre- and post-smoothing step on the finest level (Multiplicative Schwarz Smoother for Stokes).

In Table 2.10, we provide results in three dimensions for variable V-cycle methods with the same penalty parameter as we choose in Table 2.1. We keep the similar experimental setups: domain $\Omega = [-1, 1]^3$ and right hand side $f = (1, 1, 1)$. We observe the similar fast and uniform convergence performance as in 2D cases.

	Richardson		GMRES	
level	RT_1	RT_2	RT_1	RT_2
2	1	1	1	1
3	5	5	4	4
4	6	5	4	4
5	6	5	4	4

Table 2.10: Three-dimensional domain. Number of iterations n_8 to reduce the residual by 10^{-8} with the variable V-cycle algorithm with penalty parameter dependent of the finest level mesh size (Multiplicative Schwarz Smoother for Stokes).

Finally we run some tests on a non-simply connected domain again. We choose the same a square with a square hole(see Figure 2.1) as in Subsection 2.8.1 .We note that the Hodge decomposition in this case is more complicated because of the presence of harmonic forms. Nevertheless, the results in Table 2.11 for elements RT_1 and RT_2 show the same convergence rates as the simply connected case in Table 2.6, 2.7 and 2.8.

	variable						standard					
Solver	Richardson			GMRES			Richardson			GMRES		
MG level	RT_1	RT_2	RT_3	RT_1	RT_2	RT_3	RT_1	RT_2	RT_3	RT_1	RT_2	RT_3
2	6	6	7	4	4	4	6	6	7	4	4	4
3	6	6	6	4	4	5	7	7	7	5	5	5
4	6	6	6	4	4	5	7	7	7	5	5	5
5	5	5	6	4	4	5	7	7	7	5	5	5
6	5	5	6	4	4	5	7	7	7	5	5	5
7	5	5	6	4	4	5	7	7	7	5	5	5

Table 2.11: Number of iterations n_6 to reduce the residual by 10^{-8}, different finite element orders and solvers on the domain with hole $[-1,1]^2 \setminus [-1/3,1/3]^2$ (Multiplicative Schwarz Smoother for Stokes).

2.9 Conclusion

In this section, we have investigated smoothers based on the ones introduced by Arnold, Falk, and Winther for problems in H^{div} in a variable V-cycle preconditioner for the Stokes system. We presented the convergence analysis and showed uniform contraction independent on the mesh level. In numerical experiments we showed that the contraction is not only uniform, but also very fast, thus making our method a feasible solver or preconditioner.

In theory, the performance of the smoother relies on an exact sequence property of finite element spaces.Our experiments with the Taylor–Hood elements, where the method fails, demonstrate that this is not an artifact of the analysis, but that the technique does not work due to the lack of an exact Hodge decomposition and nested divergence free subspaces.

3. THE COUPLING OF STOKES AND DARCY FLOW

3.1 Introduction

As the continuation of Section 2, we will raise the bar and start tackling the relatively complicated problem - the coupling of Stokes and Darcy flow - with our multigrid preconditioning method. The coupling of Stokes and Darcy model has been brought up in many real world applications, for instance, filtration problem and groundwater contamination, etc. This model, also known as multi-domain problem with multi-physics, frequently lead to a very singular and stiff system due to the varying governing equations in different regions. Specifically, it is composed of free flow region (Stokes) and porous media flow region (Darcy) with certain interface condition.The difficulty of this type problem has been described in Section 1.1. There are several works available for the coupled Stokes and Darcy equations in current literature(cf., [7, 26, 63, 97]. Here, we mainly follow the strongly conservative finite element approach proposed by Kanschat and Riviere in [63]. For the velocity, we will use divergence conforming finite elements in the whole domain. In addition, we apply the discontinuous Galerkin method with interior penalty method [10] in Stokes region and a mixed method in Darcy region. At the interfaces between Stokes region and Darcy region, the Beavers-Joseph-Saffman conditions [16] are applied. Then the multigrid preconditioner is built for the coupled discrete system based on a overlapping domain decomposition Schwarz smoother. In this section, our main emphasis will be posed on the efficiency of multigrid solver for the coupled system from the computational viewpoint.

The plan of the section is given as follows. In Subsection 3.2, we introduce the model problem and provide the H^{div}-conforming discontinuous Galerkin finite ele-

ment discretization. The multigrid framework for the coupled system is described in Subsection 3.3. Subsection 3.4 shows two series of numerical experiments. Finally, we conclude this section in Subsection 3.5.

3.2 Model problem and discretization

Let $\Omega = \Omega_S \bigcup \Omega_D$ be the union of two bounded connected polygonal subdomains such that $\Omega_S \bigcap \Omega_D = \emptyset$. Here, Ω_S and Ω_D represents Stokes regime and Darcy regime,respectively. The interface between them are denoted by Γ_{SD}. The external boundaries are given as follows:

$$\Gamma_S = \partial\Omega \cap \partial\Omega_S, \quad \Gamma_D = \partial\Omega \cap \partial\Omega_D \tag{3.1}$$

In Ω_D, we consider Darcy's equations as the mixed formulation of an elliptic problem :

$$\begin{aligned} \kappa^{-1}u_D + \nabla p_D &= 0 \quad \text{in} \quad \Omega_D, \\ \nabla\cdot u_D &= f_D \quad \text{in} \quad \Omega_D, \\ u_D \cdot n &= 0 \quad \text{on} \quad \Gamma_D, \end{aligned} \tag{3.2}$$

where u_D and p_D represents the fluid velocity and pressure, $0 < \kappa \in L^\infty(\Omega)$ is the permeability coefficient and $f_D \in L^2(\Omega)$ models sinks and sources in the porous medium.

In Ω_S, we consider the following Stokes system:

$$\begin{aligned} -\nabla\cdot(2\mu\epsilon(u_S)) + \nabla p_S &= f_S, \quad in \quad \Omega_S \\ \nabla\cdot u_S &= 0, \quad in \quad \Omega_S \\ u_S &= 0, \quad on \quad \Gamma_S \end{aligned} \tag{3.3}$$

where $\epsilon(u_S) = \frac{1}{2}(\nabla u_S + (\nabla u_S)^T)$ is the deformation tensor, u_S and p_S represents the fluid velocity and pressure, $\mu > 0$ is the viscosity coefficient and $f_D \in L^2(\Omega)$ is a body force.

At the interface Γ_{SD}, we apply the Beavers-Joseph-Saffman transmissibility condition(cf. [16]):

$$\begin{cases} u_S \cdot n = u_D \cdot n, \\ p_S - \mu\epsilon(u_S)n \cdot n = p_D, \\ \gamma\kappa^{-\frac{1}{2}} u_S \cdot \tau - \mu\epsilon(u_S)n \cdot \tau = 0. \end{cases} \tag{3.4}$$

where n and τ be the unit normal and tangential vectors to Γ_{SD}(we assume that n points outward of Ω_S) and γ is the phenomenological friction coefficient.

We still use the hierarchy mesh $\{\mathbb{T}_j\}_{j=0,\dots,J}$ and choose the Raviart–Thomas space[81], but we point out that any pair of velocity spaces V_j and pressure spaces Q_j is admissible, if this relation

$$\nabla \cdot V_j = Q_j \tag{3.5}$$

holds.

With the same notation for integral forms defined in Subsection 2.2, the discrete weak formulation of the coupled system now reads: find $(u_j, p_j) \in V_j \times Q_j$, such that for all test functions $v_j \in V_j$ and $q_j \in Q_j$ there holds

$$\mathcal{A}_j^{SD}\left(\begin{pmatrix} u_j \\ p_j \end{pmatrix}, \begin{pmatrix} v_j \\ q_j \end{pmatrix}\right) \equiv a_j^{SD}(u_j, v_j) - (p_j, \nabla \cdot v_j) - (q_j, \nabla \cdot u_j) = \mathcal{F}^{SD}(v_j, q_j). \tag{3.6}$$

where

$$\begin{cases} a_j^{SD}(u,v) := a_j^S(u,v)_{\Omega_S} + (\kappa^{-1}u,v)_{\Omega_D} + \gamma\kappa^{-\frac{1}{2}}\big\langle u_S\cdot\tau, v_S\cdot\tau\big\rangle_{\Gamma_{SD}}, \\ a_j^S(u,v) := 2\mu(\epsilon(u),\epsilon(v))_{\mathbb{T}_j^S} - 4\mu\big\langle\{\!\{\epsilon(u)\}\!\},\{\!\{v\otimes\mathbf{n}\}\!\}\big\rangle_{\mathbb{F}_j^S} - 4\mu\big\langle\{\!\{\epsilon(v)\}\!\},\{\!\{u\otimes\mathbf{n}\}\!\}\big\rangle_{\mathbb{F}_j^S} \\ \qquad\qquad + 4\sigma_j\big\langle\{\!\{u\otimes\mathbf{n}\}\!\},\{\!\{v\otimes\mathbf{n}\}\!\}\big\rangle_{\mathbb{F}_j^S} + 2\sigma_j\big\langle u,v\big\rangle_{\Gamma_S} \\ \mathcal{F}^D(v,q) := (f_S,v)_{\Omega_S} + (f_D,q)_{\Omega_D}. \end{cases} \tag{3.7}$$

(Note that the penalty parameter σ_j is chosen large enough such that a^{SD} is positive definite)

The existence and uniqueness of such solutions, as well as the $inf-sup$ condition, have been verified by Kanschat and Riviere in [63].

3.3 Multigrid method for the coupled Stokes/Darcy problem

We use the similar nested finite element spaces associated with hierarchies of meshes $\{\mathbb{T}_j\}$. We define the action of the multigrid preconditioner $\mathcal{B}_j^{SD} : X_j \to X_j$ recursively as the multigrid V-cycle with $m(j) \geq 1$ pre- and post-smoothing steps. Let $\mathcal{R}_j^{SD}$ be a suitable smoother. Let $\mathcal{B}_0^{SD} = (\mathcal{A}_0^{SD})^{-1}$. The definition of multigrid framework for the preconditioner $\mathcal{B}_j^{SD}$ can be found in Subsection 2.5.

Remark 3. *(Choice of V-cycle method and smoother) From the extensive numerical evidences in Subsection 2.8, we conclude that variable V-cycle is more efficient than standard V-cycle algorithm. In addition, we choose the overlapping multiplicative Schwarz smoother over the additive one for the same reason based on our observations.*

The variable V-cycle preconditioner $\mathcal{B}_J^{SD}$ for the coupled system $\mathcal{A}_J^{SD}$ is defined

in the following:

$$\begin{pmatrix} u_{k+1} \\ p_{k+1} \end{pmatrix} = \begin{pmatrix} u_k \\ p_k \end{pmatrix} + \mathcal{B}_J^{SD} \left(\mathcal{F}_J^{SD} - \mathcal{A}_J^{SD} \begin{pmatrix} u_k \\ p_k \end{pmatrix} \right) \tag{3.8}$$

The symmetric multiplicative Schwarz smoother $\mathcal{R}^{\mathcal{SD}}{}_{m,j}$ is defined by

$$\begin{aligned} \mathcal{R}_{m,j}^{SD} &= (\mathcal{I} - \mathcal{E}_j^{SD})(\mathcal{A}^{SD})_j^{-1}, \\ \mathcal{E}_j^{SD} &= \left(\mathcal{I} - \mathcal{P}_{j,1}^{SD}\right) \ldots \left(\mathcal{I} - \mathcal{P}_{j,N}^{SD}\right) \ldots \left(\mathcal{I} - \mathcal{P}_{j,1}^{SD}\right). \end{aligned}$$

where $\mathcal{P}_{\ell,v}^{SD}$ is the Ritz projection.

3.4 Numerical results for Coupled Stokes/Darcy problem

In the section, we provides two sets of ideal experimental setups that describe flow around a river bed. We set the viscosity coefficient $\mu = 1$ in free flow region (Stokes) and the friction coefficient $\gamma = 0.1$ in the Beavers-Joseph-Saffman interface condition. Then, we test for different permeability coefficients in the porous media region (Darcy). Since this dissertation mainly aims at efficient preconditioning techniques, our numerical results here will only focus on the computational performance in terms of iteration steps.

Remark 4. *(Choice of parameters) The penalty parameter σ_j in the DG formulation is chosen as $\sigma_j = (k+1)(k+2)/h_J$ (h_J is the mesh size on the finest level) for optimal convergence results. The reduction residual is set to 10^{-6} in the GMRES solver. The choice of finite elements are $RT_1 \times DGQ_1$. We use uniform mesh with uniform refinement from coarse to fine grids.*

The experimental setup in this section is given by: the domain is $\Omega = [-1, 1]^2$ and the right hand side is $f = (1, 1)$.

In the first set of experimental setups, we want to simulate flow through porous medium on some simple geometries (see Figure 3.1) which consist of free flow region (Stokes), porous medium flow region (Darcy) and intermediate region (Brinkman). Note that in Brinkman region the viscosity and permeability coefficients are from the neighboring Stokes or Darcy region.

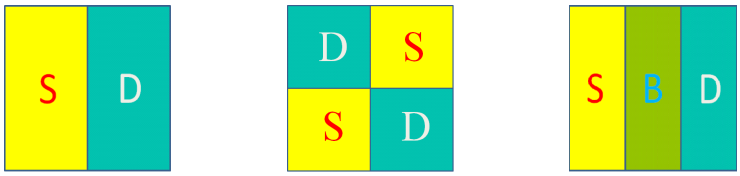

(a) Two layers (S-D)

(b) Two layers (Checkerboard)

(c) Three layers (S-B-D)

Figure 3.1: Flow through porous medium. Inflow and outflow boundary conditions left and right, no slip at top and bottom

MG level	10^{-1}	10^{-2}	10^{-3}	10^{-4}
2	15	15	15	15
3	17	17	17	17
4	19	19	19	19
5	19	20	19	20
6	20	20	20	20
7	20	20	20	20
8	20	20	20	20

Table 3.1: Two layers geometry with permeability on the right columns using RT1 and DGQ1

MG level	10^{-1}	10^{-2}	10^{-3}	10^{-4}
2	14	15	17	18
3	16	17	20	23
4	17	19	22	29
5	19	19	22	30
6	19	20	21	29
7	20	21	22	30
8	20	21	22	30

Table 3.2: Checkerboard geometry with permeability on the right columns using RT1 and DGQ1

MG level	10^{-1}	10^{-2}	10^{-3}	10^{-4}
2	14	15	16	18
3	16	18	20	22
4	17	19	21	23
5	19	20	21	24
6	20	20	21	25
7	21	21	22	25
8	21	21	22	25

Table 3.3: Three layers geometry with permeability on the right columns using RT1 and DGQ1

In Table 3.1, 3.2 and 3.3 , we provide results of flow through porous medium. For

a fixed permeability in the porous medium (any column in the table), we observe uniform convergence rate with respect to multigrid levels (mesh refinements). For a fixed multigrid level (any row in the table), we observe robust convergence rate with respect to permeability coefficients.

In the second set of experimental setups, we add channels for flow through porous medium(see Figure 3.2). We also assume continuity between Stokes-Brinkman and Darcy-Brinkman interfaces.

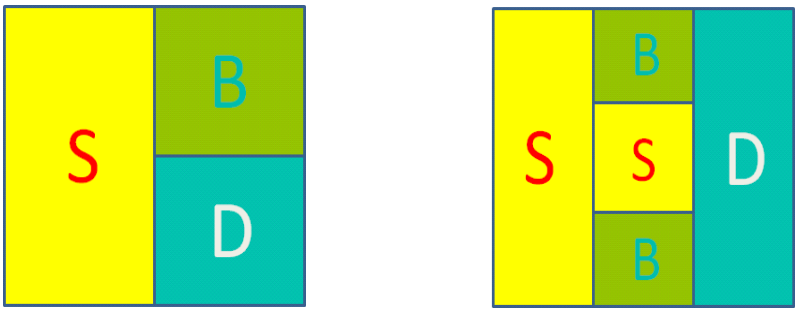

(a) Triple (b) Ring

Figure 3.2: Flow through a channel. Inflow and outflow boundary conditions left and right, no slip at top and bottom

MG level	10^{-1}	10^{-2}	10^{-3}	10^{-4}
2	19	20	23	26
3	21	22	24	26
4	25	26	25	27
5	26	27	26	29
6	27	28	28	30
7	27	28	29	31
8	27	28	29	31

Table 3.4: Triple geometry with permeability on the right columns using RT1 and DGQ1

MG level	10^{-1}	10^{-2}	10^{-3}	10^{-4}
2	21	21	23	24
3	24	22	24	27
4	25	23	26	29
5	27	26	27	31
6	27	27	30	33
7	27	28	30	33
8	27	28	30	33

Table 3.5: Ring geometry with permeability on the right columns using RT1 and DGQ1

In Table 3.4 and 3.5, we provides results of flow through porous medium with

channels. For a fixed permeability in the porous medium (any column in the table), we obtain uniform convergence rate with respect to mesh refinements. For a fixed multigrid level (any row in the table), we obtain robust convergence rate with respect to permeability coefficients.

Furthermore, we observe the robustness with respect to different experimental setups, thus making our method a decent solver to the coupling of Stokes and Darcy problems.

3.5 Conclusions

In this section, we have applied geometric multigrid method into to the coupling of Stokes and Darcy problem. In theory, the analysis of this type of multigrid method for the coupled systems is still under development. In our case, the interface terms make it difficult to prove the stable decomposition which is a key step in the whole analysis. While we can not prove the convergence for the proposed multigrid method, we still obtain uniform and robust convergence performance. These positive indications lead us to the continuation of our discovery for Brinkman's model which will be shown in next section.

4. FLOW PROBLEMS IN HETEROGENEOUS POROUS MEDIA

4.1 Introduction

Fluid flow through highly porous media (such as glass wool, industrial filter or natural reservoirs, see Figure 1.1 - 1.3) modeled by Darcy's Law or Brinkman's equations has many industrial applications. Often, these porous media materials display heterogeneity over a wide range of length-scales (see Remark 2). In relatively larger pores, flows are often governed by Stokes' Law. The smaller pores are treated as permeable medium and flows through these pores are described by Darcy's law:

$$\nabla p = -\frac{\mu}{\kappa} u \tag{4.1}$$

where p is the pressure, μ is the fluid viscosity, κ is the permeability and u is the fluid velocity. However, the Darcy's law alone is not sufficient to meet the continuity conditions of the velocity and the shear stress at the interfaces between the larger pores and permeable medium (smaller pore regions). The Brinkman's equations [23] are considered to be an adequate model introduced as follows:

$$\nabla p = -\frac{\mu}{\kappa} u + \mu \triangle u \tag{4.2}$$

As we mentioned in Subsection 1.1, the heterogeneity of the porous media frequently leads to extremely ill-conditioned discrete systems arising from approximations of Darcy's and Brinkman's equations. Corresponding efficient solvers are in high demand, thus make it an area of active research (*e.g.*, [8, 9, 5, 6, 17, 39, 38, 45, 57, 54, 53, 55, 52, 47, 46, 68, 79, 72, 90, 91], most of them based on finite volume or finite element method).

A high proportion of these finite element approaches are based on H^{div}-conforming finite elements [31, 30, 94] for two reasons: globally divergence-free discrete velocity field for incompressible flows and a more dynamic treatment of boundary conditions. Thus, preconditioning in H^{div} become popular for for flows problem (such as Darcy flow, Stokes flow, coupled Stokes and Darcy flow and Brinkman equations) in mixed finite element discretizations (*e.g.*, [11, 12, 51, 67]).

From multiscale standpoint, several precondtioners originated from multiscale finite element have been introduced(*e.g.*, [1, 34, 33, 35, 43, 49, 77, 78, 101]). From multigrid preconditioning point of view, both algebraic and geometric multigrid methods with classical smoothers are often not suitable for H^{div} problems, thus two groups of appropriate smoothers have been developed to resolve the issue. There are the $Hiptmair - Xu$ smoothers for algebraic multigrid methods and the $Arnold - Falk - Winther$ smoothers for geometric multigrid methods, respectively. Recently, algebraic multigrid preconditioners for Brinkman's equations in heterogeneously porous media have been investigated in several works (*e.g.*, [36, 37, 92, 90, 91]), whereas geometric multigrid preconditioners in this field can not be found in current literature (see two reasons listed in Section 1). In this Section, we will investigate a geometric multigrid preconditioner with Arnold-Falk-Winther type smoothers for flow problems in heterogeneously porous media.

This section is organized as follows. In Subsection 4.2.1, we mainly introduce the Brinkman models with corresponding the H^{div}-conforming finite element discretizations. The multigrid preconditioning method as well as domain decomposition smoother are derived in Subsection 4.4. Subsection 4.5 is devoted to the convergence analysis of the proposed Brinkman solver. We next present extensive numerical experiments for different porous media geometries in Subsection 4.6. This section finishes with a brief conclusion in Subsection 4.7.

4.2 Flow models and corresponding discretizations

4.2.1 The Brinkman model

Recall the model introduced in Section 1.1. Assume Ω be a bounded Lipschitz domain in $\mathbb{R}^d$ with dimension $d = 2, 3$, the Brinkman equations read:

$$\begin{aligned} -\mu\triangle u + \kappa(x)u + \nabla p &= f, \quad in \quad \Omega \\ \nabla\cdot u &= 0, \quad in \quad \Omega \\ u &= u^B, \ on \quad \partial\Omega \end{aligned} \tag{4.3}$$

The coefficient μ (positive constant) is the fluid viscosity and the coefficient $\kappa(x)$ is the inverse permeability of the porous medium. Assume there are two positive constants κ_{min} and κ_{max} such that

$$0 < \kappa_{min} \leq \kappa(x) \leq \kappa_{max} < \infty \ , \forall \ x \in \Omega \tag{4.4}$$

The nature solution spaces for the system are $H^1(\Omega)$ and $L^2_0(\Omega)$ for velocity and pressure, respectively. We will use no-slip boundary conditions here for simplicity, although we point out that other well posed boundary conditions do not pose a problem. In the reminder of this section, we will denote κ as $\kappa(x)$ for simplicity.

We apply the same hierarchy of meshes $\{\mathbb{T}_j\}_{j=0,\ldots,J}$ and finite element spaces (V_j, Q_j) for the discretization of 1.1. Here, we still choose Raviart–Thomas space RT_k in [81] (Note that any finite element space that satisfy $\nabla\cdot V_j = Q_j$ also works, *i.e.*, $Brezzi - Douglas - Marini$ (BDM) space). We will use the same notation for integral forms on $\mathbb{T}_j$ and $\mathbb{F}_j$ defined in Section 2.1.

Since $V_j \not\subseteq H^1(\Omega)$ is a non-conforming space, it can not be used directly to discretize 1.1. Thus, we apply an interior penalty DG formulation to the discretization

of the elliptic operator following [10, 75, 30, 64, 63]. Let T_1 and T_2 be two mesh cells with a joint face F, and let u_1 and u_2 be the traces of a function u on F from T_1 and T_2, respectively. On this face F, we recall the averaging and jump operator

$$\{\!\{u\}\!\} = \frac{u_1 + u_2}{2}, \ \textit{and} \ \ [\![u]\!] = u_1 - u_2 \tag{4.5}$$

The interior penalty bilinear form now reads:

$$\begin{aligned} a_j^B(u,v) =& \mu\big(\nabla u, \nabla v\big)_{\mathbb{T}_j} + (\kappa^{-1}u, v)_{\mathbb{T}_j} + 4\mu\big\langle \sigma_J \{\!\{u \otimes \mathbf{n}\}\!\}, \{\!\{v \otimes \mathbf{n}\}\!\}\big\rangle_{\mathbb{F}_j^i} \\ & - 2\mu\big\langle \{\!\{\nabla u\}\!\}, \{\!\{\mathbf{n} \otimes v\}\!\}\big\rangle_{\mathbb{F}_j^i} - 2\mu\big\langle \{\!\{\nabla v\}\!\}, \{\!\{\mathbf{n} \otimes u\}\!\}\big\rangle_{\mathbb{F}_j^i} \\ & + 2\mu\big\langle \sigma_J u, v\big\rangle_{\mathbb{F}_j^\partial} - \mu\big\langle \partial_n u, v\big\rangle_{\mathbb{F}_j^\partial} - \mu\big\langle \partial_n v, u\big\rangle_{\mathbb{F}_j^\partial}. \end{aligned} \tag{4.6}$$

Following Subsection 2.2, the operator "$\otimes$" denotes the Kronecker product of two vectors and the term $4\{\!\{u \otimes \mathbf{n}\}\!\} : \{\!\{v \otimes \mathbf{n}\}\!\}$ represents the product of the jumps of u and v.

The discrete weak formulation of (1.1) reads now: find $(u_j, p_j) \in V_j \times Q_j$, such that for all test functions $v_j \in V_j$ and $q_j \in Q_j$ there holds

$$\mathcal{A}_j^B\left(\begin{pmatrix} u_j \\ p_j \end{pmatrix}, \begin{pmatrix} v_j \\ q_j \end{pmatrix}\right) \equiv a_j^B(u_j, v_j) - \big(p_j, \nabla\cdot v_j\big) - \big(q_j, \nabla\cdot u_j\big) = \mathcal{F}(v_j, q_j) \equiv \big(f, v_j\big). \tag{4.7}$$

Here, σ_J is chosen large enough such that a^B is positive definite independent of multigrid level j. Specifically, following the discretization of Stokes equations (2.5), we choose the same penalty parameter $\sigma_j = O(\bar{\sigma}/h_J)$, where $\bar{\sigma}$ is a positive constant depending on the polynomial degree and h_J is the mesh size on the finest level J.

The energy norm on V_j is defined by:

$$\|\!|u|\!\|^2 = \big\|u\big\|_{1,j}^2 + \big\|u\big\|_{\kappa,L^2(\Omega)}^2 \tag{4.8}$$

$$\big\|u\big\|_{1,j}^2 = \big\|\nabla u\big\|_{\mathbb{T}_j}^2 + \sigma_J \big\|[\![u]\!]\big\|_{\mathbb{F}_j^i}^2 + 2\sigma_J \big\|u\big\|_{\mathbb{F}_j^\partial}^2 \tag{4.9}$$

where $\big\|[\![u]\!]\big\|_{\mathbb{F}_j^i}$ denote the jump of traces of a discontinuous function u across interior faces of the mesh and $\big\|u\big\|_{\kappa,L^2(\Omega)}^2 := \int_\Omega \kappa^{-1} u \cdot u dx$.

Now, we start investigating the properties of the discretization given by (4.7).

Lemma 6. *(Boundedness) There exists a constant ξ_1 independent of multigrid level j such that for any u and v in V_j we have*

$$\big|a_j^B(u,v)\big| \leq \xi_1 \, |\!|\!|u|\!|\!| \, |\!|\!|v|\!|\!| \tag{4.10}$$

Proof. Recall the results for Stokes problem in [30, 31, 48, 63], we have

$$\big|a_j^S(u,v)\big| \leq \xi_{S1} \big\|u\big\|_{1,j} \big\|v\big\|_{1,j} \tag{4.11}$$

where $a_j^S(\cdot,\cdot)$ refers to the bilinear form for the elliptic operator defined in (2.4) in Subsection 2.2 and ξ_{S1} is independent of j but may depend on σ_J. Now, by $Cauchy - Schwarz$ inequality we get

$$\begin{aligned}
\big|a_j^B(u,v)\big| &= \big|\mu a_j^S(u,v) + (\kappa^{-1}u, v)\big| && (4.12)\\
&\leq \mu \big|a_j^S(u,v)\big| + \big|(\kappa^{-1}u, v)\big| && (4.13)\\
&\leq \mu \xi_{S1} \big\|u\big\|_{1,j} \big\|v\big\|_{1,j} + \big\|u\big\|_{\kappa,L^2(\Omega)} \big\|v\big\|_{\kappa,L^2(\Omega)} && (4.14)\\
&\leq \xi_1 \, |\!|\!|u|\!|\!| \, |\!|\!|v|\!|\!| && (4.15)
\end{aligned}$$

where ξ_1 is independent of j but may depend on μ and σ_J. $\square$

Lemma 7. *(Stability) There exists a constant ξ_2 independent of multigrid level j such that for any $u \in V_j$ we have*

$$a_j^B(u,u) \geq \xi_2 \, |||u|||^2 \tag{4.16}$$

Proof. Similarly, we recall the *stability* result for Stokes problem

$$a_j^S(u,u) \geq \xi_{S2} \big\|u\big\|_{1,j}^2 \tag{4.17}$$

where ξ_{S2} is independent of j. With the above estimate, we have

$$\begin{aligned} a_j^B(u,u) &= \mu a_j^S(u,u) + \big\|u\big\|_{\kappa,L^2(\Omega)}^2 && (4.18)\\ &\geq \mu\xi_{S2}\big\|u\big\|_{1,j}^2 + \big\|u\big\|_{\kappa,L^2(\Omega)}^2 && (4.19)\\ &\geq \min\{\mu\xi_{S2}, 1\}\left(\big\|u\big\|_{1,j}^2 + \big\|u\big\|_{\kappa,L^2(\Omega)}^2\right) && (4.20)\\ &= \xi_2 \, |||u|||^2 && (4.21) \end{aligned}$$

where $\xi_2 = \min\{\mu\xi_{S2}, 1\}$ which is independent of j. $\square$

Proposition 6. *(Inf-sup condition) For any pressure function $q \in Q_j$, there exists a velocity function $v \in V_j$, satisfying*

$$\sup_{v \in V_j} \frac{\big(q, \nabla\cdot v\big)}{|||v|||} \geq \xi_j \big\|q\big\|_{L^2(\Omega)} > 0 \tag{4.22}$$

where $\xi_j = \bar{c}\sqrt{\frac{h_J}{h_j}} = \bar{c}\sqrt{2^{j-J}}$ and $\bar{c}$ is a constant independent of the multigrid level j.

Proof. Recall our assumption for κ: $0 < \kappa_{min} \leq \kappa \leq \kappa_{max} < \infty$. Thus, we have

$$\frac{1}{\kappa_{max}}\|v\|_{L^2(\Omega)} \leq \|v\|^2_{\kappa,L^2(\Omega)} \leq \frac{1}{\kappa_{min}}\|v\|_{L^2(\Omega)} \tag{4.23}$$

Combining Proposition 2.9 (Inf - sup condition for Stokes problem) and (4.23), we are thus left with

$$\sup_{v\in V_j} \frac{(q, \nabla\cdot v)}{|||v|||} \geq \bar{c} \sup_{v\in V_j} \frac{(q, \nabla\cdot v)}{\|v\|_{1,j}} \geq \bar{c}\gamma_j \|q\|_{L^2(\Omega)} > 0 \tag{4.24}$$

Therefore,

$$\sup_{v\in V_j} \frac{(q, \nabla\cdot v)}{|||v|||} \geq \xi_j \|q\|_{L^2(\Omega)} > 0 \tag{4.25}$$

where $\xi_j = \bar{c}\gamma_j = \bar{c}\sqrt{\frac{h_J}{h_j}} = \bar{c}\sqrt{2^{j-J}}$ and $\bar{c}$ is a constant independent of the multigrid level j but may depend on h_0 and κ_{min}. □

4.2.2 The Darcy model

As we mentioned in Subsection 1.1, Darcy's equations is a simplification of the Brinkman model. This can be done by simply setting viscosity parameter $\mu = 0$ and adjust the boundary condition, which reads now:

$$\begin{aligned} \kappa^{-1}u + \nabla p &= f, \quad in \quad \Omega \\ \nabla\cdot u &= 0, \quad in \quad \Omega \\ u\cdot n &= g, \quad on \quad \partial\Omega \end{aligned} \tag{4.26}$$

where the coefficient κ is the inverse permeability under the same assumption (see (4.4)). We choose a standard variational formulation for the system (4.26): $V \times Q$ for velocity and pressure respectively. The discrete weak formulation for 4.26 can easily

follow (4.7), thus make it a mixed formulation solving by H^{div}-conforming finite elements. The discussion on the existence and uniqueness of such solutions, as well as the corresponding $inf-sup$ condition, can be found in [20, 21]. For the finite element space, we still apply Raviart Thomas space for the same reason as in Subsection 4.2.1. The multigrid preconditioning framework for Darcy's model is similar to that of Brinkman's model, thus we will not repeat here. Besides, the corresponding analysis work with constant permeability coefficient has been shown in [11, 12]. But for the varying coefficient case, the proof of convergence is still under development and will not be discussed in this Section. Instead, we exhibit the robustness and efficiency of the proposed multigrid solver only from the computational standpoint. In this Section, the analysis work for Brinkman's equations will become our focus.

4.3 The singular perturbed problem

In order to prove convergence of our multigrid method for the Brinkman's equations, we follow the analysis sketch in Subsection 2.7. First, we prove the estimates robust with respect to the parameter ϵ of the nearly incompressible problem: find $(u_j, p_j) \in V_j \times Q_j$ such that for all $(v_j, q_j) \in V_j \times Q_j$ there holds

$$\mathcal{A}_j^B \left(\begin{pmatrix} u_j \\ p_j \end{pmatrix}, \begin{pmatrix} v_j \\ q_j \end{pmatrix} \right) + \epsilon\big(p_j, q_j\big) = \mathcal{F}(v_j, q_j). \tag{4.27}$$

The associated singular perturbed problem reads: find $u_j \in V_j$ such that for all $v_j \in V_j$ there holds

$$A_{j,\epsilon}^B(u_j, v_j) = a^B(u_j, v_j) + \frac{1}{\epsilon}(\nabla \cdot u_j, \nabla \cdot v_j) = F(v_j). \tag{4.28}$$

4.4 Multigrid method

Here, we take the same nested finite element spaces associated with hierarchies of meshes $\{\mathbb{T}_j\}$. The action of the multigrid preconditioner $\mathcal{B}_j^B : X_j \to X_j$ are recursively defined as the multigrid V-cycle with $m(j) \geq 1$ pre- and post-smoothing steps. Let $\mathcal{R}_j^B$ be a suitable smoother. Let $\mathcal{B}_0^B = (\mathcal{A}_0^B)^{-1}$. For $j \geq 1$, the action of $\mathcal{B}_j^B$ on a vector $\mathcal{F}_j = (f_j, g_j)$ can be defined similarly as in Subsection 2.5.

In this section, we also choose variable V-cycle method in order to prove the convergence analysis following Subsection 2.7. We refer to $\mathcal{B}_J^B$ as the variable V-cycle preconditioner of $\mathcal{A}_J^B$. The iteration

$$\begin{pmatrix} u_{k+1} \\ p_{k+1} \end{pmatrix} = \begin{pmatrix} u_k \\ p_k \end{pmatrix} + \mathcal{B}_J^B \left(\mathcal{F}_J^B - \mathcal{A}_J^B \begin{pmatrix} u_k \\ p_k \end{pmatrix} \right) \tag{4.29}$$

is the V-cycle iteration.

Here, we define a class of smoothing operators $\mathcal{R}_j^B$ based on a subspace decomposition of the space X_j. Let $\mathcal{N}_j$ be the set of vertices in the triangulation $\mathbb{T}_j$, and let $\mathbb{T}_{j,\upsilon}$ be the set of cells in $\mathbb{T}_j$ sharing the vertex υ. They form a triangulation with $N (N > 0)$ subdomains or patches which we denote by $\{\Omega_{j,\upsilon}\}_{\upsilon=1}^N$.

The subspace $X_{j,\upsilon} = V_{j,\upsilon} \times Q_{j,\upsilon}$ consists of the functions in X_j with support in $\Omega_{j,\upsilon}$. Note that this implies homogeneous slip boundary conditions on $\partial\Omega_{j,\upsilon}$ for the velocity subspace $V_{j,\upsilon}$ and zero mean value on $\Omega_{j,\upsilon}$ for the pressure subspace $Q_{j,\upsilon}$. The Ritz projection $\mathcal{P}_{j,\upsilon}^B : X_j \to X_{j,\upsilon}$ is defined by the equation

$$\mathcal{A}_j^B\big(\mathcal{P}_{j,\upsilon}^B \begin{pmatrix} u_j \\ p_j \end{pmatrix}, \begin{pmatrix} v_{j,\upsilon} \\ q_{j,\upsilon} \end{pmatrix}\big) = \mathcal{A}_j^B\big(\begin{pmatrix} u_j \\ p_j \end{pmatrix}, \begin{pmatrix} v_{j,\upsilon} \\ q_{j,\upsilon} \end{pmatrix}\big) \qquad \forall \begin{pmatrix} v_{j,\upsilon} \\ q_{j,\upsilon} \end{pmatrix} \in X_{j,\upsilon}. \tag{4.30}$$

The additive Schwarz $\mathcal{R}^B_{a,j}$is defined as

$$\mathcal{R}^B_{a,j} = \eta \sum_{\upsilon \in \mathcal{N}_j} \mathcal{P}^B_{j,\upsilon} (\mathcal{A}^B)^{-1}_j. \tag{4.31}$$

where $\mathcal{P}^B_{j,\upsilon}$ is the Ritz projection.

The symmetric multiplicative Schwarz smoother $\mathcal{R^B}_{m,j}$ is defined by

$$\begin{aligned} \mathcal{R}^B_{m,j} &= (\mathcal{I} - \mathcal{E}^B_j)(\mathcal{A}^B)^{-1}_j, \\ \mathcal{E}^B_j &= \left(\mathcal{I} - \mathcal{P}^B_{j,1}\right) \ldots \left(\mathcal{I} - \mathcal{P}^B_{j,N}\right) \ldots \left(\mathcal{I} - \mathcal{P}^B_{j,1}\right). \end{aligned}$$

The corresponding singularly perturbed forms $R^B_{a,j}$, $R^B_{m,j}$ and $P^B_{j,\upsilon}$ are defined similarly .

4.5 Convergence analysis for Brinkman's equations

In this Subsection, we prove the convergence for the variable V-cycle multigrid method with additive Schwarz smoother (the multiplicative version proof can easily follow according to subsection 2.7.1.2). Specifically, we follow the analysis approach for the Stokes' problem and verify the corresponding propositions and theorems for Brinkman's equations. In this proof, we assume κ is a constant over the whole domain. About the regularity assumption, we point out that Ω is bounded and convex. Without loss of generality, we assume viscosity $\mu = 1$ in this proof.

Theorem 4. *The multilevel iteration $\mathcal{I} - \mathcal{B}^B_J \mathcal{A}^B_J$ with the variable V-cycle operator $\mathcal{B}^B_J$ defined in Subsection 4.4 employing the smoother $\mathcal{R}^B_j$ is a contraction with contraction number independent of the mesh level J.*

Proof. Following Subsection 2.7, we first prove the convergence for the corresponding singularly perturbed problem. Then, we verify the equivalence between singularly

perturbed and mixed problems. Finally, the estimate uniform in ϵ gives us that $\mathcal{I} - \mathcal{B}_J^B \mathcal{A}_J^B$ is a contraction with contraction number independent of the mesh level J when $\epsilon \to 0$. □

In the reminder of this subsection, we will verify the conditions in the proof of 4.

Proposition 7. *Given $u \in (I - P_{j-1})V_j$ and the inverse permeability coefficient κ is a positive constant. There exist a decomposition $u = \sum_v u_v$ and a constant C independent of multigrid level j and κ such that*

$$\sum_{v \in \mathcal{N}_j} (\kappa^{-1} u_v, u_v) \leq C(\kappa^{-1} u, u) \tag{4.32}$$

Proof. This proof easily follows from standard scaling argument:

$$\sum_{v \in \mathcal{N}_j} (\kappa^{-1} u_v, u_v) = \kappa^{-1} \sum_{v \in \mathcal{N}_j} (u_v, u_v) \tag{4.33}$$

$$\leq \kappa^{-1} C(u, u) \tag{4.34}$$

$$= C(\kappa^{-1} u, u) \tag{4.35}$$

Where C is independent of j and κ but depending on shape regularity of the mesh. □

By Proposition 2, it remains to check: for $u = (I - P_{j-1})w$ (where $w \in V_j$) with the decomposition $u = \sum_v u_v$, there is a constant C_B independent of multigrid level j, permeability coefficient κ^{-1} and ϵ such that

$$\sum_{v \in \mathcal{N}_j} A_J^B(u_v, u_v) \leq C_B A_J^B(u, u) \tag{4.36}$$

By the convergence results of Stokes problem in Subsection 2.7 and Proposition 7, we get

$$\sum_{v\in\mathcal{N}_j} A_J^B(u_v,u_v) = \sum_{v\in\mathcal{N}_j} \left\{a_j^B(u_v,u_v) + \epsilon^{-1}(\nabla\cdot u_v, \nabla\cdot u_v)\right\} \tag{4.37}$$

$$= \sum_{v\in\mathcal{N}_j} \left\{a_j^S(u_v,u_v) + (\kappa^{-1}u_v,u_v) + \epsilon^{-1}(\nabla\cdot u_v, \nabla\cdot u_v)\right\} \tag{4.38}$$

$$\leq \sum_{v\in\mathcal{N}_j} \left\{a_j^S(u_v,u_v) + \epsilon^{-1}(\nabla\cdot u_v, \nabla\cdot v_v) + (\kappa^{-1}u_v,u_v)\right\} \tag{4.39}$$

$$= \sum_{v\in\mathcal{N}_j} (A_J^S(u_v,u_v) + (\kappa^{-1}u_v,u_v)) \tag{4.40}$$

$$\leq C_S A_J^S(u,u) + C(\kappa^{-1}u,u) \tag{4.41}$$

$$= C_S a^S(u,u) + \epsilon^{-1}(\nabla\cdot u, \nabla\cdot u) + C(\kappa^{-1}u,u) \tag{4.42}$$

$$\leq \max\{C_S, C\}\, a^B(u,u) + \epsilon^{-1}(\nabla\cdot u, \nabla\cdot u) \tag{4.43}$$

$$\leq \max\{C_S, C\}\, A^B(u,u) \tag{4.44}$$

$$= C_B A_J^B(u,u). \tag{4.45}$$

where $C_B = \max\{C_S, C\}$. (Note that $a_j^S(\cdot,\cdot)$ and $A_J^S(\cdot,\cdot)$ refer to the bilinear form and singularly perturbed form defined in (2.4) and (2.13) for the Stokes' equations, C_S is the constant in additive Schwarz smoother proof in Subsection 2.7.1.1.)

Therefore, we verify that the singularly perturbed operator $I - B_J^B A_J^B$ is a contraction with contraction number independent of the mesh level J. Finally, we complete the convergence analysis of our multigrid method for Brinkman's equations by Theorem 3 and Theorem 4.

4.6 Numerical results

In this subsection, we show the computational performance of our Brinkman solver and Darcy solver through substantial numerical experiments. First of all, we

introduce two sets of porous media geometries (2-D case) arising from the industry-related problems which are recently treated as the most popular criteria for evaluating flow solvers in heterogeneously porous media. The first set is given by four geometries as follows:

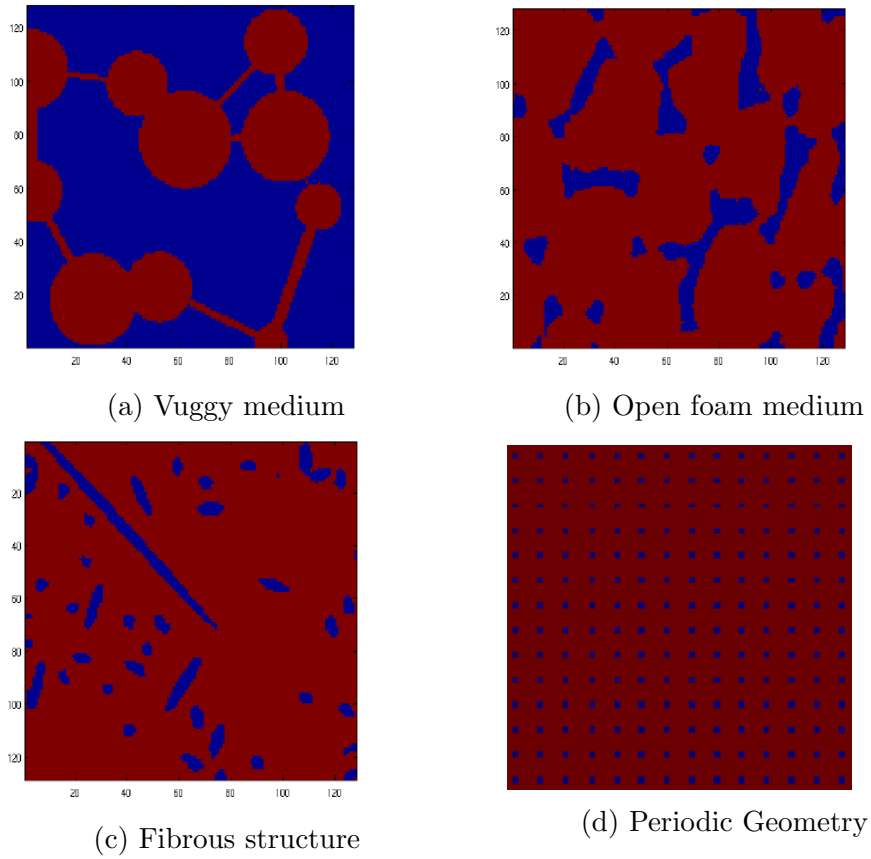

(a) Vuggy medium

(b) Open foam medium

(c) Fibrous structure

(d) Periodic Geometry

Figure 4.1: Different 2D geometries of some porous media

1. Figure 4.1(a) describes vuggy media related to oil reservoirs (cf. [80]). This type of media have a large amount of relatively big vugs or cavities (the red bubble regions) which are usually considered as pure fluid regions. The blue background region represents the lowly permeable material. Note that these

vugs are mutually connected by different "channels" or "pipes". These "channels" make the vugs highly permeable regions against the lowly permeable background. The interface between two vugs and left boundary will be the entrance for the inflows in our numerical experiments.

2. Figure 4.1(b) is one cross section of the three dimensional industrial foam (see Figure 1.2). It is also referred to open foam which has many applications in industry such as filtration, heat exchanges, etc (cf. [70, 88]). Same as Figure 4.1(a), the blue regions here represent the lowly permeable material while the red background stands for free flow region. Unlike the connected vugs in Figure 4.1(a), these low permeability regions are mostly disconnected. Hence, this type of materials, as known as filters, allow viscous fluid to flow through while blocking relative large particles.

3. In Figure 4.1(c), we introduce the fibrous structure media which is also considered as one kind of filters. The blue region here refers to lowly permeable material and the red one refers to the opposite. The only difference between open foam media (Figure 4.1(b)) and fibrous structure media is that the former has more complicated geometry.

4. Figure 4.1(d) depicts an artificial simple periodic geometry. There are 16×16 small square subdomains with length $1/32$ (the blue squares) inside the a unit square. We assume these blue squares are the obstacles in the medium and the background for flow regions. This type of artificial geometries have been treated as classical test cases in many works related to highly heterogenous and highly porous mediums (*e.g.*, [2, 53, 55, 76, 95]).

Remark 5. *(Some comments about Figure 4.1) In the figures of Figure 4.1, the*

coefficients associated with high and low permeability fields (red and blue regions) will be assigned depending on different experimental setups. Besides, the three geometries Figure 4.1(a)-(c) are given by 128×128 *matrices and generated through MATLAB plots. Hence, we need associate the permeability field according to these geometries. In our implementation, we start with initial mesh* 128×128 *and assign the coefficients to each cell corresponding to each geometry information. The details about coefficients upscaling and downscaling are discussed in Remark 7.*

The second set goes here:

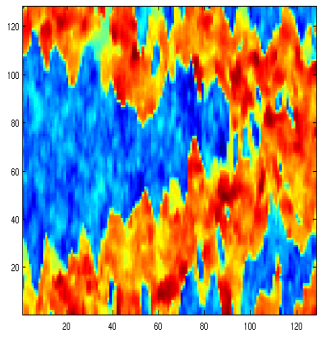

(a) SPE10 Slice 44 with logarithmic plot

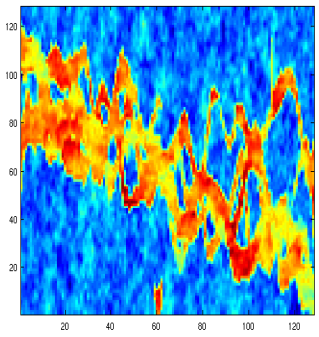

(b) SPE10 Slice 49 with logarithmic plot

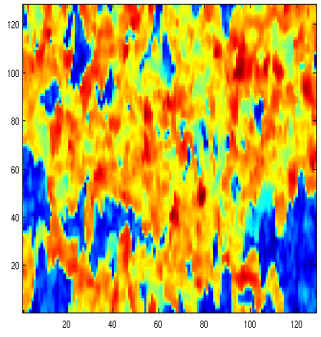

(c) SPE10 Slice 54 logarithmic plot

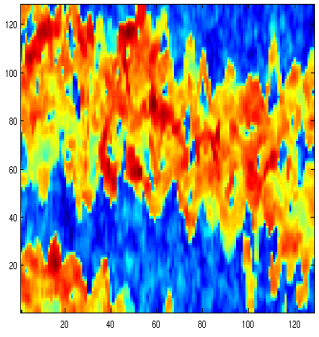

(d) SPE10 Slice 74 logarithmic plot

Figure 4.2: cross sections of 3D SPE 10 Benchmark geometry

Figure 4.2(a)-(d) are two dimensional intersections(rescaled) of the natural reservoir model in Tenth SPE Comparative Solution Project (cf. [28]). One of the main purposes of this project is to compare the performances of upscaling related methods for two phase flow in the oil reservoir shown in Figure 1.3. As we remarked in Section 1, there are 85 distinct layers within two general categories. The top 35 layers represent a prograding near shore environment where the porosity is relatively low. The bottom 50 layers represent a fluvial fan with clearly visible channels, thus making it an interesting geometry for the modeling of fluid flows. We first start with a few two dimensional layers in the bottom part of the the original 3D reservoir data. We choose these slices because they display diverse geological features. Slice 54 (Figure 4.2(b)) is almost dominated by the red and yellow regions (highly permeable region) compared to Slice 44 ,49 and 74. One may expect better upscaling results due to simplicity of the geometry of this slice. In Slice 44 (Figure 4.2(a)), we observe two highly permeable regions (marked by red color) channels which are partially connected with top, right and bottom boundaries of the geometry. The interface boundaries between highly and lowly permeable regions are typically difficult to capture by upscaling methods. In Slice 49 and 74 (Figure 4.2(b)), the main highly permeable regions locate in the channel that connect the left and right boundaries of the geometry. They are somewhat similar to Slice 44 as only the difference lies in the shape of highly permeable channels. Hence, both Slice 44, Slice 49 and Slice 74 are considered more complicated geometries than Slice 54 in terms of coefficient upscaling. Furthermore, all the figures are plotted under logarithmic scale and the actual contrast between coefficients is rather high, up to 10^8.

Finally, we bring out the three dimensional natural reservoir model(see Figure 1.3).

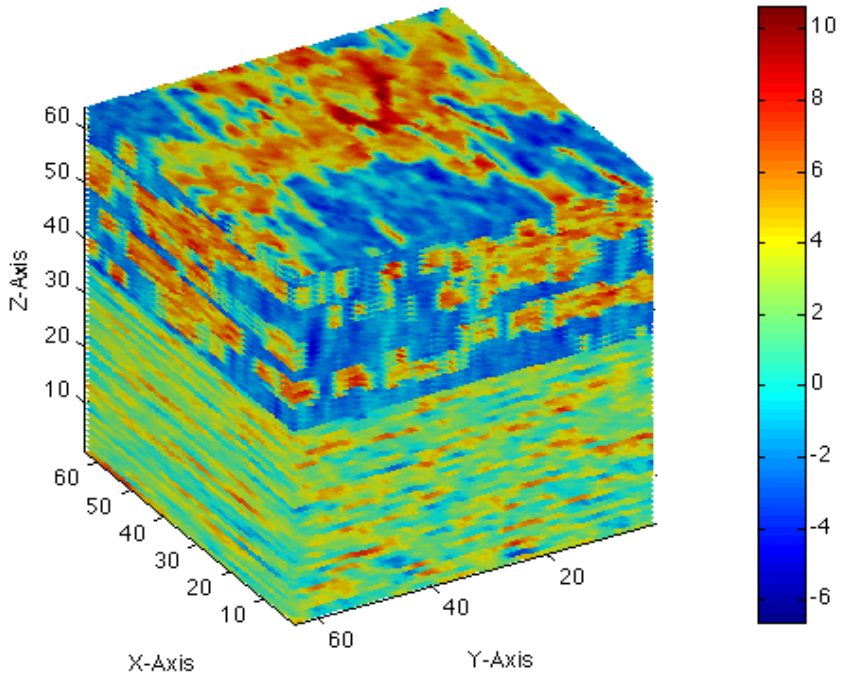

Figure 4.3: SPE 10 Benchmark natural reservoir model

Remark 6. *(Description of the geometry in Figure 4.3) Figure 4.3 depicts the rescaled three dimensional SPE10 benchmark natural reservoir model. We pick 64 layers from the original dataset (32 layers from each category) reshape each layer to* 64×64*, thus make it a three dimensional geometry with size* $64 \times 64 \times 64$*. As we pointed out in the description of 2D SPE 10 geometries, a half of the dataset represents a prograding near shore environment with rather low porosity, which is not perfect model for fluid flow simulation. Thus, we reverse these layers (with respect to the* $Z - Axis$*) and make the fluvial fan part on the top in order to observe better visual effects from the numerical simulations.*

Since our method is built on multilevel framework, it is necessary to point out the upscaling and downscaling schemes with respect to coefficients on coarse and

fine grids (Note: in our 2D experiments the initial mesh is given as 128×128 grid in order to load the permeability data (128×128) correspondingly, and our method is still capable of efficient computation after a couple of uniform refinements). More specifically, we have the following multilevel discrete systems:

$$\mathcal{A}_j^B \left(\begin{pmatrix} u_j \\ p_j \end{pmatrix}, \begin{pmatrix} v_j \\ q_j \end{pmatrix} \right) = \mathcal{F}(v_j, q_j). \tag{4.46}$$

on each level j.

Remark 7. *(Upscaling and downscaling schemes with respect to permeability field) Though upscaling techniques play a crucial role in multiscale methods, its impact on our the method is less dominant from preconditioning perspective. Actually, we use a very computationally cheap but effective upscaling scheme here: arithmetic averaging (see Figure 4.4(a)). The downscaling is just simple inheritance as shown in Figure 4.4(c).*

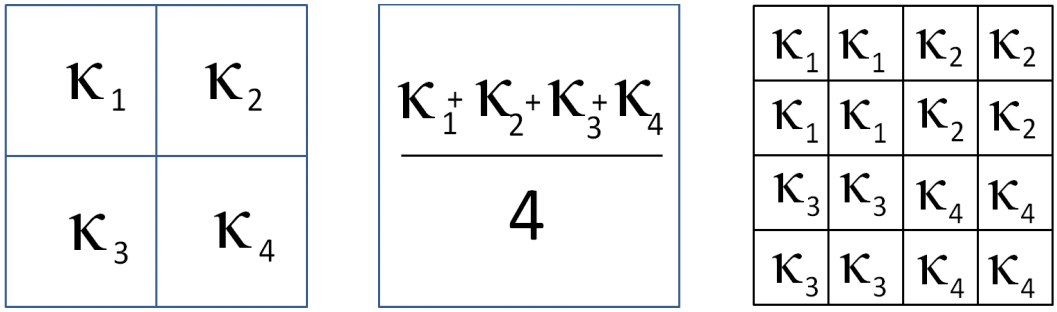

(a) a patch from initial mesh

(b) the immediate parent cell of Figure 4.4(a)

(c) the children of the patch in Figure 4.4(a)

Figure 4.4: Upscaling and downscaling with respect to coefficients

In the following next two subsections, we exhibit numerical experiments based on the two and three dimensional geometries in Figure 4.1 - 4.3 . For the details of parameter choice in multigrid method, we follow the same options as in Subsection 3.3 (see Remark 3 - 4). All the experimental setups in this section are performed on the two dimensional domain $\Omega = [0,1] \times [0,1]$.

4.6.1 Experiments with Darcy solver

In this subsection, we only focus on the performance of Darcy solver for flows in heterogeneously porous media geometries and it will be self-evident on some rather simple geometries.

Example 1. *(Darcy - geometries from Figure 4.1) The corresponding geometries are: vuggy media, open foam, fibrous media and periodic geometry. According to Remark 5, we need to assign the permeability coefficients for highly and lowly permeable regions for different experimental setups. The details about experimental setup in this example are given as follows: Inhomogeneous Neumman boundary condition:* $g = \binom{1}{0} \times n$*, right hand side* $f \equiv 0$*,* $\kappa = 1$ *in the red regions (highly permeable) and different* κ - 10^4 , 10^5 *and* 10^6 - *in the blue regions (low permeable).*

By this setup, we depict a fluid flow that moves from the left boundary to right boundary through different porous media modeled by Darcy's law. Specifically, we are interesting in the performance of the proposed Darcy solver with respect to different permeability contrasts.

	Vuggy medium			Open foam			Fibrous media			Periodic		
Mesh size	10^4	10^5	10^6	10^4	10^5	10^6	10^4	10^5	10^6	10^4	10^5	10^6
1/128	15	16	17	11	12	14	11	11	12	8	11	15
1/256	14	15	16	11	12	13	10	11	11	8	10	14
1/512	13	15	16	11	11	13	10	10	10	7	10	14

Table 4.1: Darcy solver on different geometries - Permeability contrast on the right columns

In Table 4.1, we provide the convergence results for the Darcy solver on four different geometries (see Figure 4.1). On each geometry, for a fixed permeability contrast (any column), we observe uniform convergence rate with respect to mesh refinements (multigrid levels); for a fixed multigrid level (any row), we observe robust convergence rate with respect to permeability contrasts. From any row of the whole table, we observe robust performance with respect to the geometries of the porous media. In addition to convergence results, it is necessary to present the numerical solutions on for different permeability contrasts on each geometry because one could barely have access to the corresponding analytical solutions. For simplicity, we only show two components of our solutions for each experimental setup: the first component of velocity u_1 and pressure component p. They are given in Figure 4.5 - 4.6.

Example 2. *(Darcy - Nature reservoir geometry in SPE 10) The corresponding geometries are: slice 44, 49, 54 and 74 of the SPE 10 geometries in Figure 4.2. In these geometries, the permeability fields are give in the dataset, thus will be directly assigned on the initial mesh in an appropriate order.*

The details about experimental setup in this example are given as follows: Inhomogeneous Neumann boundary condition: $u^B = \binom{1}{0} \times n$, *right hand side* $f \equiv 0$.

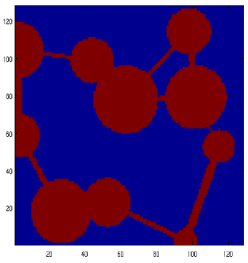

(a) Vuggy medium

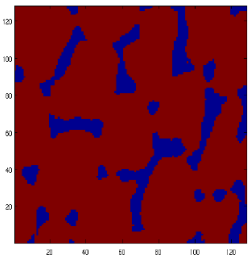

(b) Open foam

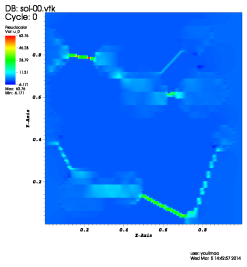

(c) permeability contrast 10^4 - u_1

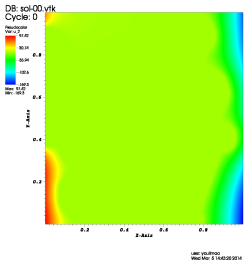

(d) permeability contrast 10^4 - p

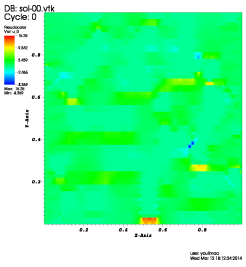

(e) permeability contrast 10^4 - u_1

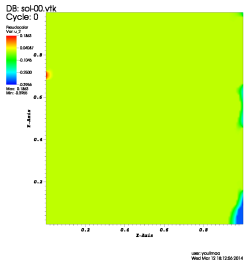

(f) permeability contrast 10^4 - p

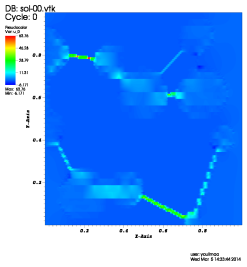

(g) permeability contrast 10^5 - u_1

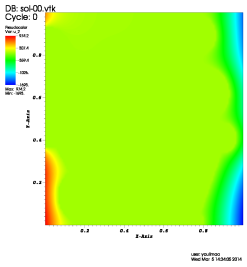

(h) permeability contrast 10^5 - p

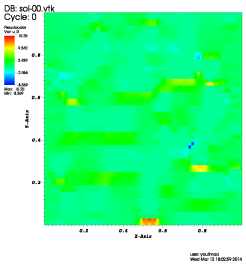

(i) permeability contrast 10^5 - u_1

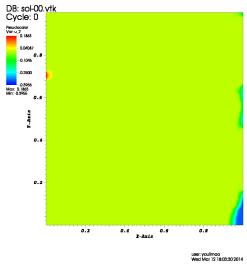

(j) permeability contrast 10^5 - p

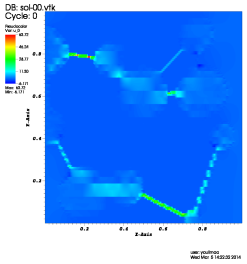

(k) permeability contrast 10^6 - u_1

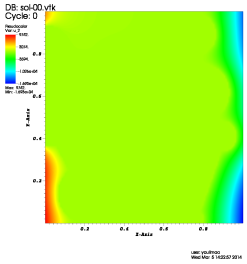

(l) permeability contrast 10^6 - p

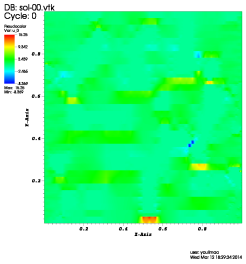

(m) permeability contrast 10^6 - u_1

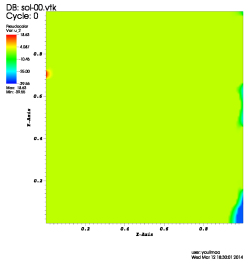

(n) permeability contrast 10^6 - p

Figure 4.5: (Darcy - Vuggy medium and open foam) numerical solution

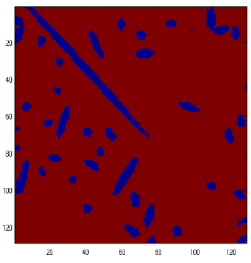

(a) Fibrous medium

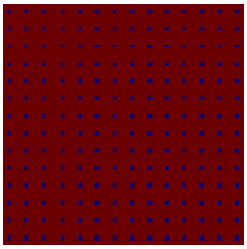

(b) Periodic geometry

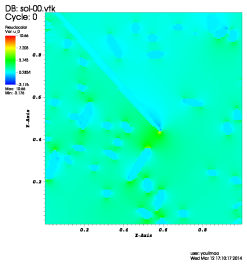

(c) permeability contrast 10^4 - u_1

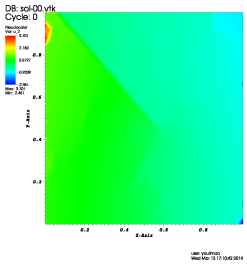

(d) permeability contrast 10^4 - p

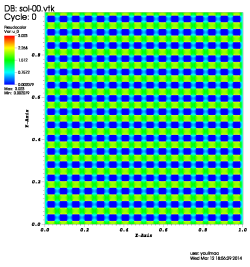

(e) permeability contrast 10^4 - u_1

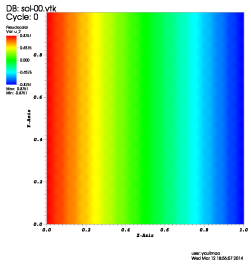

(f) permeability contrast 10^4 - p

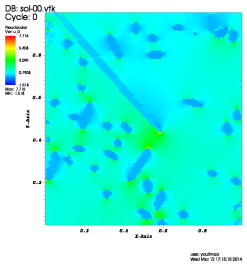

(g) permeability contrast 10^5 - u_1

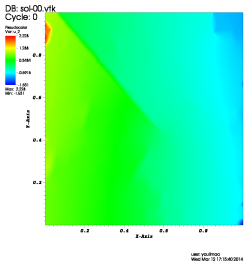

(h) permeability contrast 10^5 - p

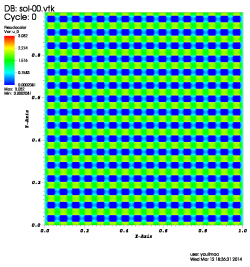

(i) permeability contrast 10^5 - u_1

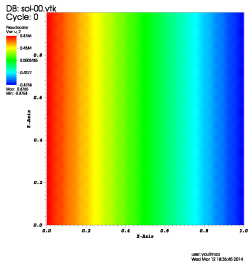

(j) permeability contrast 10^5 - p

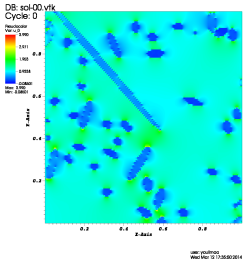

(k) permeability contrast 10^6 - u_1

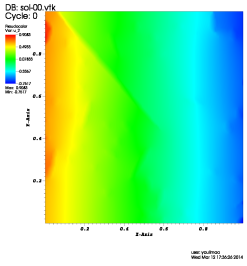

(l) permeability contrast 10^6 - p

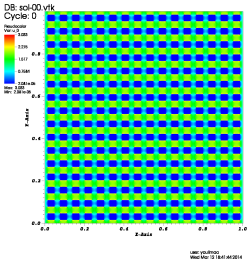

(m) permeability contrast 10^6 - u_1

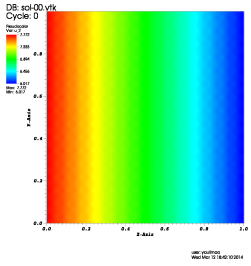

(n) permeability contrast 10^6 - p

Figure 4.6: (Darcy - Fibrous medium and periodic geometry) numerical solution

By this setup, we depict a fluid flow (oil or water) inside the natural reservoirs modeled by Darcy's law in two dimension. Specifically, we are interested in the performance of our multigrid solver for Darcy's equations with respect to different finite element orders and different slices (diverse geometry features) of the three dimensional nature reservoir.

	Slice 44		Slice 49		SPE 54		SPE 74	
Mesh size	RT_0	RT_1	RT_0	RT_1	RT_0	RT_1	RT_0	RT_1
1/128	30	36	33	41	28	32	31	38
1/256	24	30	27	33	20	28	25	31
1/512	19	26	22	29	17	24	20	28

Table 4.2: Darcy solver on SPE 10 geometries - Different finite orders on the right columns

In Table 4.2, we exhibit the convergence results for the Darcy solver on SPE 10 geometries. For a fixed slice (any column), we discern optimal convergence rate with respect to mesh refinements, which is a pleasant surprise. The reason for this phenomenon will be given in detail in Remark 8. For a fixed multigrid level, we also observe robust results with respect to diverse geometries. In addition, we notice the robustness of our solver with respect to different finite element orders. Besides, the results also coincide with our prediction about the geometries: slice 44, 48 and 74 are more complex geometries than slice 54. Similarly, we will show the corresponding numerical solutions in Figure 4.7 - 4.8.

Remark 8. *(on optimal convergence results on the fine levels) From the results in Table 4.1 and 4.2, we have noticed that the convergence rates on fine levels become*

superior, especially in Table 4.2. The reason for that is the preconditioner become more superior as we refine the mesh due to the upscaling and downscaling schemes defined in Remark 7.

From the numerical solutions in Figure 4.5 - 4.8, we discern that the velocity as well as pressure components are not well represented around the interfaces between free flow and porous media flow regions. This is because viscous effects are neglected in Darcy's model as we discussed in Section 1. Thus here we experimentally verified that Darcy's model is not appropriate on highly heterogeneous and highly porous media. In spite of its flaws, Darcy's model is still give decent results in general. In the next subsection, we will model the fluid flow through the same porous media by Brinkman's equations for comparison and exhibit the corresponding numerical solutions.

4.6.2 Experiments with Brinkman solver

In this subsection, we investigate the performance of the Brinkman solver in two and three dimension geometries through the following cases: Example 3, Example 4 and Example 5.

Example 3. *(Brinkman - geometries from Figure 4.1) The corresponding geometries are: vuggy media, open foam, fibrous media and periodic geometry. According to Remark 5, we need to assign the permeability coefficients for highly and lowly permeable regions for different experimental setups. The details about experimental setup in this example are given as follows: Inhomogeneous Dirichlet boundary condition:* $u^B = \binom{1}{0}$*, right hand side* $f \equiv 0$*,* $\mu = 10^{-2}$ *and* $\kappa = 1$ *in the red regions (highly permeable) and different* κ *-* 10^4 *,* 10^5 *and* 10^6 *- in the blue regions (low permeable).*

By this setup, we describe a fluid flow that moves from the left boundary to right boundary through different porous media modeled by Brinkman's equations.

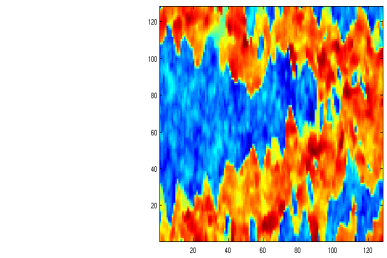

(a) SPE 10 Slice 44

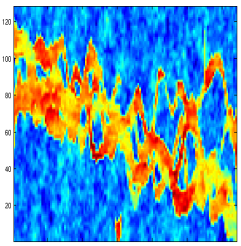

(b) SPE 10 Slice 49

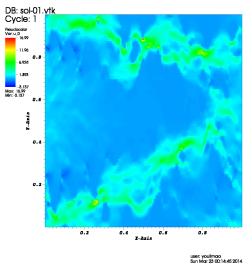

(c) RT_0 - u_1

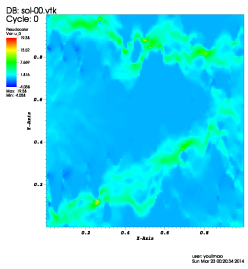

(d) RT_1 - u_1

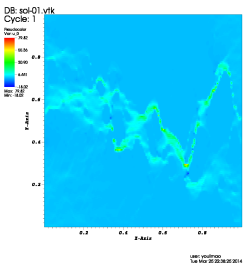

(e) RT_0 - u_1

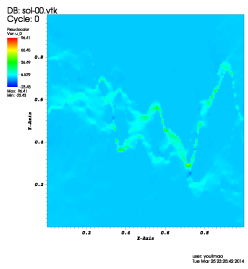

(f) RT_1 - u_1

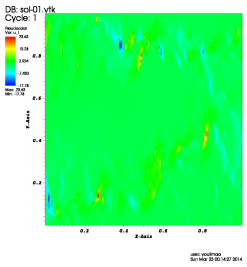

(g) RT_0 - u_2

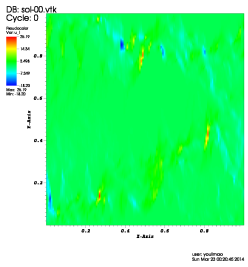

(h) RT_1 - u_2

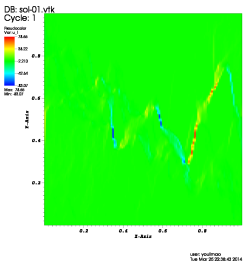

(i) RT_0 - u_2

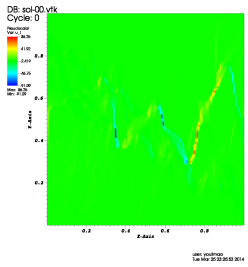

(j) RT_1 - u_2

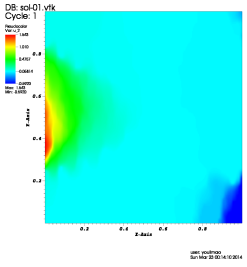

(k) RT_0 - p

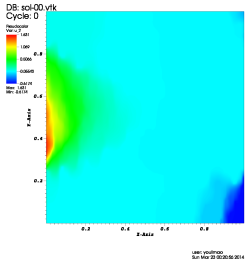

(l) RT_1 - p

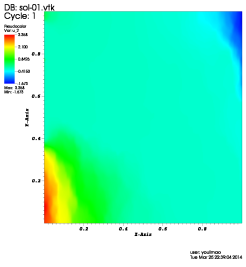

(m) RT_0 - p

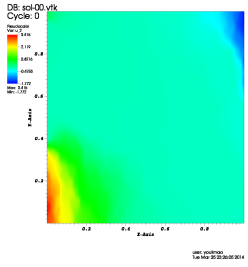

(n) RT_1 - p

Figure 4.7: (Darcy - SPE10 Slice 44 and 49) numerical solution

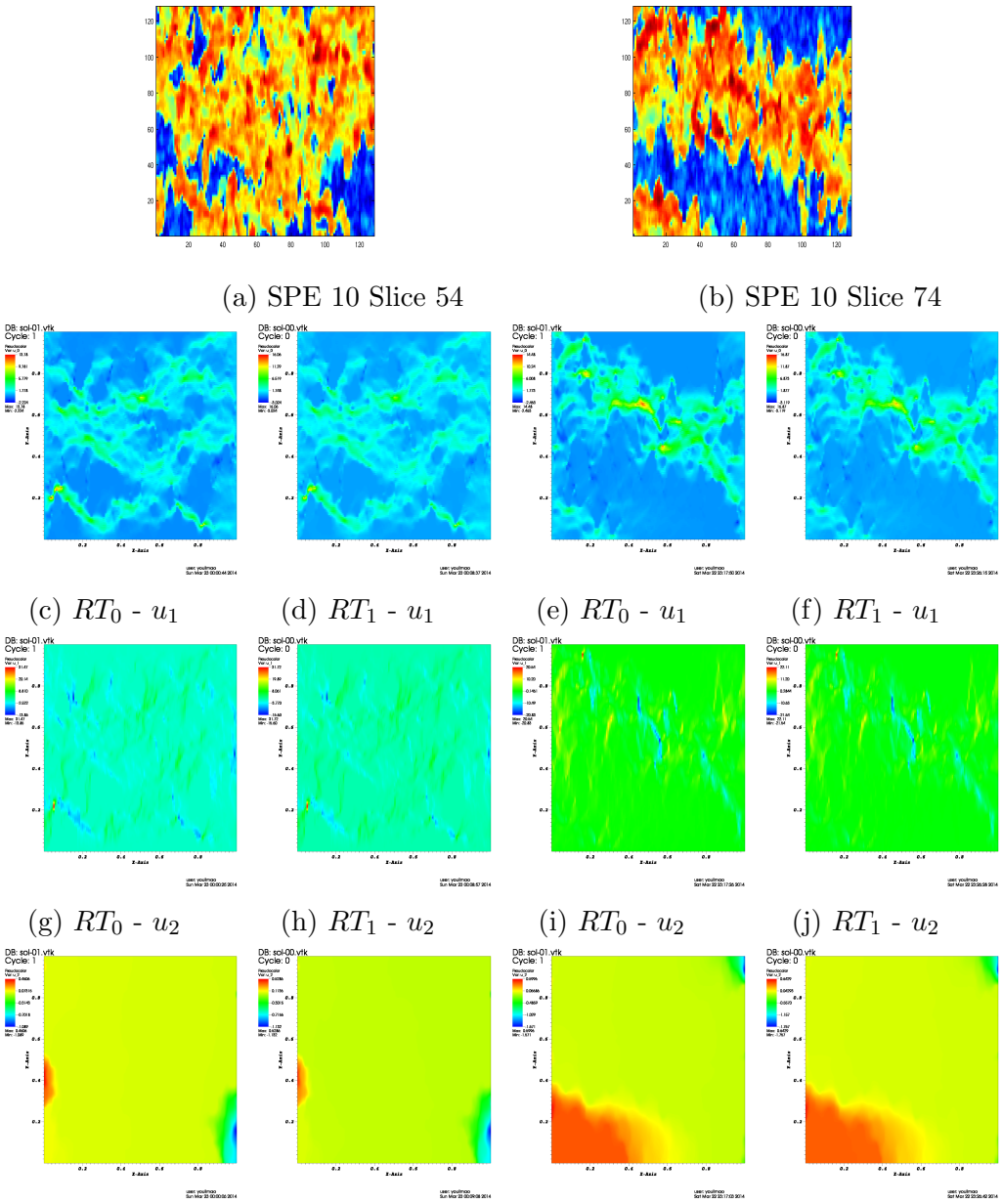

(a) SPE 10 Slice 54 (b) SPE 10 Slice 74

(c) RT_0 - u_1 (d) RT_1 - u_1 (e) RT_0 - u_1 (f) RT_1 - u_1

(g) RT_0 - u_2 (h) RT_1 - u_2 (i) RT_0 - u_2 (j) RT_1 - u_2

(k) RT_0 - p (l) RT_1 - p (m) RT_0 - p (n) RT_1 - p

Figure 4.8: (Darcy - SPE10 Slice 54 and 74) numerical solution

Specifically, we are interesting in the performance of the proposed Brinkman solver on diverse geometries with respect to different permeability contrasts.

	Vuggy medium			Open foam			Fibrous media			Periodic		
Mesh size	10^4	10^5	10^6	10^4	10^5	10^6	10^4	10^5	10^6	10^4	10^5	10^6
1/128	11	17	25	12	22	31	11	21	31	19	20	22
1/256	11	16	24	12	21	30	10	20	30	19	20	22
1/512	10	16	23	11	20	29	10	20	29	18	19	21

Table 4.3: Brinkman solver on different geometries - Permeability contrast on the right columns

In Table 4.3, we observe similar convergence performance as in Darcy's solver for the same geometries. In Figure 4.9 and 4.10, we show the first component of velocity u_1 and pressure component p with respect to different geometries and permeability contrasts.

Example 4. *(Brinkman - Nature reservoir geometry in SPE 10) The corresponding geometries are: slice 44, 49, 54 and 74 of the SPE 10 geometries in Figure 4.2. We assign the permeability field following Example 2.*
The details about experimental setup in this example are given as follows: Inhomogeneous Dirichlet boundary condition: $u^B = \binom{1}{0}$*, right hand side* $f \equiv 0$*, and* $\mu = 10^{-2}$ *(rather small viscosity coefficients are typically chosen in order to make the term* $(\kappa^{-1}(x)u, v)$ *dominant in the discrete system 4.7).*

By this setup, we depict a fluid flow (oil or water) inside the natural reservoirs by Brinkman's equations. Here we are interesting in the performance of the proposed

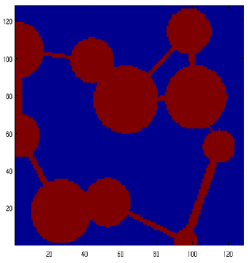

(a) Vuggy medium

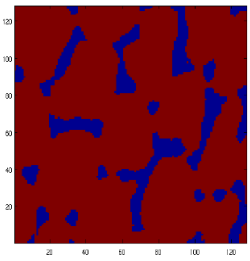

(b) Open foam

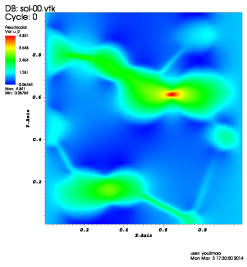

(c) permeability contrast 10^4 - u_1

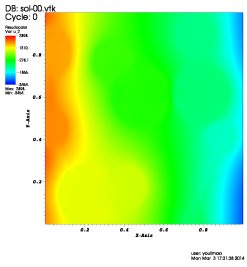

(d) permeability contrast 10^4 - p

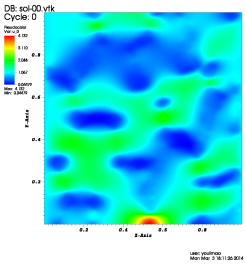

(e) permeability contrast 10^4 - u_1

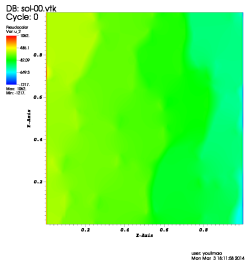

(f) permeability contrast 10^4 - p

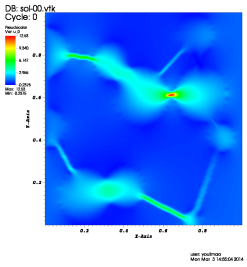

(g) permeability contrast 10^5 - u_1

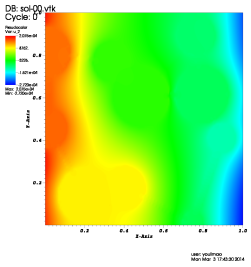

(h) permeability contrast 10^5 - p

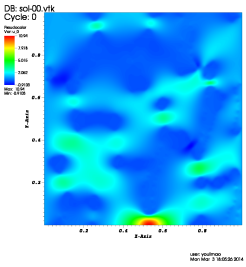

(i) permeability contrast 10^5 - u_1

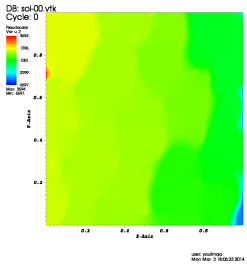

(j) permeability contrast 10^5 - p

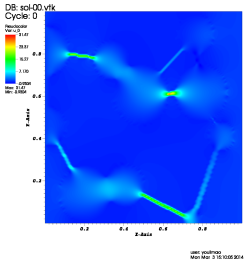

(k) permeability contrast 10^6 - u_1

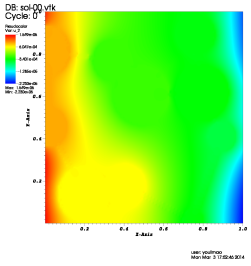

(l) permeability contrast 10^6 - p

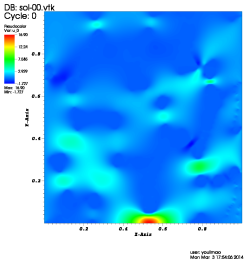

(m) permeability contrast 10^6 - u_1

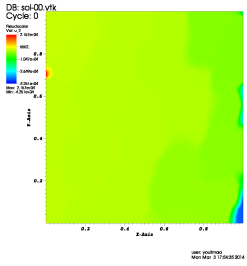

(n) permeability contrast 10^6 - p

Figure 4.9: (Brinkman - Vuggy medium and open foam) numerical solution

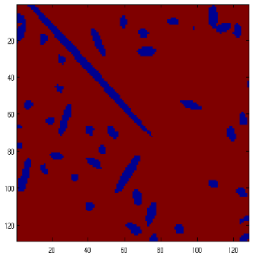

(a) Fibrous medium

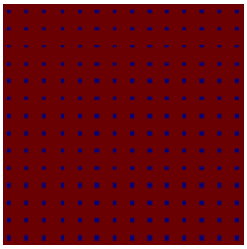

(b) Periodic geometry

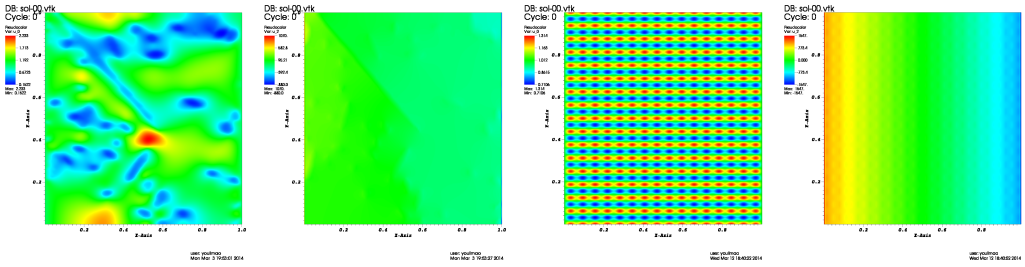

(c) permeability contrast 10^4 - u_1 (d) permeability contrast 10^4 - p (e) permeability contrast 10^4 - u_1 (f) permeability contrast 10^4 - p

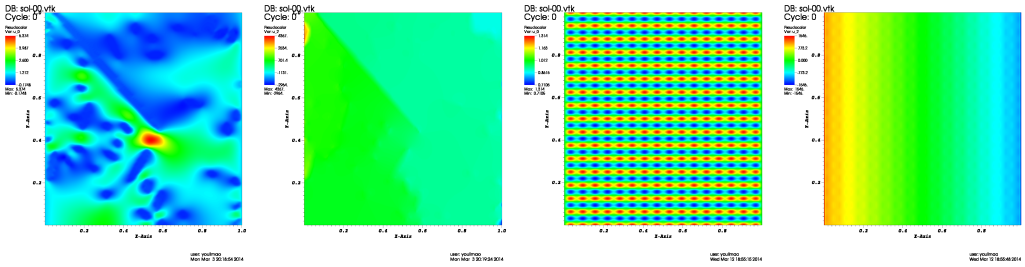

(g) permeability contrast 10^5 - u_1 (h) permeability contrast 10^5 - p (i) permeability contrast 10^5 - u_1 (j) permeability contrast 10^5 - p

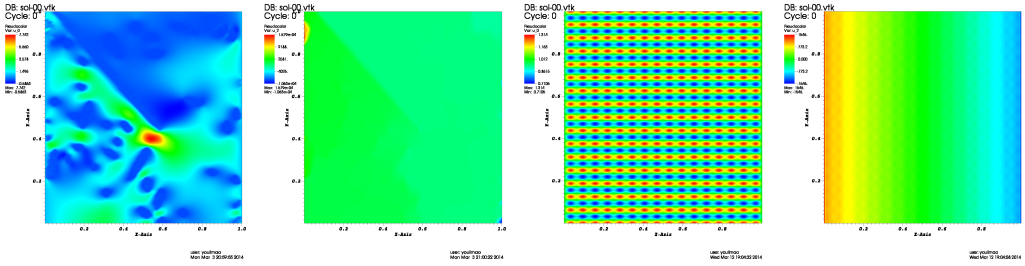

(k) permeability contrast 10^6 - u_1 (l) permeability contrast 10^6 - p (m) permeability contrast 10^6 - u_1 (n) permeability contrast 10^6 - p

Figure 4.10: (Brinkman - Fibrous medium and periodic geometry) numerical solution

Brinkman solver with respect to nature reservoir geometries with different features.

	Slice 44		Slice 49		SPE 54		SPE 74	
Mesh size	RT_0	RT_1	RT_0	RT_1	RT_0	RT_1	RT_0	RT_1
1/128	28	32	29	35	26	28	29	33
1/256	26	29	27	32	24	26	27	31
1/512	24	27	23	29	22	24	25	28

Table 4.4: Brinkman solver on SPE 10 geometries - Different finite orders on the right columns

In Table 4.4, we demo the convergence results for the Brinkman solver on SPE 10 geometries with different finite element orders. For a fixed slice (any column), we perceive optimal convergence rate with respect to mesh refinements(see Remark 8). For a fixed multigrid level, we also observe robust results with respect to different geometries. Additionally, we discern the robustness of our solver with respect to different finite element orders. Besides, the convergence rates in the Table 4.4 also confirm our predictions about the geometric features of the three slices. The corresponding numerical solutions can be found in Figure 4.11 - 4.12.

From the numerical solutions in Figure 4.9 - 4.12, the improvement is rather self-evident in compare to the results of Darcy's model, which indicates the superiority of Brinkman's model.

Finally, we finish our numerical experiments with a 3D simulation on the rescaled SPE10 natural reservoir model.

Example 5. *(Brinkman - 3D simulation on natural reservoir model (see Figure 4.3)) In this example, we exhibit a three dimensional numerical simulation of rescaled*

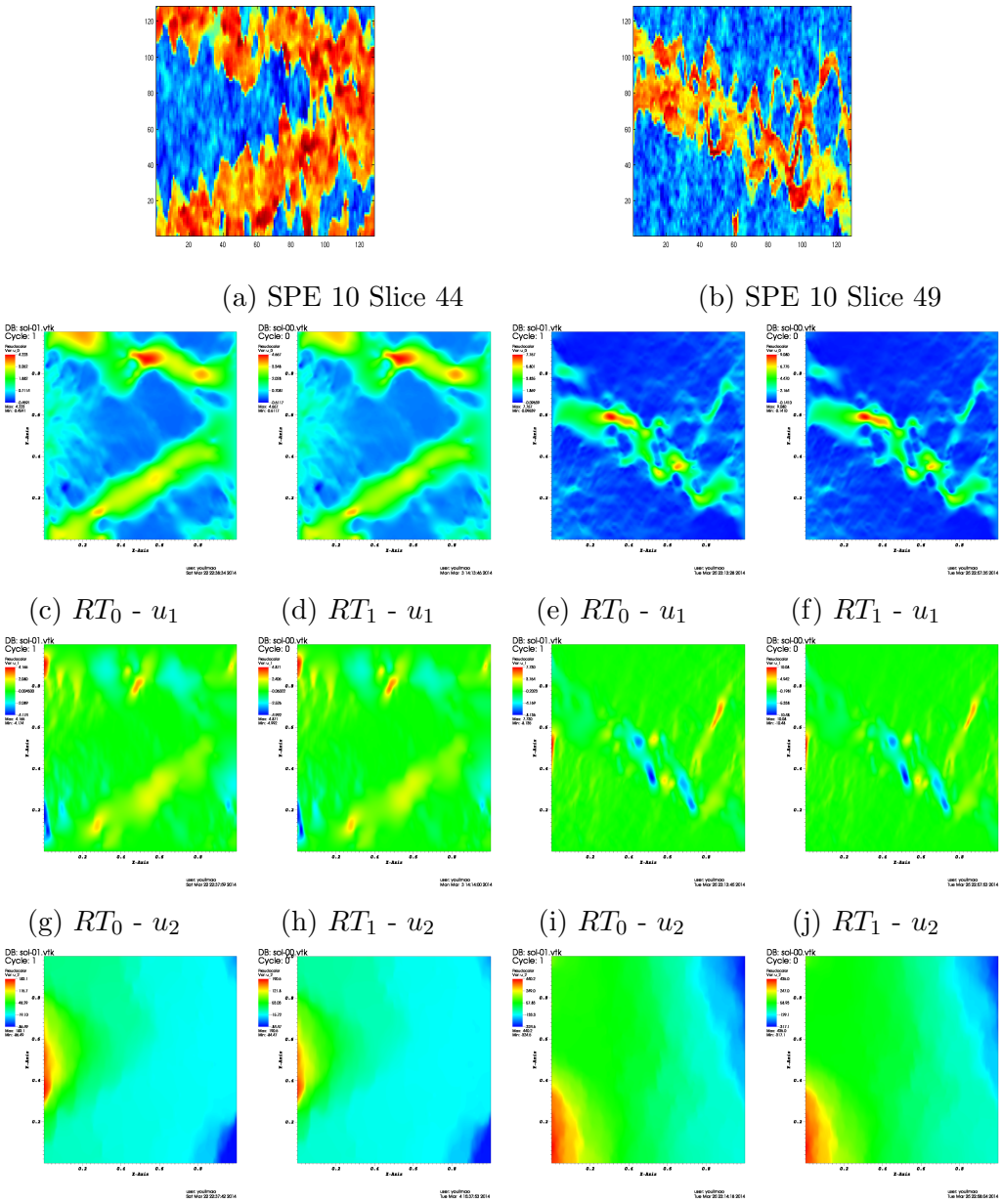

(a) SPE 10 Slice 44 (b) SPE 10 Slice 49

(c) RT_0 - u_1 (d) RT_1 - u_1 (e) RT_0 - u_1 (f) RT_1 - u_1

(g) RT_0 - u_2 (h) RT_1 - u_2 (i) RT_0 - u_2 (j) RT_1 - u_2

(k) RT_0 - p (l) RT_1 - p (m) RT_0 - p (n) RT_1 - p

Figure 4.11: (Brinkman - SPE10 Slice 44 and 49) numerical solution

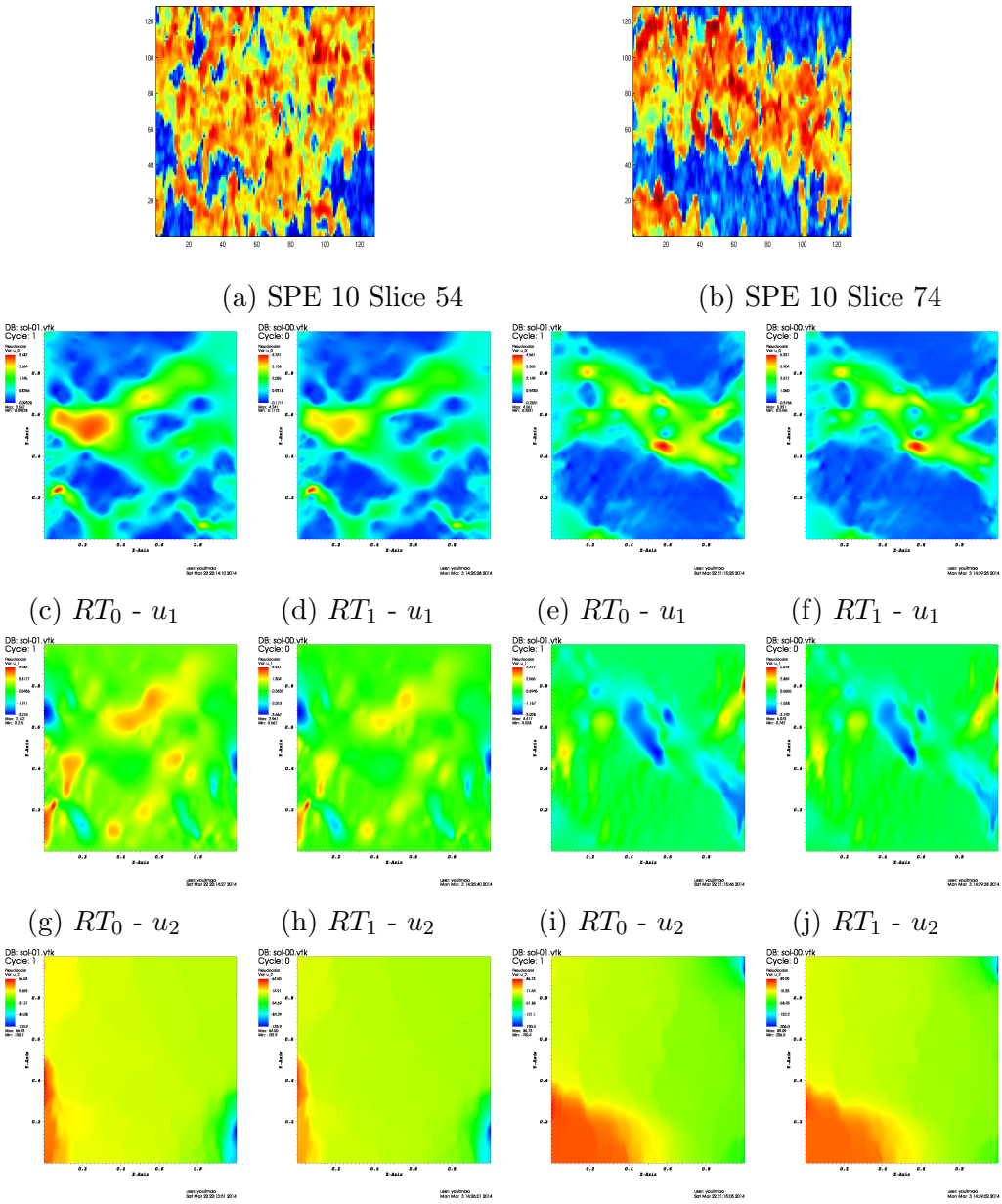

(a) SPE 10 Slice 54 (b) SPE 10 Slice 74

(c) RT_0 - u_1 (d) RT_1 - u_1 (e) RT_0 - u_1 (f) RT_1 - u_1

(g) RT_0 - u_2 (h) RT_1 - u_2 (i) RT_0 - u_2 (j) RT_1 - u_2

(k) RT_0 - p (l) RT_1 - p (m) RT_0 - p (n) RT_1 - p

Figure 4.12: (Brinkman - SPE10 Slice 54 and 74) numerical solution

natural reservoir geometry in Figure 4.3. The permeability data are assigned in the similar fashion as in Example 2 and Example 4. The details about experimental setup in this example are given as follows: Inhomogeneous Dirichlet boundary condition and homogeneous right hand side:

$$u^B = \begin{pmatrix} 1 \\ 0 \\ 0 \end{pmatrix}_{BC1} \quad \& \quad \begin{pmatrix} 0 \\ 1 \\ 0 \end{pmatrix}_{BC2}, \text{ and } f = \begin{pmatrix} 0 \\ 0 \\ 0 \end{pmatrix} \tag{4.47}$$

and viscosity coefficient $\mu = 10^{-2}$*).*

By this setup, we basically extend Example 4 into three dimensional case. As we indicated in Remark 6, the top half the reservoir data has clearly visible channels but the bottom half does not. Thus, it is not necessary to model flow through $X-Y$ along $Z-Axis$. Therefore, by the first and second boundary conditions we model flow through $Y-Z$ plane and $X-Z$ plane along $X-Axis$ and $Y-Axis$, respectively.

	Residual 10^{-6}		Residual 10^{-7}		Residual 10^{-8}		Residual 10^{-9}	
Mesh size	$BC1$	$BC2$	$BC1$	$BC2$	$BC1$	$BC2$	$BC1$	$BC2$
1/64	40	41	47	47	55	56	65	66
1/128	31	31	39	39	46	46	57	57

Table 4.5: Brinkman solver on 3D SPE 10 model - Different boundary conditions on the right columns

Remark 9. *(on 3D results in Table 4.5) In Table 4.5, we show the convergence results with respect to reduction residual in our solver. For a fixed column, we observe*

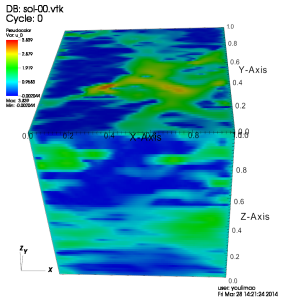

(a) Solver reduction residual 10^{-6}

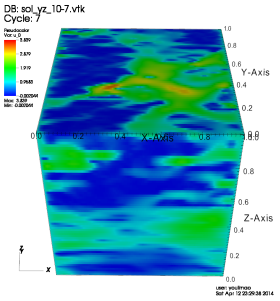

(b) Solver reduction residual 10^{-7}

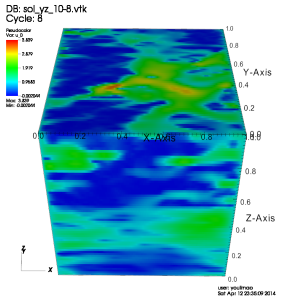

(c) Solver reduction residual 10^{-8}

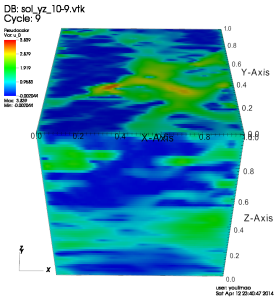

(d) Solver reduction residual 10^{-9}

Figure 4.13: (Brinkman with RT_0) numerical solution with respect to different reduction residuals in the solver

similar optimal convergence rate as in two dimensional cases. After two refinements, the number of degree freedom is about 70 million and our machine runs out of memory, thus no convergence results are available thereafter. Besides, the results with RT_1 and DGQ_1 are either not available due to the same memory issue of our current machine (the number of degree freedom reaches 10 million on the initial grid).

In Figure 4.13, we present the first component of velocity with respect to different reduction residuals for flow through $X - Z$ plane. Despite of the small increase of convergence steps, we observe the almost identical numerical solution as shown in Figure 4.13.

In Figure 4.14- 4.17, we show numerical solutions with respect to different boundary conditions and velocity components.

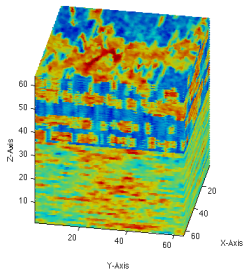

(a) Flow through $Y-Z$ plane (Front View)

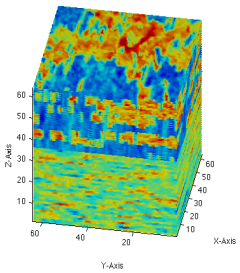

(b) Flow through $Y-Z$ plane (Back View)

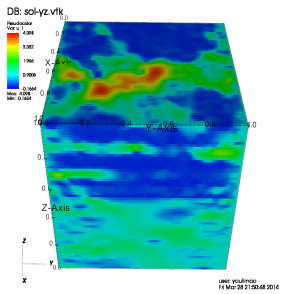

(c) First component of velocity

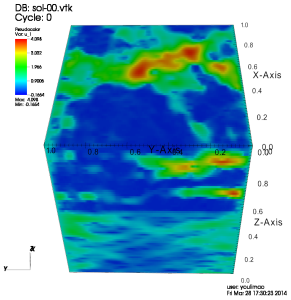

(d) First component of velocity

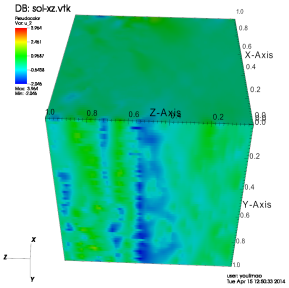

(e) Third component of velocity

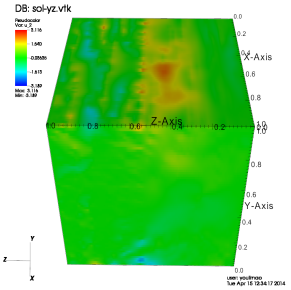

(f) Third component of velocity

Figure 4.14: (Brinkman - 3D SPE 10 with flow through $Y-Z$ plane) numerical solution

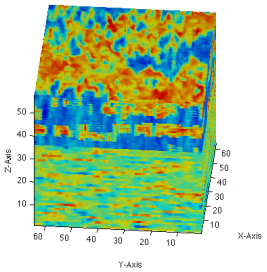

(a) Flow through $Y - Z$ plane (Box View) - Slice 58

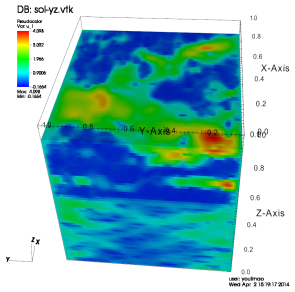

(b) First component of velocity - Slice 58

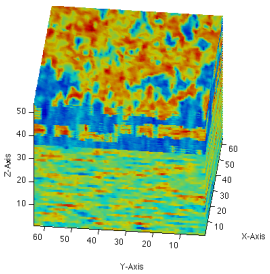

(c) Flow through $Y - Z$ plane (Box View) - Slice 54

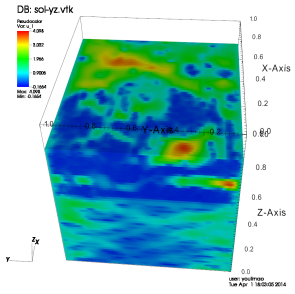

(d) First component of velocity - Slice 54

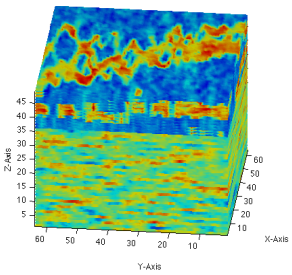

(e) Flow through $Y - Z$ plane (Box View) - Slice 49

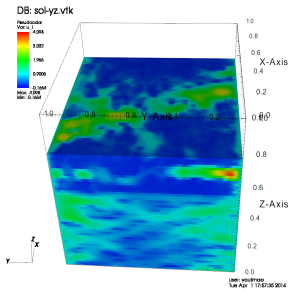

(f) First component of velocity - Slice 49

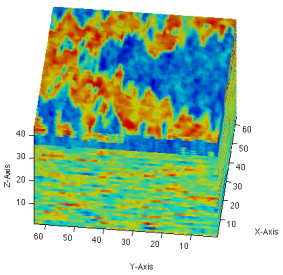

(g) Flow through $Y - Z$ plane (Box View) - Slice 44

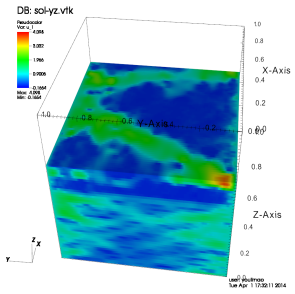

(h) First component of velocity - Slice 44

Figure 4.15: (Brinkman - 3D SPE 10 with flow through $Y - Z$ plane) Slice views of numerical solution

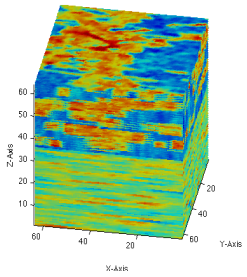

(a) Flow through $X-Z$ plane (Front View)

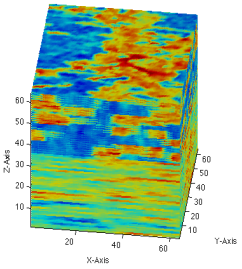

(b) First component of velocity

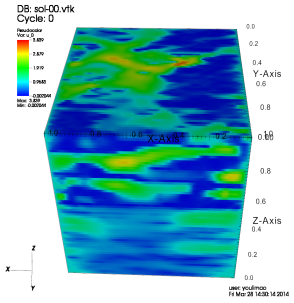

(c) Flow through $X-Z$ plane (Back View)

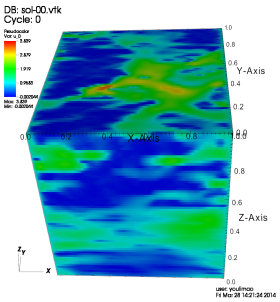

(d) First component of velocity

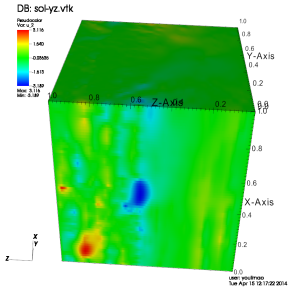

(e) Third component of velocity

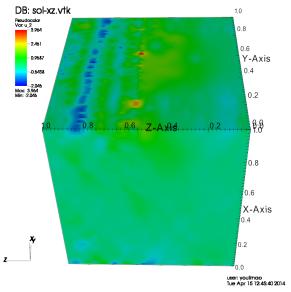

(f) Third component of velocity

Figure 4.16: (Brinkman - 3D SPE 10 with flow through $X-Z$ plane) numerical solution

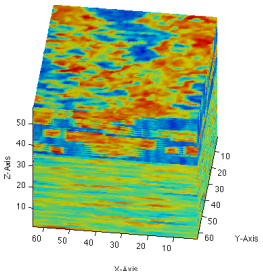

(a) Flow through $Y - Z$ plane (Box View) - Slice 58

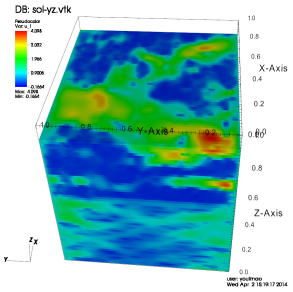

(b) First component of velocity - Slice 58

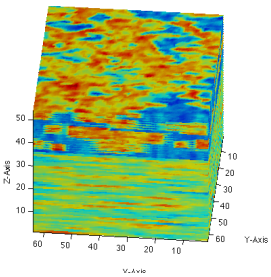

(c) Flow through $X - Z$ plane (Box View) - Slice 54

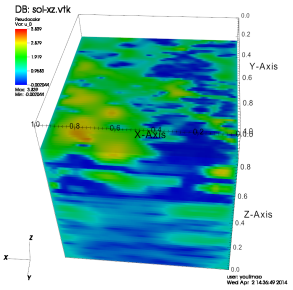

(d) First component of velocity - Slice 54

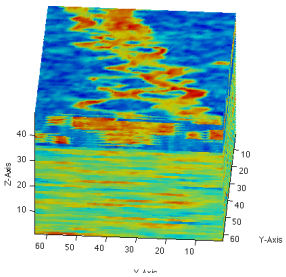

(e) Flow through $X - Z$ plane (Box View) - Slice 49

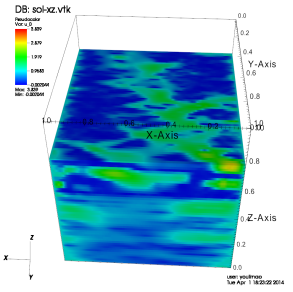

(f) First component of velocity - Slice 49

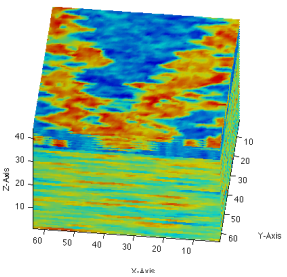

(g) Flow through $X - Z$ plane (Box View) - Slice 44

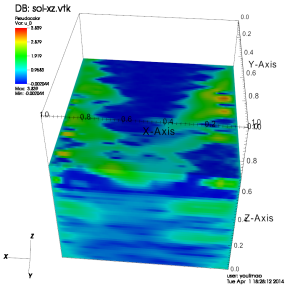

(h) First component of velocity - Slice 44

Figure 4.17: (Brinkman - 3D SPE 10 with flow through $X - Z$ plane) Slice views of numerical solution

4.7 Conclusion

In this section, we introduce the H^{div}-conforming discontinuous Galerkin discretization for the Brinkman's equations, and present a geometric multigrid method with on Arnold-Falk-Winther type smoother for the system. We present the convergence analysis with constant permeability case and show uniform contraction independent of the mesh size. In addition, we experimentally verify the robustness and efficiency of our method with respect to different partial differential equation models on complex geometries (two and three dimensional cases). Therefore, it makes our method a powerful solver for flow problems in highly heterogeneous and highly porous media.

5. SUMMARY

In this dissertation, we have studied and implemented a geometric multigrid method for flow problems such as Stokes flow, Darcy flow, the coupling of Stokes and Darcy flow and Brinkman equations. This multigrid method is based on H^{div}-conforming finite element methods under which the discrete velocity field is globally exactly divergence free for incompressible flows. There are two key ingredients of the proposed preconditioner: first, the Arnold-Falk-Winther type smoothers can capture a meaningful basis on local divergence free subspace associated with each overlapping patch; additionally, the grid operator does not increase the divergence from the coarse divergence free subspace to the fine one due to the fact that the divergence free spaces are nested.

In Section 2, we first introduce the multigrid preconditioning method with H^{div}-conforming discontinuous Galerkin methods for the Stokes problem, and then we prove the convergence analysis for two types of domain decomposition Schwarz smoothers with variable V-cycle method. Within these proofs, we choose the penalty parameter depend on the polynomial degree and the mesh size of the finest level $O(\frac{k^2}{h_J})$ in the DG method. The corresponding numerical results confirm our analysis work which also show strong robustness and efficiency. For the standard V-cycle method with penalty parameter of order $O(\frac{k^2}{h_J})$, we experimentally exhibit the robust and efficient results despite of the lack of theoretical proof. For the penalty parameter of order $O(\frac{k^2}{h_j})$ with both variable and standard V-cycle methods, plenty of numerical evidence shows the same computational performance as that of order $O(\frac{k^2}{h_J})$ albeit without analysis work. Besides, we extend our numerical experiments to non-simply connected geometries where the Hodge decompositions are rather complicated.

In Section 3, we migrate to the coupling of Stokes and Darcy flow based on Stokes results in the previous section. We apply the similar H^{div}-conforming DG method for the coupled system and the same multigrid preconditioning method. The analysis work for this coupled model is still under development due to the presence of interface terms. Despite the fact that we can not prove the convergence, the numerical results show strong robustness and efficiency of the proposed multigrid solver.

In Section 4, we present the models for flows in highly heterogeneous and highly porous media with corresponding H^{div}-conforming finite element discretizations. Then we introduce the multigrid preconditioning method for the corresponding discrete system. The convergence analysis of the proposed multigrid method for Brinkman problem has been provided with constant permeability coefficient. For the varying coefficient cases, we apply a relative simple but effective coefficient upscaling and downscaling schemes on the coarse and fine grids. Finally, we introduce two sets of industry related geometries (*e.g.*, industrial filter models and natural reservoir model), and show the robustness, efficiency and unification of our algorithm through plenty of numerical experiments in two and three dimension.

Up to now, it is still an open problem for the analysis work of fully robust (with respect to coefficient variation) multigrid preconditioning method. Future developments of interest include coefficient upscaling techniques, parallel computation and analysis work with respect to coefficient variation.

REFERENCES

[1] Burak Aksoylu, Ivan Graham, Hector Klie, and Robert Scheichl. Towards a rigorously justified algebraic preconditioner for high-contrast diffusion problems. *Computing and Visualization in Science*, 11(4-6):319–331, 2008.

[2] Grégoire Allaire. Homogenization of the Navier-Stokes equations in open sets perforated with tiny holes i. abstract framework, a volume distribution of holes. *Archive for Rational Mechanics and Analysis*, 113(3):209–259, 1991.

[3] Philippe Angot. Analysis of singular perturbations on the Brinkman problem for fictitious domain models of viscous flows. *Mathematical Methods in The Applied Sciences*, 22(16):1395–1412, 1999.

[4] Philippe Angot, Charles-Henri Bruneau, and Pierre Fabrie. A penalization method to take into account obstacles in incompressible viscous flows. *Numerische Mathematik*, 81(4):497–520, 1999.

[5] Todd Arbogast. Implementation of a locally conservative numerical subgrid upscaling scheme for two-phase Darcy flow. *Computational Geosciences*, 6(3-4):453–481, 2002.

[6] Todd Arbogast. Analysis of a two-scale, locally conservative subgrid upscaling for elliptic problems. *SIAM Journal on Numerical Analysis*, 42(2):576–598, 2005.

[7] Todd Arbogast and Heather Lehr. Homogenization of a Darcy–Stokes system modeling vuggy porous media. *Computational Geosciences*, 10(3):291–302, 2006.

[8] Todd Arbogast, Gergina Pencheva, Mary F Wheeler, and Ivan Yotov. A multiscale mortar mixed finite element method. *Multiscale Modeling & Simulation*, 6(1):319–346, 2007.

[9] Todd Arbogast and Hailong Xiao. A multiscale mortar mixed space based on homogenization for heterogeneous elliptic problems. *SIAM Journal on Numerical Analysis*, 51(1):377–399, 2013.

[10] D. Arnold. An interior penalty finite element method with discontinuous elements. *SIAM Journal on Numerical Analysis*, 19(4):742–760, 1982.

[11] Douglas Arnold, Richard Falk, and Ragnar Winther. Preconditioning in H(div) and applications. *Math. Comp*, 66(219):957–984, 1997.

[12] Douglas Arnold, Richard Falk, and Ragnar Winther. Multigrid in H(div) and H(curl). *Numerische Mathematik*, 85(2):197–217, 2000.

[13] Douglas N. Arnold, Richard S. Falk, and Ragnar Winther. Finite element exterior calculus: from Hodge theory to numerical stability. *Bull. Amer. Math. Soc. (N.S.)*, 47:281–354, 2010.

[14] Blanca Ayuso de Dios, Franco Brezzi, L.Donatella Marini, Jinchao Xu, and Ludmil Zikatanov. A simple preconditioner for a discontinuous Galerkin method for the Stokes problem. *Journal of Scientific Computing*, 58(3):517–547, 2014.

[15] Wolfgang Bangerth, Timo Heister, Guido Kanschat, et al. `deal.II` *Differential Equations Analysis Library, Technical Reference*, 1999. `http://www.dealii.org`.

[16] Gordon Beavers and Daniel Joseph. Boundary conditions at a naturally permeable wall. *Journal of Fluid Mechanics*, 30(01):197–207, 1967.

[17] Giuseppe Bonfigli and Patrick Jenny. An efficient multi-scale Poisson solver for the incompressible Navier–Stokes equations with immersed boundaries. *Journal of Computational Physics*, 228(12):4568 – 4587, 2009.

[18] D. Braess and W. Hackbusch. A new convergence proof for the Multigrid method including the V-cycle. *SIAM Journal on Numerical Analysis*, 20(5):967–975, 1983.

[19] James Bramble. *Multigrid methods*. John Wiley & Sons Inc, New York, 1993.

[20] Franco Brezzi. On the existence, uniqueness and approximation of saddle-point problems arising from Lagrangian multipliers. *ESAIM: Mathematical Modelling and Numerical Analysis-Modélisation Mathématique et Analyse Numérique*, 8(R2):129–151, 1974.

[21] Franco Brezzi and Michel Fortin. *Mixed and Hybrid Finite Element Methods*. Springer-Verlag, New York, 1991.

[22] William Briggs, Steve McCormick, et al. *A multigrid tutorial*, volume 72. SIAM, Philadelphis, 2000.

[23] HC Brinkman. A calculation of the viscous force exerted by a flowing fluid on a dense swarm of particles. *Applied Scientific Research*, 1(1):27–34, 1949.

[24] Erik Burman and Peter Hansbo. Stabilized Crouzeix-Raviart element for the Darcy-Stokes problem. *Numerical Methods for Partial Differential Equations*, 21(5):986–997, 2005.

[25] Erik Burman and Peter Hansbo. A unified stabilized method for Stokes' and Darcy's equations. *Journal of Computational and Applied Mathematics*, 198(1):35–51, 2007.

[26] Mingchao Cai and Mo Mu. A multilevel decoupled method for a mixed Stokes/Darcy model. *Journal of Computational and Applied Mathematics*, 236(9):2452–2465, 2012.

[27] Zhiqiang Cai, Charles I Goldstein, and Joseph E Pasciak. Multilevel iteration for mixed finite element systems with penalty. *SIAM Journal on Scientific Computing*, 14(5):1072–1088, 1993.

[28] Michael Christie and Martin Blunt. Tenth SPE comparative solution project: A comparison of upscaling techniques. *SPE Reservoir Evaluation & Engineering*, 4(04):308–317, 2001.

[29] Bernardo Cockburn, Guido Kanschat, and Dominik Schötzau. A locally conservative LDG method for the incompressible Navier-Stokes equations. *Mathematics of Computation*, 74(251):1067–1095, 2005.

[30] Bernardo Cockburn, Guido Kanschat, and Dominik Schötzau. A note on discontinuous Galerkin divergence-free solutions of the Navier–Stokes equations. *Journal of Scientific Computing*, 31(1-2):61–73, 2007.

[31] Bernardo Cockburn, Guido Kanschat, Dominik Schötzau, and Christoph Schwab. Local discontinuous Galerkin methods for the Stokes system. *SIAM Journal on Numerical Analysis*, 40(1):319–343, 2002.

[32] Carlo D'Angelo and Paolo Zunino. A finite element method based on weighted interior penalties for heterogeneous incompressible flows. *SIAM Journal on Numerical Analysis*, 47(5):3990–4020, 2009.

[33] Yalchin Efendiev, Juan Galvis, Seul Ki Kang, and Raytcho Lazarov. Robust Multiscale Iterative Solvers for Nonlinear Flows in Highly Heterogeneous Media. *Numerical Mathematics: Theory, Methods & Applications*, 5(3), 2012.

[34] Yalchin Efendiev, Juan Galvis, Raytcho Lazarov, Svetozar Margenov, and Jun Ren. Robust two-level domain decomposition preconditioners for high-contrast anisotropic flows in multiscale media. *Computational Methods in Applied Mathematics*, 12(4):415–436, 2012.

[35] Yalchin Efendiev, Juan Galvis, Raytcho Lazarov, and Jeorg Willems. Numerical upscaling and preconditioning of flows in highly heterogeneous porous media. *Advanced Computational Engineering, Report No 09*, pages 55–59, 2012.

[36] Yalchin Efendiev, Juan Galvis, and Panayot Vassilevski. Spectral element agglomerate algebraic multigrid methods for elliptic problems with high-contrast coefficients. In *Domain Decomposition Methods in Science and Engineering XIX*, pages 407–414. Springer, 2011.

[37] Yalchin Efendiev, Juan Galvis, and Panayot Vassilevski. Multiscale spectral AMGe solvers for high-contrast flow problems. *ISC-Preprint 2012*, 2, 2012.

[38] Yalchin Efendiev and Thomas Hou. *Multiscale finite element methods: theory and applications*, volume 4. Springer, New York, 2009.

[39] Yalchin Efendiev, Thomas Hou, and Xiao-Hui Wu. Convergence of a nonconforming multiscale finite element method. *SIAM Journal on Numerical Analysis*, 37(3):888–910, 2000.

[40] Howard Elman, David Silvester, and Andrew Wathen. Performance and analysis of saddle point preconditioners for the discrete steady-state Navier-Stokes equations. *Numerische Mathematik*, 90(4):665–688, 2002.

[41] Richard Falk and Michael Neilan. Stokes complexes and the construction of stable finite elements with pointwise mass conservation. *SIAM Journal on Numerical Analysis*, 51(2):1308–1326, 2013.

[42] Xiaobing Feng and Ohannes Karakashian. Two-level additive Schwarz methods for a discontinuous Galerkin approximation of second order elliptic problems. *SIAM Journal on Numerical Analysis*, 39(4):1343–1365, 2001.

[43] Ivan Graham, Patrick Lechner, and Robert Scheichl. Domain decomposition for multiscale PDEs. *Numerische Mathematik*, 106(4):589–626, 2007.

[44] Johnny Guzmán and Michael Neilan. Conforming and divergence-free Stokes elements on general triangular meshes. *Mathematics of Computation*, 83(285):15–36, 2014.

[45] Hadi Hajibeygi, Giuseppe Bonfigli, Marc Andre Hesse, and Patrick Jenny. Iterative multiscale finite-volume method. *Journal of Computational Physics*, 227(19):8604–8621, 2008.

[46] Antti Hannukainen, Mika Juntunen, and Rolf Stenberg. Computations with finite element methods for the Brinkman problem. *Computational Geosciences*, 15(1):155–166, 2011.

[47] Peter Hansbo and Mika Juntunen. Weakly imposed Dirichlet boundary conditions for the Brinkman model of porous media flow. *Applied Numerical Mathematics*, 59(6):1274–1289, 2009.

[48] Peter Hansbo and Mats Larson. Discontinuous Galerkin methods for incompressible and nearly incompressible elasticity by Nitsche's method. *Computer Methods in Applied Mechanics and Engineering*, 191(17):1895–1908, 2002.

[49] Pascal Havé, Roland Masson, Frédéric Nataf, Mikolaj Szydlarski, Hua Xiang, and Tao Zhao. Algebraic domain decomposition methods for highly heterogeneous problems. *SIAM Journal on Scientific Computing*, 35(3):C284–C302, 2013.

[50] Ralf Hiptmair. Multigrid method for Maxwell's equations. *SIAM Journal on Numerical Analysis*, 36(1):204–225, 1998.

[51] Ralf Hiptmair and Jinchao Xu. Preface: Special issue on adaptive and multilevel methods in computational electromagnetics. *Journal of Computational Mathematics*, 27:561–562, 2009.

[52] Oleg Iliev, Zahra Lakdawala, and Vadimas Starikovicius. On a numerical subgrid upscaling algorithm for Stokes–Brinkman equations. *Computers & Mathematics with Applications*, 65(3):435–448, 2013.

[53] Oleg Iliev, Raytcho Lazarov, and Joerg Willems. Discontinuous Galerkin subgrid finite element method for heterogeneous Brinkman's equations. In *Large-Scale Scientific Computing*, pages 14–25. Springer, 2010.

[54] Oleg Iliev, Raytcho Lazarov, and Joerg Willems. Fast numerical upscaling of heat equation for fibrous materials. *Computing and Visualization in Science*, 13(6):275–285, 2010.

[55] Oleg Iliev, Raytcho Lazarov, and Joerg Willems. Variational multiscale finite element method for flows in highly porous media. *Multiscale Modeling & Simulation*, 9(4):1350–1372, 2011.

[56] Bärbel Janssen and Guido Kanschat. Adaptive multilevel methods with local smoothing for H^1 and H^{curl}-conforming high order finite element methods. *SIAM Journal on Scientific Computing*, 33(4):2095–2114, 2011.

[57] Patrick Jenny and Ivan Lunati. Multi-scale finite-volume method for elliptic problems with heterogeneous coefficients and source terms. *PAMM*, 6(1):485–486, 2006.

[58] Guido Kanschat. Multilevel methods for discontinuous Galerkin FEM on locally refined meshes. *Computers & Structures*, 82(28):2437–2445, 2004.

[59] Guido Kanschat. Block preconditioners for LDG discretizations of linear incompressible flow problems. *Journal of Scientific Computing*, 22(1-3):371–384, 2005.

[60] Guido Kanschat. Divergence-free discontinuous Galerkin schemes for the Stokes equations and the MAC scheme. *International Journal for Numerical Methods in Fluids*, 56(7):941–950, 2008.

[61] Guido Kanschat and Youli Mao. Multigrid methods for H(div)-conforming discontinuous Galerkin for the Stokes. *Journal of Numerical Mathematics*, accepted for publication, 2013.

[62] Guido Kanschat and Youli Mao. Multiplicative overlapping Schwarz smoothers for H(div)-conforming discontinuous Galerkin for the Stokes problem. *Lecture Notes in Computational Science and Engineering*, submitted, 2014.

[63] Guido Kanschat and Beatrice Rivière. A strongly conservative finite element method for the coupling of Stokes and Darcy flow. *Journal of Computational Physics*, 229(17):5933–5943, 2010.

[64] Guido Kanschat and Dominik Schötzau. Energy norm a posteriori error estimation for divergence-free discontinuous Galerkin approximations of the Navier–Stokes equations. *International Journal for Numerical Methods in Fluids*, 57(9):1093–1113, 2008.

[65] Guido Kanschat and Natasha Sharma. Divergence-conforming discontinuous Galerkin methods and C^0 interior penalty methods. *SIAM Journal on Numerical Analysis, submitted*, 2013.

[66] David Kay, Daniel Loghin, and Andrew Wathen. A Preconditioner for the Steady-State Navier–Stokes Equations. *SIAM Journal on Scientific Computing*, 24(1):237–256, 2002.

[67] Tzanio Kolev and Panayot Vassilevski. Parallel auxiliary space AMG solver for H(div) problems. *SIAM Journal on Scientific Computing*, 34(6):A3079–A3098, 2012.

[68] Juho Könnö and Rolf Stenberg. H(div)-conforming finite elements for the Brinkman problem. *Mathematical Models and Methods in Applied Sciences*, 21(11):2227–2248, 2011.

[69] William Layton, Friedhelm Schieweck, and Ivan Yotov. Coupling fluid flow with porous media flow. *SIAM Journal on Numerical Analysis*, 40(6):2195–2218, 2002.

[70] Louis-Philippe Lefebvre, John Banhart, and David Dunand. Porous metals and metallic foams: current status and recent developments. *Advanced Engineering Materials*, 10(9):775–787, 2008.

[71] Kent Andre Mardal, Xue-Cheng Tai, and Ragnar Winther. A robust finite element method for Darcy–Stokes flow. *SIAM Journal on Numerical Analysis*, 40(5):1605–1631, 2002.

[72] Lin Mu, Junping Wang, and Xiu Ye. A stable numerical algorithm for the Brinkman equations by weak Galerkin finite element methods. *arXiv preprint*, 2013.

[73] Mo Mu and Jinchao Xu. A two-grid method of a mixed Stokes-Darcy model for coupling fluid flow with porous media flow. *SIAM Journal on Numerical Analysis*, 45(5):1801–1813, 2007.

[74] Malcolm F Murphy, Gene H Golub, and Andrew J Wathen. A note on preconditioning for indefinite linear systems. *SIAM Journal on Scientific Computing*, 21(6):1969–1972, 2000.

[75] Joachim Nitsche. Über ein variationsprinzip zur Lösung von Dirichlet-Problemen bei Verwendung von Teilräumen, die keinen Randbedingungen unterworfen sind. In *Abhandlungen aus dem mathematischen Seminar der Universität Hamburg*, volume 36, pages 9–15. Springer, 1971.

[76] J Alberto Ochoa-Tapia and Stephen Whitaker. Momentum transfer at the boundary between a porous medium and a homogeneous fluid—I. Theoretical development. *International Journal of Heat and Mass Transfer*, 38(14):2635–2646, 1995.

[77] Clemens Pechstein and Robert Scheichl. Scaling up through domain decomposition. *Applicable Analysis*, 88(10-11):1589–1608, 2009.

[78] Clemens Pechstein and Robert Scheichl. Analysis of FETI methods for multiscale PDEs. Part II: interface variation. *Numerische Mathematik*, 118(3):485–529, 2011.

[79] Peter Popov. Preconditioning of linear systems arising in finite element discretizations of the Brinkman equation. In *Proceedings of the 8th International Conference on Large-Scale Scientific Computing*, LSSC'11, pages 381–389. Springer-Verlag, 2012.

[80] Peter Popov, Linfeng Bi, Yalchin Efendiev, Richard Edward Ewing, Guan Qin, Jianglong Li, Yulin Ren, et al. Multi-physics and multi-scale methods for modeling fluid flow through naturally-fractured vuggy carbonate reservoirs. In *SPE Middle East Oil and Gas Show and Conference*. Society of Petroleum Engineers, 2007.

[81] Pierre-Arnaud Raviart and Jean-Marie Thomas. A mixed finite element method for 2-nd order elliptic problems. In *Mathematical Aspects of Finite Element Methods*, pages 292–315. Springer, 1977.

[82] Joachim Schöberl. Multigrid methods for a parameter dependent problem in primal variables. *Numerische Mathematik*, 84(1):97–119, 1999.

[83] Joachim Schöberl. *Robust multigrid methods for parameter dependent problems.* PhD thesis, Johannes Kepler Universität Linz, Linz, 1999.

[84] Dominik Schötzau, Christoph Schwab, and Andrea Toselli. Mixed hp-DGFEM for incompressible flows. *SIAM Journal on Numerical Analysis*, 40(6):2171–2194, 2002.

[85] Ridgway Scott and Michael Vogelius. Norm estimates for a maximal right inverse of the divergence operator in spaces of piecewise polynomials. *Modélisation Mathématique et Analyse Numérique*, 19(1):111–143, 1985.

[86] Ulrich Trottenberg, Cornelius W Oosterlee, and Anton Schuller. *Multigrid*. Academic press, Waltham, 2000.

[87] Stefan Turek. An efficient solution technique for the radiative transfer equation. *Impact of Computing in Science and Engineering*, 5(3):201–214, 1993.

[88] Martyn Twigg and James Richardson. Fundamentals and applications of structured ceramic foam catalysts. *Industrial & Engineering Chemistry Research*, 46(12):4166–4177, 2007.

[89] Pratap Vanka. Block-implicit multigrid solution of Navier-Stokes equations in primitive variables. *Journal of Computational Physics*, 65(1):138–158, 1986.

[90] Panayot Vassilevski and Umberto Villa. A block-diagonal algebraic multigrid preconditioner for the Brinkman problem. *SIAM Journal on Scientific Computing*, 35(5):S3–S17, 2013.

[91] Panayot Vassilevski and Umberto Villa. A mixed formulation for the brinkman problem. *SIAM Journal on Numerical Analysis*, 52(1):258–281, 2014.

[92] Umberto Villa. *Scalable efficient methods for incompressible fluid-dynamics in engineering problems*. PhD thesis, Emory University, Atlanta, 2012.

[93] Michael Vogelius. A right-inverse for the divergence operator in spaces of piecewise polynomials. *Numerische Mathematik*, 41(1):19–37, 1983.

[94] Junping Wang and Xiu Ye. New finite element methods in computational fluid dynamics by H(div) elements. *SIAM Journal on Numerical Analysis*, 45(3):1269–1286, 2007.

[95] Joerg Willems. *Numerial upscalling for multiscale flow problems.* PhD thesis, Technische Universitat Kaiserslautern, Kaiserslautern, 2009.

[96] Hilmar Wobker and Stefan Turek. Numerical studies of Vanka-type smoothers in computational solid mechanics. *Advances in Applied Mathematics and Mechanics*, 1(1):29–55, 2009.

[97] Xiaoping Xie, Jinchao Xu, and Guangri Xue. Uniformly-stable finite element methods for Darcy-Stokes-Brinkman models. *Journal of Computational Mathematics*, 26(3), 2008.

[98] Xuejun Xu and Shangyou Zhang. A new divergence-free interpolation operator with applications to the Darcy-Stokes-Brinkman equations. *SIAM Journal on Scientific Computing*, 32(2):855–874, 2010.

[99] Shangyou Zhang. A family of 3D continuously differentiable finite elements on tetrahedral grids. *Applied Numerical Mathematics*, 59(1):219–233, 2009.

[100] Shangyou Zhang. A family of $Q_{\mathrm{k+1,\ k}} \times Q_{\mathrm{k,\ k+1}}$ divergence-free finite elements on rectangular grids. *SIAM Journal on Numerical Analysis*, 47(3):2090–2107, 2009.

[101] Hui Zhou, Hamdi A Tchelepi, et al. Two-stage algebraic multiscale linear solver for highly heterogeneous reservoir models. *SPE Journal*, 17(02):523–539, 2012.